



## 저작자표시-비영리-변경금지 2.0 대한민국

이용자는 아래의 조건을 따르는 경우에 한하여 자유롭게

- 이 저작물을 복제, 배포, 전송, 전시, 공연 및 방송할 수 있습니다.

다음과 같은 조건을 따라야 합니다:



저작자표시. 귀하는 원저작자를 표시하여야 합니다.



비영리. 귀하는 이 저작물을 영리 목적으로 이용할 수 없습니다.



변경금지. 귀하는 이 저작물을 개작, 변형 또는 가공할 수 없습니다.

- 귀하는, 이 저작물의 재이용이나 배포의 경우, 이 저작물에 적용된 이용허락조건을 명확하게 나타내어야 합니다.
- 저작권자로부터 별도의 허가를 받으면 이러한 조건들은 적용되지 않습니다.

저작권법에 따른 이용자의 권리는 위의 내용에 의하여 영향을 받지 않습니다.

이것은 [이용허락규약\(Legal Code\)](#)을 이해하기 쉽게 요약한 것입니다.

[Disclaimer](#)

공학박사 학위논문

**Synthesis, Photophysical Properties and  
Electroluminescent Device Applications of  
Thermally Activated Delayed Fluorescence  
(TADF) Emitters**

열활성지연형광 (TADF) 현상을 활용한 발광체의 합  
성, 광물리학적 특성 평가 및 전기발광 소자에의 활  
용

2023 년 2월

서울대학교 대학원  
재료공학부

정 세 영

# Synthesis, Photophysical Properties and Electroluminescent Device Applications of Thermally Activated Delayed Fluorescence (TADF) Emitters

열활성지연형광 (TADF) 현상을 활용한 발광체의 합성, 광물리학적  
특성 평가 및 전기발광 소자에의 활용

지도교수 박 수 영

이 논문을 공학박사 학위논문으로 제출함

2023 년 2월

서울대학교 대학원  
재료공학부

정 세 영

정세영의 박사 학위논문을 인준함

2022년 12월

위 원 장 안 철 희 (인)

부 위 원 장 박 수 영 (인)

위 원 권 민 상 (인)

위 원 박 상 규 (인)

위 원 유 영 민 (인)

# Abstract

## **Synthesis, Photophysical Properties and Electroluminescent Device Applications of Thermally Activated Delayed Fluorescence (TADF) Emitters**

Seyoung Jung

Department of Materials Science and Engineering

The Graduate School

Seoul National University

Emitter plays most important role in organic light emitting diode (OLED) device so that the liveliest discussion has been made among the topics related OLED. Through generations of conventional fluorophore and phosphor, thermally activated delayed fluorescent (TADF) emitter get the spotlight because it broke through the limitation of light harvesting from different manner in multiplicity of excited state. To utilize TADF efficiently, excited triplet state of the emitter should be dealt with delicately to meet small energy difference with its excited singlet state. In this dissertation, important role of excited triplet state in TADF process from a photophysical point of view would be discussed in three series of materials.

In chapter 2, series of auxiliary functional groups with different electron

withdrawing or donating strength are introduced to PXZ-OXD, which is already reported material as a TADF emitter. From thorough study, unique trend of relationship between excited states stemming from intramolecular charge transfer (CT) and local excitation (LE) was found that could not be described with conventional photophysical model. With 2-level model, without assistance of LE state, fast reverse intersystem crossing (rISC) in target material could be described as the energy difference between singlet CT state and triplet CT state reduces. From the result, efficient bluegreen to green OLED devices could be fabricated.

In chapter 3, 1,8-naphthalimide is used as acceptor for red TADF emitter and two molecular design strategies are applied to make the red TADF emitter more efficient in color and brightness. While substitution of donor part in D-A type TADF emitter induced dramatic bathochromic shift in emission spectra, radiative decay of the emitter has faded into insignificance because of energy gap law in long-wavelength emitter. Instead, electron withdrawing auxiliary functional group made infinitesimal change in emission range but raised rISC rate constant, which led to increased external quantum efficiency (EQE) in OLED device.

In chapter 4, multiresonance (MR) type TADF emitters are proposed, with different detail of photophysical mechanism from traditional D-A type TADF emitters. Heavy atom effect from sulfur and silicon enhances rISC property which is crucial for TADF emitter.

**Keyword : Organic light emitting diode, thermally activated delayed**

**fluorescence, excited triplet state, fast reverse intersystem crossing, oxadiazole,  
naphthalimide, multiresonance**

**Student Number : 2016-20824**

# Contents

<b>Abstract .....</b>	<b>i</b>
<b>List of Tables .....</b>	<b>vii</b>
<b>List of Figures .....</b>	<b>ix</b>
<b>Chapter 1. Introduction .....</b>	<b>1</b>
1.1. Organic light emitting diodes (OLEDs).....	1
1.2. Thermally activated delayed fluorescence (TADF) .....	4
1.3. Photophysical process of TADF .....	7
1.4. Research objectives and outlines of thesis.....	9
1.5. References.....	11
<b>Chapter 2. 1,3,4-Oxadiazole Acceptor for Efficient Bluegreen- to-green TADF Emitter .....</b>	<b>15</b>
2.1. Research background .....	15
2.2. Experimental method.....	17
2.2.1. Materials and synthesis .....	17
2.2.2. Quantum chemical calculation .....	22
2.2.3. Photophysical and electrochemical characterization.....	22
2.2.4. Equations for rate constants .....	23
2.2.5. OLED device fabrication and device test.....	24
2.3. Results and discussions.....	26

2.3.1. Materials and design strategy .....	26
2.3.2. Theoretical calculation .....	26
2.3.3. Photophysical properties .....	30
2.3.4. Rate constant study.....	35
2.3.5. OLED device performance.....	37
2.4. Couclusions.....	42
2.5. References.....	43

### **Chapter 3. 1,8-Naphthalimide Acceptor for Efficient Red TADF Emitter ..... 47**

3.1. Research background.....	47
3.2. Experimental method.....	50
3.2.1. Materials and synthesis .....	50
3.2.2. Quantum chemical calculation .....	55
3.2.3. Photophysical and electrochemical characterization.....	55
3.2.4. Equations for rate constants .....	56
3.2.5. OLED device fabrication and device test.....	57
3.3. Results and discussions.....	59
3.3.1. Materials and design strategy .....	59
3.3.2. Theoretical calculation .....	59
3.3.3. Photophysical properties .....	62
3.3.4. Rate constant study.....	66
3.3.5. OLED device performance.....	68
3.4. Conclusions.....	72

3.5. References .....	73
<b>Chapter 4. Chalcogen-introduced Multiresonance TADF Emitter for Narrow and Pure Blue Emission .....</b>	<b>75</b>
4.1. Research background .....	75
4.2. Experimental method .....	77
4.2.1. Materials and synthesis .....	77
4.2.2. Quantum chemical calculation .....	90
4.2.3. Photophysical and electrochemical characterization.....	90
4.3. Results and discussions.....	92
4.3.1. Materials and design strategy .....	92
4.3.2. Theoretical calculation .....	93
4.3.3. Photophysical properties .....	96
4.4. Conclusions.....	103
4.5. References.....	104
<b>국문 초록 (Abstract in Korean) .....</b>	<b>106</b>
<b>List of Publications.....</b>	<b>108</b>
<b>List of Presentations.....</b>	<b>110</b>
<b>List of Patents .....</b>	<b>111</b>

## List of tables

<b>Table 2-1.</b> Selective parameters of 1,3,4-oxadiazole-based TADF emitters from DFT calculation .....	29
<b>Table 2-2.</b> Photophysical parameters of 1,3,4-oxadiazole-based TADF emitters from experiments .....	32
<b>Table 2-3.</b> Rate constants and other photophysical parameters of 1,3,4-oxadiazole-based TADF emitters.....	38
<b>Table 2-4.</b> Performance of OLED device using 1,3,4-oxadiazole-based TADF emitters.....	42
<b>Table 3-1.</b> Selective parameters of 1,8-naphthalimide-based TADF emitters from DFT calculation.....	61
<b>Table 3-2.</b> Photophysical parameters of 1,8-naphthalimide-based TADF emitters from experiments .....	67
<b>Table 3-3.</b> Performance of OLED device using 1,8-naphthalimide-based TADF emitters.....	71
<b>Table 4-1.</b> Selective parameters of MR type TADF emitters from DFT calculation .....	95

<b>Table 4-2.</b> Photophysical parameters of 1,3,4-oxadiazole-based TADF emitters from experiments .....	98
---	----

## List of Figures

<b>Figure 1-1.</b> Structure of OLED device .....	3
<b>Figure 2-1.</b> Chemical structure and synthesis scheme of target materials.....	18
<b>Figure 2-2.</b> Optimized structure and distribution of HOMOs and LUMOs of the target materials from DFT calculation .....	28
<b>Figure 2-3.</b> (upper) Absorption and emission spectra of target materials in toluene solution. (below) Emission spectra of target materials doped in mCPCN film ...	31
<b>Figure 2-4.</b> Low temperature PL spectra of the target materials doped in mCPCN film .....	34
<b>Figure 2-5.</b> Time-resolved radiative decay profile of target materials doped in mCPCN film in various temperatures .....	36
<b>Figure 2-6.</b> (a) Structure of OLED device. (b) J-V-L curve of the OLED device. (c) Electroluminescence spectrum of the OLED device. (d) External quantum efficiency graph of the OLED device .....	41
<b>Figure 3-1.</b> Chemical structure and synthetic route of the target materials.....	51
<b>Figure 3-2.</b> Optimized structure and distribution of HOMOs and LUMOs of the target materials from DFT calculation .....	60

<b>Figure 3-3.</b> (upper) Absorption and emission spectra of target materials in toluene solution. (below) Emission spectra of target materials doped in mCPCN film ...	63
<b>Figure 3-4.</b> Low temperature PL spectra of the target materials doped in mCPCN film. (left) PNIDMAC (right) diCF <sub>3</sub> PNIDMAC .....	65
<b>Figure 3-5.</b> Time-resolved radiative decay profile of target materials doped in mCPCN film in various temperatures. (left) PNIDMAC (right) diCF <sub>3</sub> PNIDMAC . .....	65
<b>Figure 3-6.</b> (a) Structure of OLED device. (b) J-V-L curve of the OLED device. (c) Electroluminescence spectrum of the OLED device. (d) External quantum efficiency graph of the OLED device .....	69
<b>Figure 4-1.</b> Chemical structure of the target materials .....	78
<b>Figure 4-2.</b> Optimized structure and distribution of HOMOs and LUMOs of OBO core and OBO-Si from DFT calculation .....	95
<b>Figure 4-3.</b> (upper) Absorption and (lower) emission spectra of target materials in toluene solution .....	97
<b>Figure 4-4.</b> Emission spectra of target materials doped in DPEPO film .....	98
<b>Figure 4-5.</b> Low temperature PL spectra of the target materials in toluene solution .....	101

<b>Figure 4-6.</b> Time-resolved radiative decay profile of target materials doped in DPEPO film .....	102
--	-----

# **Chapter 1.**

## **Introduction**

### **1.1. Organic light emitting diodes (OLEDs)**

A display is an information medium that compresses and visualizes information. Since the spread of cathode ray tube (CRT) monitors appeared in the 1950s, display has been evolved in the direction of full-color implementation, resolution increase, enlargement in panel area, and thickness reduction through continuous development. As of the 2020s, OLED panels are widely used as a result of their development and are in an industrially important position. OLED is an optoelectronic device that receives electrons and holes from electrodes and utilizes light generated through the energy of excitons generated by the combination of charge carriers the light emitting layer containing emitter material.<sup>1</sup>

The earliest form of OLED device, announced by C. Tang, has a simple structure in which only a light emitting layer exists.<sup>2</sup> The device was driven by directly injecting, moving, and combining of electrons and holes toward light emitting from the emitter. Through these findings, it was confirmed that OLED may be possible option for industrial display field. Subsequently, an improved device structure model was presented through further research, and accordingly, performance was improved rapidly.<sup>3,4</sup> First, some studies have shown that the area where electron and hole are combined is limited to a specific range, not across all over the device. Based on this, charge carrier transporting layers were introduced in

addition to the light emitting layer to improve the electrical driving characteristics of the device, although it does not directly participate in the light emitting of the device. Additionally, a charge carrier injection layer was designed to alleviate the barrier of charge carrier movement due to the energy level difference between each electrode and the charge carrier transfer layer, and a blocking layer to prevent the charge carrier transfer layer from receiving energy generated by the hole and charge. In conclusion, the general structure of OLED devices currently manufactured consists of a combination of a transparent substrate, a thin organic layer stacked from an anode, and a metal cathode, as shown in **Figure 1.1**. At this time, it is observed that light generated from the light emitting layer comes out in the direction of the transparent substrate.

Each element has developed in its own direction to make highly efficient OLED devices, including mobility of charge carrier transporting material,<sup>5-9</sup> alignment of molecular orbital energy or excited state energy,<sup>10-12</sup> prohibition of concentration quenching mechanisms of emission by applying host-dopant system in emitting layer.<sup>13-15</sup> Among them, the most actively studied field is the emitter material itself. In OLED devices, emitters can directly receive charge carriers to generate light, or hosts that form most of a light-emitting layer can receive energy generated through the combination of charge carriers to generate light. In order to induce such luminescence to emit light of the desired color with high efficiency, studies are actively being conducted to identify the mechanism of luminescence or to change the chemical structure of the emitter.

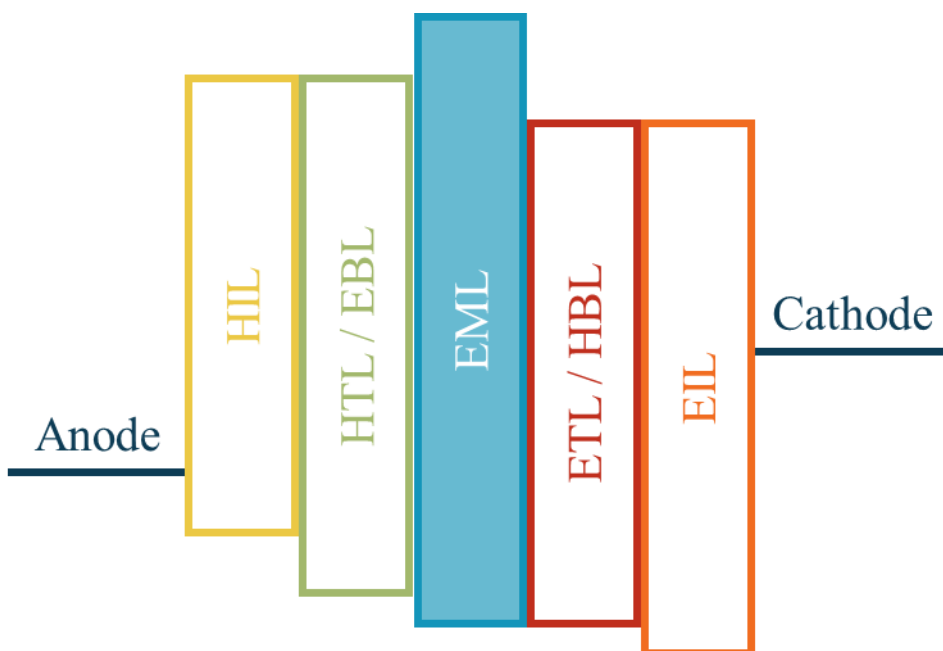


**Figure 1-1.** Structure of OLED device.

## 1.2. Thermally Activated Delayed Fluorescence (TADF)

When the light emitter in the ground state receives energy and is excited, it emits energy in the form of light through a series of photophysical processes and returns to the ground state. Emitters that have received the energy of photons or the binding energy of excitons without the provision of new charge carriers have an excited state of which multiplicity called a singlet or triplet depending on the spin configuration of the electrons constituting the molecule. When a radiative relaxation is caused by a singlet state, it is called fluorescence, while it is caused by a triplet state, it is called phosphorescence. Most light emitters have a structure in which light emission in one mode of phosphorescence and fluorescence is dominant.

In the driving situation of OLED devices, electrons and holes with the same spin arrangement as electrons are combined to create an exciton. Thus, statistically, a singlet excited state accounts for 25% of the totally generated exciton, and a triplet excited state accounts for 75%.<sup>16-19</sup> In the light emitting layer of the host-dopant system, since the subject to which the charge carrier is transported is the host material, the emitter, which is the dopant, receives energy from the host. Namely, the fluorophore receives an excited singlet state of the host mainly through Förster resonance energy transfer, and the phosphor receives an excited triplet state of the host through Dexter energy transfer. In this process, multiplicity of excited states that are not necessarily used for light emission are discarded unless a separate multiplicity substitution process is applied, resulting in technical limitations in the exciton utilization efficiency.

In order to overcome these limitations, multiplicity substitution processes such as triplet-triplet annihilation (TTA) and hybridized local and charge transfer (HLCT) have been proposed. However, TTA still has the disadvantage of not being able to fully utilize excitons in that more than two excited triplet states are substituted with a single excited singlet state energetically, and the high-energy excited state of HLCT risks disintegrating the bonds of the elements, especially the molecules that make up the emission layer. Thus, the demand for a photophysical mechanism to replace an excited singlet state and an excited triplet with low energy and by one-on-one has emerged.

To realize the ideal photophysical process, people focused on the energy difference of the excited singlet and triplet states of the molecule ( $\Delta E_{ST}$ ). A typical organic molecule has a  $\Delta E_{ST}$  of approximately 0.5 to 1 eV scale, but in some organic molecules this value decreases to 0.2 eV or close to zero. In these organic molecules, thermally activated delayed fluorescence (TADF), which has the same emission spectrum as fluorescence and lasts much longer than fluorescence, was observed. TADF looks similar to phosphorescence in that it utilizes emission with lifetime of microsecond scale, not an emission lifetime of ns from general fluorescence from excited singlet state, but unlike phosphorescence with a separate emission spectrum from fluorescence, the existing emission spectrum of the fluorescence is maintained. In addition, the excited triplet state and the singlet state are exchanged one-to-one, and the energy is not high, so the limitations of the previously described multiplicity substitution process could be overcome. C. Adachi reported that OLED devices

using emitter with TADF characteristics overcame the limitations of light emission efficiency of existing fluorescent OLEDs.<sup>20</sup> Since then, numerous researchers around the world have competitively reported OLED devices with excellent light emission efficiency using various types of TADF emitters.<sup>21-26</sup>

The most important thing to consider to impart TADF properties to the phosphor is  $\Delta E_{ST}$ . It is known that  $\Delta E_{ST}$  is theoretically calculated following the equation below,

$$\Delta E_{ST} = 2 \cdot \iint \phi_{LUMO}(\mathbf{1})\phi_{HOMO}(\mathbf{2})\left(\frac{e^2}{r_1 - r_2}\right)\phi_{LUMO}(\mathbf{2})\phi_{HOMO}(\mathbf{1}) d\mathbf{r}_1 d\mathbf{r}_2$$

which is directly proportional to  $\langle\phi_{HOMO}|\phi_{LUMO}\rangle$ , the orbital overlap integral. Therefore, in order to minimize  $\Delta E_{ST}$ , HOMO and LUMO must be separated into separate spaces within the molecule. On the other hand, fluorescence itself includes molecular orbital change from LUMO to HOMO, which means its transition possibility is also proportional to the orbital overlap integral. Therefore, TADF emitters should be designed so that spatial separation of HOMO-LUMO occurs to an appropriate degree between the two counterparts.

### 1.3. Detailed photophysical mechanism of TADF

Among the contents mentioned in the previous section, the D-A type of TADF phosphor has a lowest excited single and triplet state based on an intramolecular charge transfer (ICT) from the donor part to the acceptor part. According to El Sayed rules, intersystem crossing (ISC) is difficult to occur between excited states with similar types of molecular orbitals, so in order for a material to show an active TADF phenomenon, an excited state with a different type of molecular orbital must be assisted.<sup>27</sup> In conclusion, a 3-level model describing the correlation of these three states of  $^1\text{CT}$ ,  $^3\text{CT}$ , and  $^3\text{LE}$  is commonly applied to the molecular structure design of D-A type TADF phosphors. In detail, an emitter exhibiting TADF properties requires (1) the lowest excited triplet state based on LE and at the same time small  $\Delta E_{\text{ST}}$ , or (2) the lowest excited triplet state based on ICT and reverse ISC (rISC) route being preceded by internal conversion between  $^3\text{CT}$  and  $^3\text{LE}$ . These constraints are generally applied without difficulty to blue TADF phosphors with  $^1\text{CT}$  levels of energy similar to donor and acceptor parts with LE excited states located in the ultraviolet region. However, emitters showing excellent TADF characteristics are reported even when the lowest excited triplet state is ICT-based and the large energy difference between  $^3\text{CT}$  so that internal conversion toward  $^3\text{LE}$  is difficult to occur where conventional 3-level models do not provide sufficient evidence. A recent study has reported that even without the help of the locally excited state, rISC between the ICT-based excited singlet and triplet state occurs. For this phenomenon, the D-A type TADF phosphor is placed in an environment

with appropriate polarity and the energies of  $^1\text{CT}$  and  $^3\text{CT}$  are located close enough, supported by the vibronic perturbation of the molecule.<sup>28-29</sup> Some molecular systems to prove these findings have been reported, and the limitations of the existing 3-level model have been overcome through a 2-level model describing the correlation between the two states of  $^1\text{CT}$  and  $^3\text{CT}$  through experimental evidence.

## 1.4. Objectives and outlines of thesis

From the previous sections, TADF emitters could get attraction from academic and industrial area for the ultimate model of emitter for OLED. In fact, researchers at the organic emitter field have been reporting new combinations of donor – acceptor or heteroatoms for multiresonance. In addition to this, TADF emitter have been used not only as an emitter in the light emitting layer, but also as an assistant dopant for conventional fluophore, which is called hyperfluorescence. Versatility of TADF emitter justified its importance in the informatic display field.

Although usage of the excited triplet state is crucial in overall TADF process, its scrutinization has a limitation with simple photophysical measurement and needs special treatment including time-dependent study and cryogenic measurement, which led to lack of description of photophysics of excited triplet state. In this study, more detailed study on the essence of excited triplet state of TADF emitter would be described with series of materials.

In **Chapter 2**, 1,3,4-oxadiazole acceptor and 10*H*-phenoxazine donor are used to make a green-light emitting D-A type TADF material and various auxiliary chemical group are introduced to study tendency of TADF process within delicately tuned series of materials. Electron-donating dimethylamino group and methoxy group, and electron-withdrawing fluoro group, trifluoromethyl group and nitrile group are presented to manage  $\Delta E_{ST}$  and intensify rISC process in the material. From quantum chemical calculation and rate constant study, possible rISC process that fits 2-level model are stated.

In **Chapter 3**, 1,8-naphthalimide acceptor is used as acceptor for red-light emitting D-A type TADF material. Faster delayed fluorescence could be observed as electron-withdrawing trifluoromethyl group applied adjacent to the acceptor core with a small bathochromic shift of emission.

In **Chapter 4**, chalcogen and boron heteroatoms are used to derive multiresonance type TADF and heavy atom effect of sulfur with newly introduced tetraphenylsilyl group into the emitter material is suggested. To support model of photophysical process in ultraviolet-to-blue-light emitting MR type TADF material, quantum chemical calculation, low temperature photoluminescence and time-dependent radiation decay profile are measured and analyzed.

## 1.5. References

1. Stolka, M.; Yanus, J. F.; Pai, D. M. Hole transport in solid solutions of a diamine in polycarbonate. *The Journal of Physical Chemistry* **1984**, *88* (20), 4707-4714.
2. Tang, C. W.; VanSlyke, S. A., Organic electroluminescent diodes. *Applied Physics Letters* **1987**, *51* (12), 913-915.
3. Gather, M. C.; Köhnen, A.; Meerholz, K. White Organic Light-Emitting Diodes. *Advanced Materials* **2011**, *23* (2), 233-248.
4. Brown, A. R.; Bradley, D. D. C.; Burroughes, J. H.; Friend, R. H.; Greenham, N. C.; Burn, P. L.; Holmes, A. B.; Kraft, A. Poly(p-phenylenevinylene) light-emitting diodes: Enhanced electroluminescent efficiency through charge carrier confinement. *Applied Physics Letters* **1992**, *61* (23), 2793-2795.
5. Tamoto, N.; Adachi, C.; Nagai, K. Electroluminescence of 1,3,4-Oxadiazole and Triphenylamine-Containing Molecules as an Emitter in Organic Multilayer Light Emitting Diodes. *Chemistry of Materials* **1997**, *9* (5), 1077-1085.
6. Yang, Y.; Heeger, A. J. Polyaniline as a transparent electrode for polymer light-emitting diodes: Lower operating voltage and higher efficiency. *Applied Physics Letters* **1994**, *64* (10), 1245-1247.
7. Dodabalapur, A. Organic light emitting diodes. *Solid State Communications* **1997**, *102* (2), 259-267.
8. Matsushima, T.; Takamori, M.; Miyashita, Y.; Honma, Y.; Tanaka, T.; Aihara, H.; Murata, H. High electron mobility layers of triazines for improving driving voltages, power conversion efficiencies, and operational stability of organic light-emitting diodes. *Org. Electron.* **2010**, *11* (1), 16-22.
9. Rhee, S. H.; Nam, K. b.; Kim, C. S.; Song, M.; Cho, W.; Jin, S. -H.; Ryu, S. Y. Effect of

- Electron Mobility of the Electron Transport Layer on Fluorescent Organic Light-Emitting Diodes. *ECS Solid State Letters* **2014**, 3 (5), R19.
10. Hu, Z.; Zhong, Z.; Chen, Y.; Sun, C.; Huang, F.; Peng, J.; Wang, J.; Cao, Y. Energy-Level Alignment at the Organic/Electrode Interface in Organic Optoelectronic Devices. *Advanced Functional Materials* **2016**, 26 (1), 129-136.
  11. Sanderson, S.; Philippa, B.; Vamvounis, G.; Burn, P. L.; White, R. D. Elucidating the effects of guest-host energy level alignment on charge transport in phosphorescent OLEDs. *Applied Physics Letters* **2019**, 115 (26), 263301.
  12. Yadav, R. A. K.; Dubey, D. K.; Chen, S.-Z.; Liang, T.-W.; Jou, J.-H. Role of Molecular Orbital Energy Levels in OLED Performance. *Scientific Reports* **2020**, 10 (1), 9915.
  13. Xie, H. Z.; Liu, M. W.; Wang, O. Y.; Zhang, X. H.; Lee, C. S.; Hung, L. S.; Lee, S. T.; Teng, P. F.; Kwong, H. L.; Zheng, H.; et al. Reduction of Self-Quenching Effect in Organic Electrophosphorescence Emitting Devices via the Use of Sterically Hindered Spacers in Phosphorescence Molecules. *Advanced Materials* **2001**, 13 (16), 1245-1248.
  14. Jeon, W. S.; Park, T. J.; Kim, S. Y.; Pode, R.; Jang, J.; Kwon, J. H. Ideal host and guest system in phosphorescent OLEDs. *Org. Electron.* **2009**, 10 (2), 240-246.
  15. Zhou, Y.; Kim, J. W.; Nandhakumar, R.; Kim, M. J.; Cho, E.; Kim, Y. S.; Jang, Y. H.; Lee, C.; Han, S.; Kim, K. M.; et al. Novel binaphthyl-containing bi-nuclear boron complex with low concentration quenching effect for efficient organic light-emitting diodes. *Chemical Communications* **2010**, 46 (35), 6512-6514.
  16. Tao, S. L.; Hong, Z. R.; Peng, Z. K.; Ju, W. G.; Zhang, X. H.; Wang, P. F.; Wu, S. K.; Lee, S. T. Anthracene derivative for a non-doped blue-emitting organic electroluminescence device with both excellent color purity and high efficiency. *Chem. Phys. Lett.* **2004**, 397 (1-3), 1-4.
  17. Baldo, M. A.; O'Brien, D. F.; You, Y.; Shoustikov, A.; Sibley, S.; Thompson, M. E.;

- Forrest, S. R., Highly efficient phosphorescent emission from organic electroluminescent devices. *Nature* **1998**, *395* (6698), 151-154.
18. Baldo, M. A.; Lamansky, S.; Burrows, P. E.; Thompson, M. E.; Forrest, S. R., Very high-efficiency green organic light-emitting devices based on electrophosphorescence. *Applied Physics Letters* **1999**, *75* (1), 4-6.
19. Bin, J.-K.; Cho, N.-S.; Hong, J.-I., New Host Material for High-Performance Blue Phosphorescent Organic Electroluminescent Devices. *Advanced Materials* **2012**, *24* (21), 2911-2915.
20. Endo, A.; Sato, K.; Yoshimura, K.; Kai, T.; Kawada, A.; Miyazaki, H.; Adachi, C., Efficient up-conversion of triplet excitons into a singlet state and its application for organic light emitting diodes. *Applied Physics Letters* **2011**, *98* (8), 083302.
21. Lee, S. Y.; Yasuda, T.; Yang, Y. S.; Zhang, Q.; Adachi, C. Luminous Butterflies: Efficient Exciton Harvesting by Benzophenone Derivatives for Full-Color Delayed Fluorescence OLEDs. *Angewandte Chemie International Edition* **2014**, *53* (25), 6402-6406.
22. Kaji, H.; Suzuki, H.; Fukushima, T.; Shizu, K.; Suzuki, K.; Kubo, S.; Komino, T.; Oiwa, H.; Suzuki, F.; Wakamiya, A.; Murata, Y.; Adachi, C., Purely organic electroluminescent material realizing 100% conversion from electricity to light. *Nature Communications* **2015**, *6* (1), 8476.
23. Chen, D. Y.; Liu, W.; Zheng, C. J.; Wang, K.; Li, F.; Tao, S. L.; Ou, X. M.; Zhang, X. H. Isomeric Thermally Activated Delayed Fluorescence Emitters for Color Purity-Improved Emission in Organic Light-Emitting Devices. *ACS Appl. Mater. Interfaces* **2016**, *8* (26), 16791-16798.
24. Godumala, M.; Choi, S.; Cho, M. J.; Choi, D. H. Thermally activated delayed fluorescence blue dopants and hosts: from the design strategy to organic light-emitting diode applications. *Journal of Materials Chemistry C* **2016**, *4* (48), 11355-11381.

25. Nobuyasu, R. S.; Ren, Z.; Griffiths, G. C.; Batsanov, A. S.; Data, P.; Yan, S.; Monkman, A. P.; Bryce, M. R.; Dias, F. B. Rational Design of TADF Polymers Using a Donor–Acceptor Monomer with Enhanced TADF Efficiency Induced by the Energy Alignment of Charge Transfer and Local Triplet Excited States. *Advanced Optical Materials* **2016**, *4* (4), 597-607.
26. Yuan, Y.; Hu, Y.; Zhang, Y. X.; Lin, J. D.; Wang, Y. K.; Jiang, Z. Q.; Liao, L. S.; Lee, S. T. Over 10% EQE Near-Infrared Electroluminescence Based on a Thermally Activated Delayed Fluorescence Emitter. *Advanced Functional Materials* **2017**, *27* (26).
27. Braslavsky, S. E. Glossary of Terms used in Photochemistry, 3<sup>rd</sup> Edition (IUPAC Recommendations 2006). *Pure and Applied Chemistry* **2007**, *79* (3), 293-465.
28. Ryoo, C. H.; Han, J.; Yang, J.-h.; Yang, K.; Cho, I.; Jung, S.; Kim, S.; Jeong, H.; Lee, C.; Kwon, J. E.; et al. Systematic Substituent Control in Blue Thermally Activated Delayed Fluorescence (TADF) Emitters: Unraveling the Role of Direct Intersystem Crossing between the Same Charge-Transfer States. *Advanced Optical Materials* **2022**, *10* (24), 2201622.
29. Serdiuk, I. E.; Jung, S.; Mońka, M.; Ryoo, C. H.; Park, S. Y. Contradictory Role of Locally-Excited Triplet States in Blue Thermally Activated Delayed Fluorescence of s-Triazine-Based Emitters. *The Journal of Physical Chemistry C* **2023**, *127* (1), 358-367.

## Chapter 2.

# 1,3,4-Oxadiazole Acceptor for Efficient Bluegreen-to-Green TADF Emitter

### 2.1. Research background

Emissive performance of organic light emitting diode (OLED) device has been receiving the most attention among OLED-related studies. In the earlier days, it was proved that the luminescence of organic materials can be utilized in electronic devices,<sup>1</sup> and the limit of efficiency of conventional fluorescent OLED devices was overcome in phosphorescent OLED.<sup>2-4</sup> However, due to the emissive mechanism of traditional fluorophors and phosphors, only a part of singlet or triplet excitons generated in OLED devices could be used, which was a harsh limit to achieving high efficiency. In order to solve the issue, groundbreaking fluorophor utilizing thermally activated delayed fluorescence (TADF) was proposed.<sup>5</sup> In TADF emitters, the lowest excited triplet state ( $T_1$ ) can be converted to the lowest excited singlet state ( $S_1$ ) through reverse inter-system crossing (rISC), so that all excitons can be utilized for luminescence despite being a fluorophor. Based on this point, a variety of high-efficiency OLED devices using TADF have been reported so far.<sup>6-9</sup>

To activate rISC, TADF emitter uses a molecular design in which an electron donating moiety (donor, D) and electron withdrawing moiety (acceptor, A) pair is

directly connected. The D-A linkage allows the separation of the HOMO and LUMO regions in the molecule, thereby reducing the energy difference between  $S_1$  and  $T_1$  ( $\Delta E_{ST}$ ).<sup>10,11</sup> In order to control the characteristics of the emitter, donor and acceptor can be changed basically,<sup>12</sup> or the  $\pi$ -conjugation of the entire molecule can be controlled by introducing a phenyl ring between the donor and acceptor.<sup>13</sup> There would be also a design strategy to improve the properties of emitters by introducing functional groups that can control electronic properties, bulkiness, or rigidity.<sup>14-15</sup>

In this chapter, various types of functional groups were added to the combination of 1,3,4-oxadiazole donor and 10*H*-phenoxazine acceptor based on 2PXZ-OXD and PXZ-OXD, which are excellent D-A type TADF phosphors that have already been reported in paper.<sup>16</sup> However, detailed photophysical mechanism could not be totally described with conventional 3-level model as the energy level of the excited states of PXZ-OXD were far from energy from 1,3,4-oxadiazole and 10*H*-phenoxazine. By introducing functional groups, performance of the emitter could be delicately modified without change its D-A combination. Various derivatives could be obtained from the molecular design strategy while maintaining the existing synthesis scheme if appropriate precursors exist. Based on the above-mentioned advantages, it was possible to finely tune emission performance of PXZ-OXD while maintaining TADF characteristics. In addition, by applying 2-level model, consistent description of the TADF characteristics within the series of target materials could be performed.

## 2.2. Experimental method

### 2.2.1. Materials and synthesis

All target materials were synthesized in a three-step reaction from benzohydrazide derivatives as reported in the references.<sup>16</sup> Chemicals for synthesis of the target materials were used as purchased from commercial suppliers, without further purification. Thin layer chromatography (TLC) plate (silica gel 60 F254, Merck Co.) and silica gel 60 (particle size 0.063 – 0.200mm, Merck co.) were used to judge the reaction progress and for column chromatographic purification.

Chemical structures of the final target materials were assigned by analyzing nuclear magnetic resonance (NMR) spectra, mass spectra and elemental analysis (EA) data. <sup>1</sup>H-NMR data of the target materials were recorded on Avance-300 (Bruker), and <sup>13</sup>C-NMR data were recorded on Avance-500 (Bruker). Mass spectra of the target materials were obtained with JMS-T100LP 4G (JEOL). EA of carbon, hydrogen and nitrogen of the target materials was executed with Flash2000 (ThermoFisher Scientific).

#### *Synthesis of PXZ-OXD*

To a dehydrated round-bottomed flask connected with a reflux condenser, a mixture of 2-(4-bromophenyl)-5-phenyl-1,3,4-oxadiazole (1.73 g, 5.74 mmol), 10*H*-phenoxazine (1.16 g, 6.32 mmol), bis(tri-*tert*-butylphosphine) palladium(0) as Pd catalyst (30 mg, 0.06 mmol), potassium *tert*-butoxide (1.16 g, 10.34 mmol) and

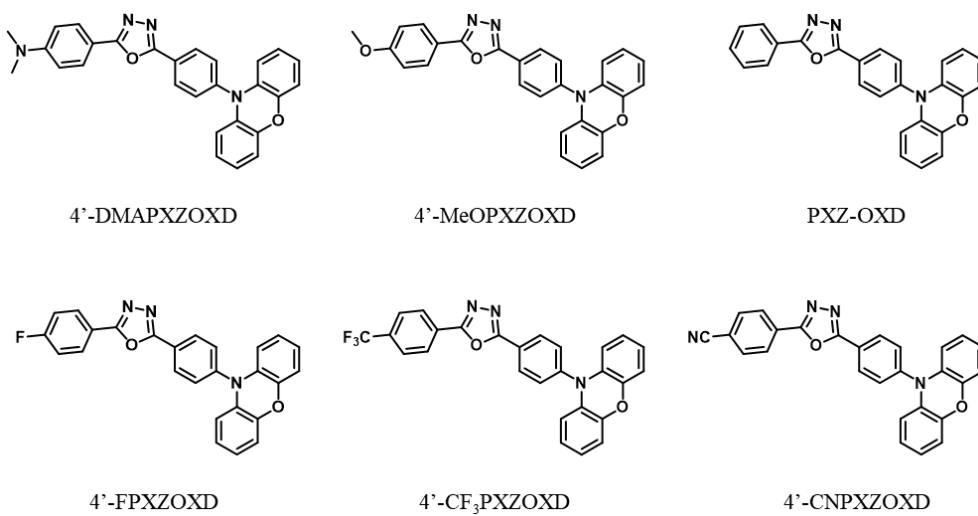


**Figure 2-1.** Chemical structure of the target materials.

anhydrous toluene (20 mL) was refluxed under inert atmosphere filled with Ar for 24 hours. After the reaction finished, the mixture was cooled down to room temperature and the solvent was removed under reduced pressure, followed by extraction with brine and dichloromethane. The organic layer was dried with  $\text{MgSO}_4$  and concentrated under reduced pressure. The residual solid crude material was purified by column chromatography on silica gel using mixture solvent of ethyl acetate / n-hexane (v:v 1:5) and recrystallized from mixed solvent of chloroform and methanol to afford 10-(4-(5-phenyl-1,3,4-oxadiazol-2-yl)phenyl)-10*H*-phenoxazine (**PXZ-OXD**) as yellow powder (1.56 g, yield: 67.3 %).  $^1\text{H}$  NMR (300MHz,  $\text{CDCl}_3$ )  $\delta$ : 8.38 (d,  $J = 8.7$  Hz, 2H), 8.20-8.14 (m, 2H), 7.61-7.52 (m, 5H), 6.76-6.66 (m, 4H), 6.62 (td,  $J_1 = 7.4$  Hz,  $J_2 = 2.2$  Hz, 2H), 5.99 (dd,  $J_1 = 7.8$  Hz,  $J_2 = 1.5$  Hz, 2H).  $^{13}\text{C}$  NMR (125MHz,  $\text{CDCl}_3$ )  $\delta$ : 165.13, 164.10, 144.18, 142.56, 133.96, 132.17, 132.00, 129.90, 129.39, 127.23, 124.16, 123.97, 123.54, 122.07, 115.94, 113.47. coldspray-LC-TOF-MS  $m/z$ : calculated for  $\text{C}_{26}\text{H}_{17}\text{N}_3\text{O}_2$ ; 403.13, found;  $[\text{M}+\text{H}]^+$  404.1880. EA: calculated for  $\text{C}_{26}\text{H}_{17}\text{N}_3\text{O}_2$ ; C 77.41, H 4.25, N 10.42, found; C 75.51, H 4.32, N 9.80.

#### *Synthesis of 4'-DMAPXZOXD*

2-(4-bromophenyl)-5-(4-dimethylaminophenyl)-1,3,4-oxadiazole was used instead of 2-(4-bromophenyl)-5-phenyl-1,3,4-oxadiazole. Pale yellow powder.  $^1\text{H}$  NMR (300MHz,  $\text{CDCl}_3$ )  $\delta$ : 8.35 (d,  $J = 8.7$  Hz, 2H), 8.00 (d,  $J = 9.3$  Hz, 2H), 7.52 (d,  $J = 8.4$  Hz, 2H), 6.78 (d,  $J = 9.0$  Hz, 2H), 6.75-6.58 (m, 6H), 5.99 (dd,  $J_1 = 7.8$  Hz,  $J_2 = 1.5$  Hz, 2H), 3.09 (s, 6H).  $^{13}\text{C}$  NMR (125MHz,  $\text{CDCl}_3$ )  $\delta$ : 165.84, 163.01,

152.69, 144.16, 141.95, 134.05, 131.85, 129.62, 128.63, 124.68, 123.53, 121.96, 115.87, 113.47, 111.83, 110.86, 40.32. coldspray-LC-TOF-MS  $m/z$ : calculated for  $C_{28}H_{22}N_4O_2$ ; 446.17, found;  $[M+H]^+$  447.2292. EA: calculated for  $C_{28}H_{22}N_4O_2$ ; C 75.32, H 4.97, N 12.55, found; C 73.80, H 4.84, N 12.24.

#### *Synthesis of 4'-MeOPXZOXD*

2-(4-bromophenyl)-5-(4-methoxyphenyl)-1,3,4-oxadiazole was used instead of 2-(4-bromophenyl)-5-phenyl-1,3,4-oxadiazole. Pale yellow powder.  $^1H$  NMR (300MHz,  $CDCl_3$ )  $\delta$ : 8.36 (d,  $J = 8.4$  Hz, 2H), 8.11 (d,  $J = 9.0$  Hz, 2H), 7.54 (d,  $J = 8.7$  Hz, 2H), 7.06 (d,  $J = 9.0$  Hz, 2H), 6.77-6.58 (m, 6H), 5.99 (dd,  $J_1 = 7.8$  Hz,  $J_2 = 1.5$  Hz, 2H), 3.91 (s, 3H).  $^{13}C$  NMR (125MHz,  $CDCl_3$ )  $\delta$ : 165.08, 163.64, 162.73, 144.17, 142.33, 133.99, 131.94, 129.77, 129.01, 124.33, 123.53, 122.04, 116.44, 115.92, 114.82, 113.47, 55.73. coldspray-LC-TOF-MS  $m/z$ : calculated for  $C_{27}H_{19}N_3O_3$ ; 433.14, found;  $[M+H]^+$  434.1998. EA: calculated for  $C_{27}H_{19}N_3O_3$ ; C 74.81, H 4.42, N 9.69, found; C 75.44, H 4.32, N 9.71.

#### *Synthesis of 4'-FPXZOXD*

2-(4-bromophenyl)-5-(4-fluorophenyl)-1,3,4-oxadiazole was used instead of 2-(4-bromophenyl)-5-phenyl-1,3,4-oxadiazole. Yellow powder.  $^1H$  NMR (300MHz,  $CDCl_3$ )  $\delta$ : 8.37 (d,  $J = 8.7$  Hz, 2H), 8.18 (dd,  $J_1 = 9.0$  Hz,  $J_2 = 5.1$  Hz, 2H), 7.56 (d,  $J = 8.7$  Hz, 2H), 7.26 (d,  $J = 17.4$  Hz, 2H), 6.76-6.66 (m, 4H), 6.62 (td,  $J_1 = 7.3$  Hz,  $J_2 = 2.0$  Hz, 2H), 5.99 (dd,  $J_1 = 8.0$  Hz,  $J_2 = 1.4$  Hz, 2H).  $^{13}C$  NMR (125MHz,  $CDCl_3$ )

$\delta$ : 166.16, 164.32, 164.13, 164.12, 144.18, 142.65, 133.93, 132.02, 129.88, 129.55, 129.49, 124.01, 123.53, 122.10, 120.31, 120.28, 116.87, 116.69, 115.96, 113.47. coldspray-LC-TOF-MS  $m/z$ : calculated for  $C_{26}H_{16}FN_3O_2$ ; 421.12, found;  $[M+H]^+$  422.1833. EA: calculated for  $C_{26}H_{16}FN_3O_2$ ; C 74.10, H 3.83, N 9.97, found; C 74.93, H 3.85, N 9.96.

#### *Synthesis of 4'-CF<sub>3</sub>PXZOXD*

2-(4-bromophenyl)-5-(4-(trifluoromethyl)phenyl)-1,3,4-oxadiazole was used instead of 2-(4-bromophenyl)-5-phenyl-1,3,4-oxadiazole. Yellow powder.  $^1H$  NMR (300MHz,  $CDCl_3$ )  $\delta$ : 8.39 (d,  $J$  = 8.4 Hz, 2H), 8.31 (d,  $J$  = 8.1 Hz, 2H), 7.84 (d,  $J$  = 8.1 Hz, 2H), 7.58 (d,  $J$  = 8.4 Hz, 2H), 6.77-6.60 (m, 6H), 5.99 (dd,  $J_1$  = 7.8 Hz,  $J_2$  = 1.5 Hz, 2H).  $^{13}C$  NMR (125MHz,  $CDCl_3$ )  $\delta$ : 164.64, 163.95, 144.21, 142.97, 133.89, 132.09, 130.03, 127.53, 127.18, 126.47, 126.44, 123.72, 123.53, 122.16, 116.00, 113.47. coldspray-LC-TOF-MS  $m/z$ : calc.d for  $C_{27}H_{16}F_3N_3O_2$  471.12, found  $[M+H]^+$  472.1873. EA: calc.d for  $C_{27}H_{16}F_3N_3O_2$ ; C 68.79, H 3.42, N 8.91, found; C 68.80, H 3.40, N 8.86.

#### *Synthesis of 4'-CNPXZOXD*

4-(5-(4-bromophenyl)-1,3,4-oxadiazol-2-yl)benzonitrile was used instead of 2-(4-bromophenyl)-5-phenyl-1,3,4-oxadiazole. Red powder.  $^1H$  NMR (300MHz,  $CDCl_3$ )  $\delta$ : 8.39 (d,  $J$  = 8.7 Hz, 2H), 8.30 (d,  $J$  = 8.7 Hz, 2H), 7.87 (d,  $J$  = 8.7 Hz, 2H), 7.58 (d,  $J$  = 8.7 Hz, 2H), 6.76-6.67 (m, 4H), 6.62 (td,  $J_1$  = 7.4 Hz,  $J_2$  = 2.1 Hz, 2H),

5.99 (dd,  $J_1 = 7.8$  Hz,  $J_2 = 1.2$  Hz, 2H).  $^{13}\text{C}$  NMR (125MHz,  $\text{CDCl}_3$ )  $\delta$ : 164.86, 163.57, 144.21, 143.15, 133.84, 133.19, 132.12, 130.06, 127.80, 127.63, 123.52, 122.21, 118.05, 116.03, 115.62, 113.48. coldspray-LC-TOF-MS  $m/z$ : calc.d for  $\text{C}_{27}\text{H}_{16}\text{N}_4\text{O}_2$  428.13, found  $[\text{M}+\text{H}]^+$  429.1918. EA: calc.d for  $\text{C}_{27}\text{H}_{16}\text{N}_4\text{O}_2$ ; C 75.69, H 3.76, N 13.08, found; C 75.99, H 3.73, N 13.09.

### 2.2.2. Quantum chemical calculation

All quantum chemical calculations were carried out using the Gaussian 09 quantum chemical package. Geometry optimization in the ground state was performed using density functional theory (DFT) method with B3LYP functional / 6-31G(d,p) basis set. Energy levels of the ground state and some excited state with singlet or triplet multiplicity were calculated using time-dependent DFT (TD-DFT) method with B3LYP functional / 6-31G(d,p) basis set.

### 2.2.3. Photophysical and electrochemical characterization

Solution samples for cyclic voltammetry (CV) measurement were prepared as concentration of  $5 \times 10^{-3}$  M in methylene chloride, with 0.1 M TBAHFP as the supporting electrolyte. Solution samples for other photophysical characterizations were prepared as concentrations of  $10^{-5}$  M in toluene. Film samples were fabricated on quartz substrate using thermal evaporation under vacuum ( $P < 10^{-4}$  Pa), with co-deposition rate of  $1.0 \text{ \AA s}^{-1}$  in total for the emitter and host material. Quartz substrates were rinsed by sonication with detergent-containing deionized water, acetone, and

isopropyl alcohol, in the listed order.

CV was performed on 273A (Princeton Applied Research) using a three-electrode solution container cell. Three electrodes include an Ag wire in 0.01 M AgNO<sub>3</sub> solution as a reference electrode, a carbon disc as a working electrode, and a Pt wire as a counter electrode. The redox potential of the reference electrode was calibrated using ferrocene/ferrocenium (Fc/Fc<sup>+</sup>) as an internal standard. For steady-state photophysical studies, UV-1650PC (Shimadzu) for UV-Vis absorption spectra, QuantaMaster 40 (Photon Technology International) for room temperature photoluminescence spectra, Cary Eclipse fluorescence spectrophotometer (Varian) for low temperature photoluminescence spectra were used, respectively. In order to remove background data, quartz cuvette filled with toluene, which was the solvent for the solution samples, or blank quartz substrate was used for the steady-state photophysical studies. Time-dependent photoluminescence decay profiles were observed by FluoTime 200 (PicoQuant) and analyzed by time-correlated single photon counting technique.

#### **2.2.4. Equations for rate constants**

According to the reference<sup>10</sup>, equations below were used to calculate rate constants related to TADF process. Symbols used for terminologies were described as follows:  $\Phi_{\text{PF}}$  and  $\Phi_{\text{DF}}$  (photoluminescence quantum yield (PLQY) derived from prompt and delayed fluorescence),  $k_{\text{PF}}$  and  $k_{\text{DF}}$  (rate constant of prompt and delayed fluorescence),  $k_{\text{r}}^{\text{S}}$  and  $k_{\text{nr}}^{\text{S}}$  (rate constant of radiative and nonradiative decay from

excited singlet state, to be specific,  $S_1$ ),  $k_{nr}^T$  (rate constant of nonradiative decay from excited triplet state, to be specific,  $T_1$ ),  $\Phi_{ISC}$  and  $\Phi_{rISC}$  (ISC and rISC efficiency),  $k_{ISC}$  and  $k_{rISC}$  (rate constant of ISC and rISC)

$$k_{PF/DF} = \frac{1}{\tau_{PF/DF}}$$

$$k_{ISC} = \frac{\Phi_{DF}}{\Phi_{tot}} * k_{PF}$$

$$k_{RISC} = \frac{k_{PF}}{k_{ISC}} * \frac{\Phi_{DF}}{\Phi_{PF}} * k_{DF}$$

$$k_{r,S} = \Phi_{PF} * k_{PF}$$

$$k_{nr,S} = (1 - \Phi_{PF} - \Phi_{ISC}) * k_{PF}$$

After experimental measurement and analysis of photophysical properties,  $\Phi_{PF}$ ,  $\Phi_{DF}$ ,  $\tau_{PF}$  and  $\tau_{DF}$  could be directly calculated. Other rate constants and efficiencies for designated photophysical process were calculated by the formula and confirmed whether the values fit the assumption for derivation of the equation.

#### 2.2.4. OLED device fabrication and device test

OLED devices were fabricated on indium tin oxide (ITO)-patterned glass substrate using thermal evaporation under vacuum ( $P < 10^{-4}$  Pa). Detailed structure of the device and materials used were described at the discussion section. ITO-patterned glass substrates were rinsed by sonication with detergent-containing deionized water, acetone, and isopropyl alcohol, in the listed order. Sublimation-grade chemicals were used as purchased from commercial sources without further

sublimation, unless specifically mentioned. Target materials were used as emitter and sublimed two times before the device fabrication. mCPCN, used for host material, was synthesized according to the previously reported method<sup>17</sup> and sublimed two times before the device fabrication.

Each layer was deposited continuously following 20 minutes interval in order to prevent from intervening of particle formed during deposition and from increasing substrate temperature. Deposition rate was  $1.0 \text{ \AA s}^{-1}$  for organic layers,  $1.0 \text{ \AA s}^{-1}$  in total for the co-deposited organic layers,  $0.1 \text{ \AA s}^{-1}$  for LiF and  $2.0 \text{ \AA s}^{-1}$  for Al electrode, respectively. Customized aluminum masks for organic and inorganic material were applied during deposition to make the active layer of  $2 \text{ mm} \times 2 \text{ mm}$  square shape.

To evaluate performance of the OLED devices, the current–voltage–luminance (I–V–L) data were collected with Keithley 236 source-measure unit (Tektronix), Keithley 2000 multimeter unit (Tektronix) and a calibrated Si photodiode S5227-1010BQ (Hamamatsu). The luminance and the device efficiencies were calculated from the photocurrent measurement data obtained with the Si photodiode. The electroluminescence spectra were obtained by using a spectroradiometer CS-2000 (Konica Minolta).

## **2.3. Results and discussions**

### **2.3.1. Materials design and synthesis**

Synthesis of target molecules started from commercially available precursors, and completed by three steps of reaction including Friedel-Crafts acylation, condensation followed by Buchwald-Hartwig amination. Details of overall synthesis scheme, methods and structure analysis data were described in Supplementary Information. Whole synthetic routes were facile and the products were obtained with moderate yield.

### **2.3.2. Theoretical calculation**

Optimized molecular and orbital geometry, and energy levels were calculated using density functional theory (DFT) and time-dependent DFT (TD-DFT). Dihedral angles between the phenoxazine donor and oxadiazole acceptor ranged from 77° to 90° for all target molecules. From the torsion close to the right angle between donor and acceptor, highest occupied molecular orbitals (HOMOs) and lowest occupied molecular orbitals (LUMOs) could be definitely localized at the donor and acceptor, respectively, which lead to the small  $\Delta E_{ST}$  value for the materials. Interestingly, energy level of LUMOs, localized zone of which extended toward the auxiliary functional groups of the molecules, were affected by the electronic properties of the groups. Electron donating functional group made the LUMO level shallower (4'-DMAPXZOXD and 4'-MeOPXZOXD) than the reference material (PXZ-OXD),

whereas electron withdrawing functional group did the opposite way (4'-FPXZOXD, 4'-CF<sub>3</sub>PXZOXD and 4'-CNPXZOXD). As a result, calculated LUMO level had the difference up to 0.94eV between 4'-DMPXZOXD and 4'-CNPXZOXD. However, difference of calculated HOMO level was significantly reduced (~0.23eV), since the orbitals were localized only at the donor moiety for all molecules. Energy levels of the lowest excited state of each spin multiplicity were calculated. Since all materials have  $\Delta E_{ST}$  less than 0.05 eV, it was expected that TADF could be executed as expected from the distribution of HOMO-LUMO. After checking distribution of molecular orbital participating into excitation, both S<sub>1</sub> state and T<sub>1</sub> state were originated from intramolecular CT from donor part to acceptor part of the molecule. From which, direct ISC or rISC would not effectively according to the 3-level model. Next, excited state stemming from LE, which helps ISC or rISC process as a medium state, was scrutinized. In all target materials, lowest LE excited state of 10*H*-phenoxazine donor was calculated about 2.8 eV with triplet multiplicity. For 1,3,4-oxadiazole acceptor part, the value differed from 2.60 eV in 4'-DMPXZOXD to 3.21 eV in 4'-CNPXZOXD, as auxiliary functional group changes while keeping triplet multiplicity. As strong electron withdrawing functional group attached, electron density at acceptor part increased which led to higher excited triplet energy of LE state from acceptor.

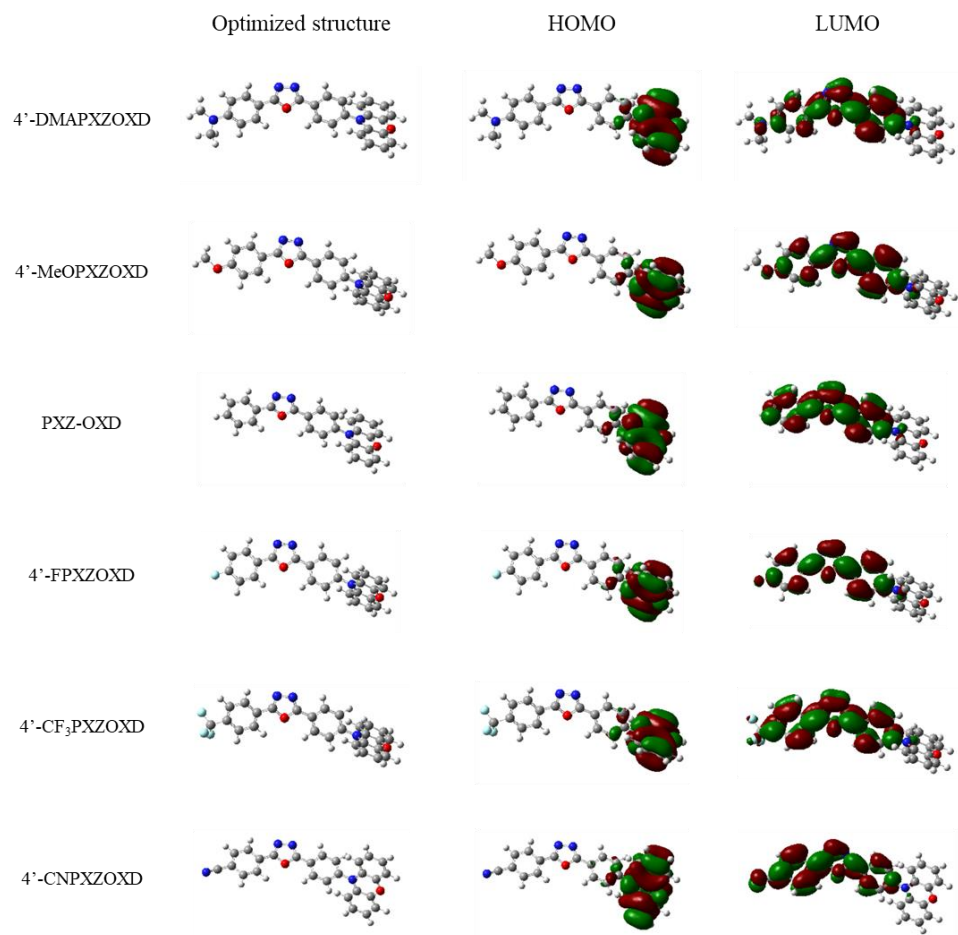


**Figure 2-2.** Optimized structure and distribution of HOMOs and LUMOs of the target materials from DFT calculation.

Material	HOMO (eV)	LUMO (eV)	S <sub>1</sub> (eV)	T <sub>1</sub> (eV)	$\Delta E_{ST}$ (eV)	Dihedral angle (deg.)
4'-DMAPXZOXD	-4.65	-1.56	2.4985	2.4893	0.0092	90.0
4'-MeOPXZOXD	-4.70	-1.73	2.4023	2.3935	0.0088	90.0
PXZ-OXD	-4.75	-1.89	2.3193	2.3033	0.0160	84.8
4'-FPXZOXD	-4.78	-1.92	2.3269	2.2852	0.0417	79.2
4'-CF <sub>3</sub> PXZOXD	-4.83	-2.20	2.1649	2.1331	0.0318	79.6
4'-CNPXZOXD	-4.88	-2.50	2.0011	1.9675	0.0336	77.0

**Table 2-1.** Selective parameters of 1,3,4-oxadiazole-based TADF emitters from DFT calculation.

### 2.3.3. Photophysical properties

Photophysical characteristics of the target materials were evaluated thoroughly. From the selected results, role of the auxiliary functional group toward photoluminescent and TADF properties could be delineated. First, energy levels of HOMOs and LUMOs were experimentally analyzed from UV-Vis absorption spectra and cyclic voltammetry graphs. Energy levels of HOMOs, calculated with oxidation onset voltage of cyclic voltammetry graph, were about -5 eV for all target materials and not related to the type of functional group. However, optical bandgap energy from onset wavelength of UV-Vis absorption graph was varied according to the functional group, which made different LUMO levels of -2.15 eV and -2.42 eV for 4'-DMPXZOXD and 4'-CNPXZOXD, respectively. As the calculation results depicted, electron withdrawing auxiliary functional group made LUMO level deeper, as the functional group decreased oxadiazole acceptor's electron density, making electron potential get lower.

Overall luminescent characteristics of the target materials were investigated through UV-Vis absorption spectra, steady-state photoluminescence (PL) spectra and PL quantum yields (PLQYs). In toluene solution, all target materials showed high absorbing structured band around 300nm and relatively low absorbing structureless band. Especially, the structureless absorbing band could be assigned as intramolecular CT absorption since the band slightly moves along with the intramolecular CT strength of the compound. Intramolecular CT characteristics had

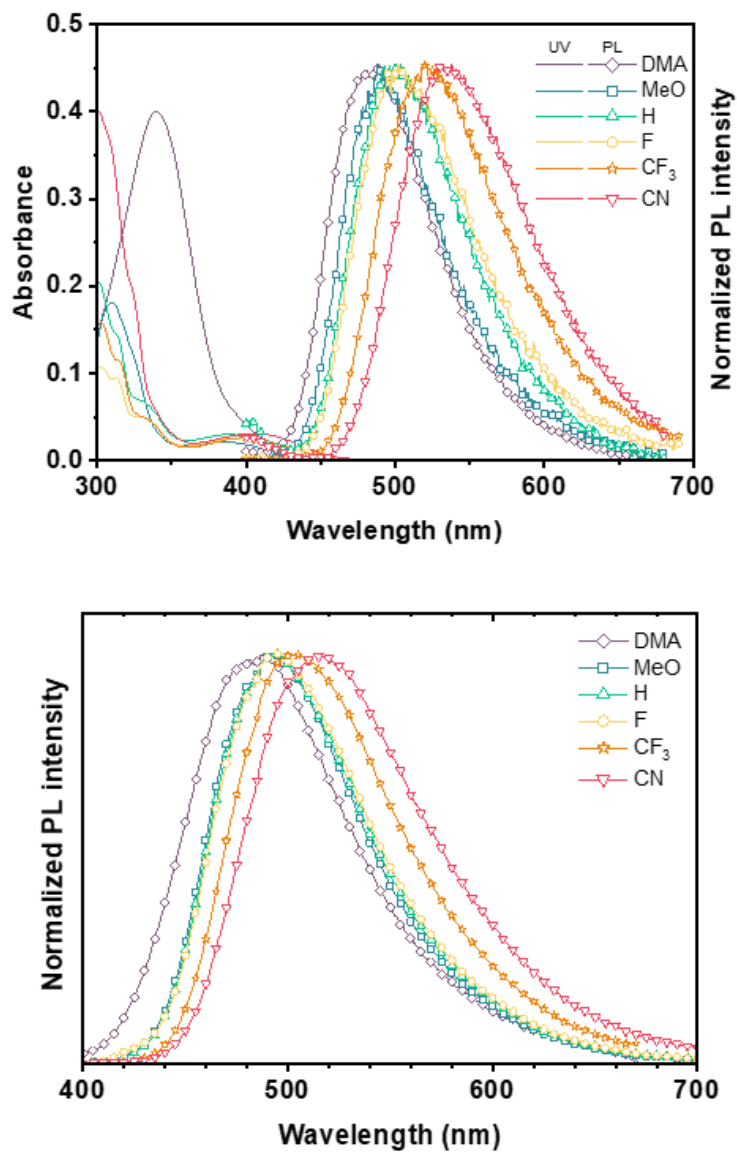


**Figure 2-3.** (upper) Absorption and emission spectra of target materials in toluene solution. (below) Emission spectra of target materials doped in mCPCN film.

Material	Solution (10 <sup>-5</sup> M in toluene)		Doped film (6wt.% in mCPCN)		S <sub>1</sub> /T <sub>1</sub> /ΔE <sub>S-T</sub> (eV)	HOMO (eV)	LUMO (eV)	τ <sub>PF</sub> (ns)	τ <sub>DF</sub> (μs)
	λ <sub>abs</sub> (nm)	λ <sub>PL</sub> (nm)	λ <sub>PL</sub> (nm)	Φ <sub>PL</sub> (%)					
4'-DMAPXZOXD	339	486	487	31.7	3.008/2.736/0.272	-5.06	-2.15	7.35	N/A
4'-MeOPXZOXD	302,385	497	493	65.8	2.870/2.772/0.098	-5.07	-2.23	10.2	N/A
PXZ-OXD	301,389	496	493	74.0	2.836/2.731/0.105	-5.06	-2.27	17.9	14.5
4'-FPXZOXD	298,389	502	495	61.3	2.836/2.737/0.099	-5.09	-2.29	11.3	20.6
4'-CF <sub>3</sub> PXZOXD	302,396	521	501	81.1	2.758/2.746/0.012	-5.08	-2.36	13.8	5.14
4'-CNPXZOXD	297,404	533	513	86.8	2.718/2.677/0.041	-5.09	-2.42	18.6	5.29

**Table 2-2.** Photophysical parameters of 1,3,4-oxadiazole-based TADF emitters from experiments.

major role in the PL spectra, giving structureless graph and emission range varying with the intramolecular CT strength. 4'-DMAPXZOXD with the strongest EDG substituted at the acceptor moiety had PL emission peak at 486nm, whilst 4'-CNPXZOXD with the strongest EWG had PL emission peak at 533nm. Difference up to 47nm in the PL emission peak throughout the series of target materials was smaller than in the series of compounds from conventional molecular design strategy, which alters core donor or acceptor moiety to totally different chemical group.<sup>8,18</sup> In the thin film doped in mCPCN as host, the tendency of emission range was kept with much lower difference between 4'-DMAPXZOXD and 4'-CNPXZOXD. Absolute PLQYs of the film samples were measured using integrating sphere, scoring the highest value of 86.8% for 4'-CNPXZOXD.

To verify the potential of rISC in target compounds, fluorescence and phosphorescence spectra in 77K were measured to calculate  $S_1$  and  $T_1$  levels. All spectra showed structureless single-peaked graph, indicating that intramolecular charge transfer state rather than locally excited state of donor or acceptor part was related to the lowest excited state. Influence of intramolecular CT characteristics on  $S_1$  and  $T_1$  state could be found in tendency of emission range, which is same as in the room-temperature PL spectra.  $\Delta E_{ST}$  calculated from onset of fluorescence and phosphorescence spectra decreased when stronger electron withdrawing group attached, which made  $\Delta E_{ST}$  value of 4'-CF<sub>3</sub>PXZOXD and 4'-CNPXZOXD lower than 0.05eV. However, strong electron donating dimethylamino group in 4'-DMAPXZOXD made  $\Delta E_{ST}$  increased up to 0.272eV, indicating remarkably reduced

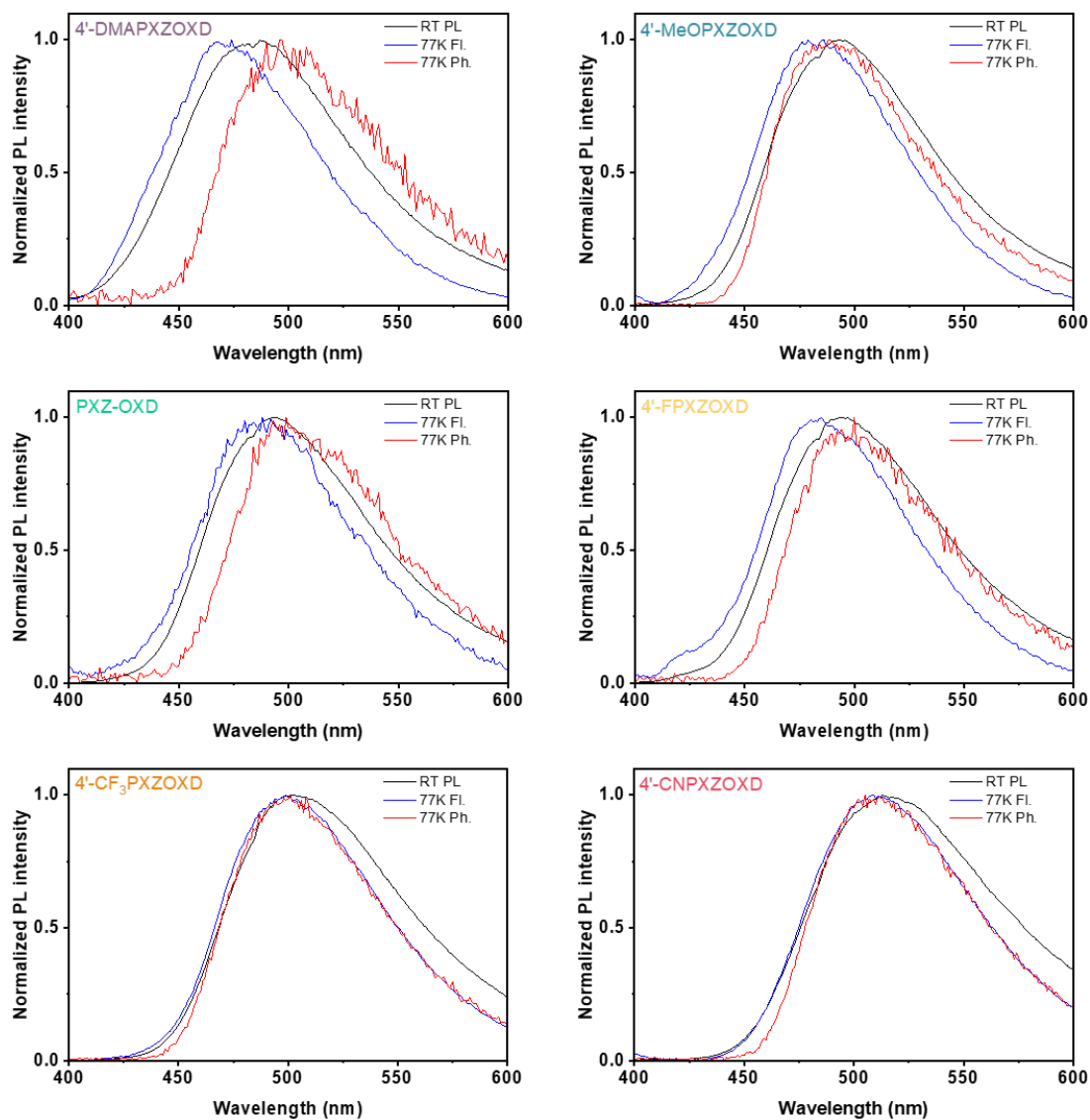


**Figure 2-4.** Low temperature PL spectra of the target materials doped in mCPCN film.

chance of TADF.

Delayed fluorescence was directly observed via transient PL decay profile. At the low temperature ca. 100K, all thin film samples of target materials didn't show PL decay lifetime about  $10^1$   $\mu$ s order or longer, which is commonly known decay lifetime of D-A combined TADF compound. However, as the temperature increased, some compounds exhibited PL decay lasting more than microsecond time range. Lifetime of delayed fluorescence of 4'-CF<sub>3</sub>PXZOXD and 4'-CNPXZOXD didn't exceed 10 $\mu$ s, which could be described from efficient rISC by reduced  $\Delta E_{ST}$  value. PXZ-OXD and 4'-FPXZOXD also showed delayed fluorescence with lifetime from 14.5 $\mu$ s to 20.6 $\mu$ s, but not conspicuous as abovementioned compounds because of increased  $\Delta E_{ST}$ . The delayed fluorescence observed could be concluded as TADF from that all delayed fluorescence appeared and got intensified as temperature increased. In 4'-DMPXZOXD and 4'-MeOPXZOXD, delayed fluorescence wasn't founded, as expected from low-temperature PL analysis.

#### 2.3.4. Rate constant study

From lifetime data of transient PL decay graph combined with the measured fluorescence performances, rate constant study was carried out following the formula in reference.<sup>19</sup> Rate constants and quantum efficiencies of selected photophysical transitions are listed at Table S3. Contrary to the expectation that reduced  $\Delta E_{ST}$  in electron-withdrawing-group-attached compounds enhances TADF performance so that the portion of delayed fluorescence toward PLQY ( $f_{DF}$ ) increase, calculated  $f_{DF}$

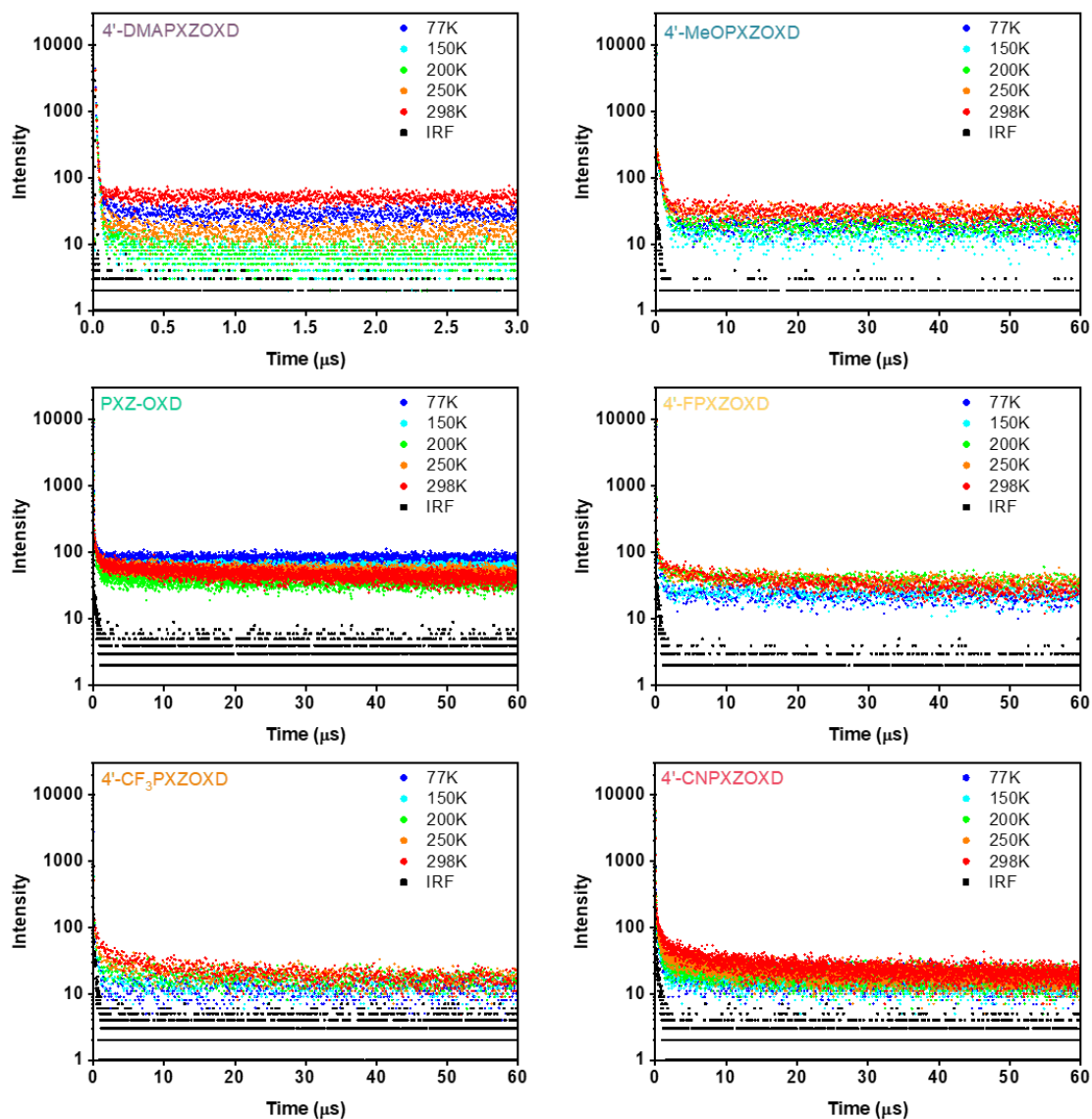


**Figure 2-5.** Time-resolved radiative decay profile of target materials doped in mCPCN film in various temperatures.

also reduced as  $\Delta E_{ST}$  reduced. This could be elucidated from high rate constant of radiative decay in  $S_1$  state ( $k_{rad,S}$ ), guiding photoexcited singlet exciton directly to prompt fluorescence rather than quantum-mechanically prohibited ISC in spite of small energy difference. However, at the same time, tendency of rate constant of rISC ( $k_{rISC}$ ) matched with tendency of  $\Delta E_{ST}$ ,  $k_{rISC}$  scoring high as  $4.12 \times 10^5 \text{ s}^{-1}$  in 4'-CNPXZOXD while low as  $2.37 \times 10^5 \text{ s}^{-1}$  in 4'-FPXZOXD. From the result, small  $\Delta E_{ST}$  value played an important role toward photophysical properties in two ways – increasing  $k_{rad,S}$  and  $k_{rISC}$ , which predicted that 4'-CNPXZOXD become a high-performance TADF emitter for OLED among the target compounds.

Material	$\Phi_{\text{tot}}$ (%)	$\Phi_{\text{PF}}$ (%)	$\Phi_{\text{DF}}$ (%)	$\tau_{\text{PF}}$ (ns)	$\tau_{\text{DF}}$ ( $\mu\text{s}$ )	$k_{\text{PF}}$ ( $10^7 \text{ s}^{-1}$ )	$k_{\text{DF}}$ ( $10^4 \text{ s}^{-1}$ )	$k_{\text{r},\text{S1}}$ ( $10^7 \text{ s}^{-1}$ )	$k_{\text{nr},\text{S1}}$ ( $10^7 \text{ s}^{-1}$ )	$k_{\text{ISC}}$ ( $10^7 \text{ s}^{-1}$ )	$k_{\text{rISC}}$ ( $10^8 \text{ s}^{-1}$ )
4'-DMAPXZOXD	31.7	31.7	-	7.35	-	13.6	-	4.31	9.29	-	-
4'-MeOPXZOXD	65.8	65.8	-	10.2	-	9.80	-	6.45	3.35	-	-
PXZ-OXD	74.0	15.2	58.8	17.9	14.5	5.59	6.89	0.849	0.298	4.44	3.35
4'-FPXZOXD	61.3	12.6	48.7	11.3	20.6	8.85	4.85	1.11	0.702	7.03	2.37
4'-CF <sub>3</sub> PXZOXD	81.1	47.7	33.4	13.8	5.14	7.25	19.5	3.45	0.805	2.99	3.31
4'-CNPXZOXD	86.8	39.8	47.0	18.6	5.29	5.38	18.9	2.14	0.325	2.91	4.12

**Table 2-3.** Rate constants and other photophysical parameters of 1,3,4-oxadiazole-based TADF emitters.

### 2.3.5. OLED device performance

To evaluate electric device performance of the target materials, OLED devices were fabricated as a stacked layers of ITO / HAT-CN (5 nm) / TAPC (30 nm) / mCP (10 nm) / 6wt.% emitter : mCPCN (20 nm) / TmPyPB (10 nm) / 3TPYMB (50 nm) / LiF (0.7 nm) / Al (100 nm). (ITO: indium tin oxide, served as an anode, HAT-CN: 1,4,5,8,9,11-hexaazatriphenylenehexacarbonitrile, served as a hole-injecting material, TAPC: 4,4'-cyclohexylidenebis[*N,N'*-bis(4-methylphenyl)benzenamine], served as a hole transporting material, mCP: 1,3-bis(9*H*-carbazol-9-yl)benzene, served as an exciton blocking material, mCPCN: 9-(3-(9*H*-carbazol-9-yl)phenyl)-9*H*-carbazole-3-carbonitrile, served as a host, TmPyPB: 1,3,5-tri(*m*-pyridin-3-ylphenyl)benzene, served as an exciton blocking material, 3TPYMB: tri[3-(3-pyridyl)mesityl]borane, served as an electron transporting material, LiF as an electron injecting material, Al as a cathode) OLED device with the referential PXZ-OXD as emitter showed maximum EQE of 18.7% and emission spectrum peaking at 496nm, which is comparable to the data of 2PXZ-OXD reported in advance.<sup>16</sup> Tendency of the electroluminescence spectrum among the target materials was same as in the PL spectrum except 4'-FPXZOXD; the auxiliary fluorine of 4'-FPXZOXD is weak electron-withdrawing group but electron-rich, making incoming barrier of exciton higher and emission range slightly blue-shifted in the electroluminescence situation.<sup>20</sup> Internal Commission on Illumination (Commission international de l'éclairage, CIE) coordinate of the OLED device with PXZ-OXD was (0.25,0.43), and the coordinate of other series of the device didn't deviated remarkably from the

referential one, featuring bluegreen to green emission to the naked eye. EQE of the device with 4'-CNPXOXD recorded up to 21.3%, which was facilitated by efficient rISC and high radiation rate constant from the  $S_1$  state. Other series of the device showed EQE analogous to the PXZ-OXD device, showing potential of oxadiazole core as acceptor for the highly efficient TADF emitter when properly modified and combined with donor.

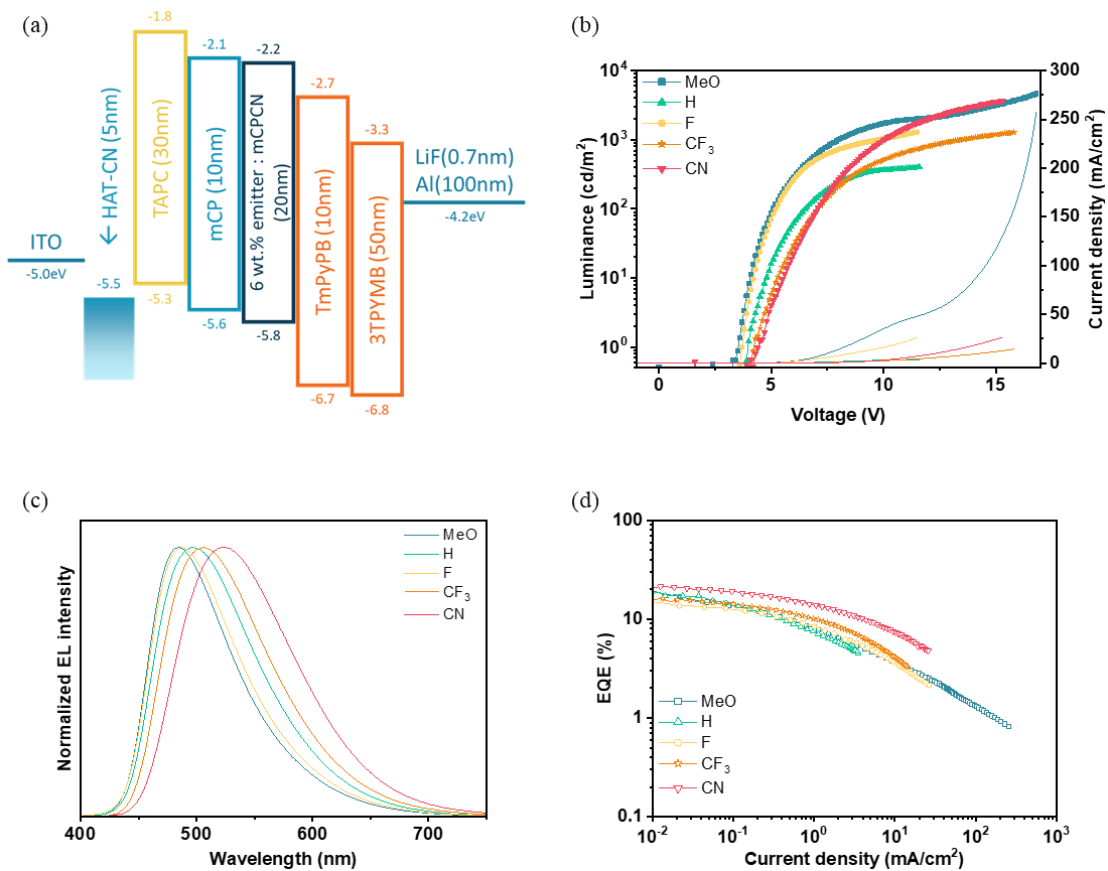


**Figure 2-6.** (a) Structure of OLED device. (b) J-V-L curve of the OLED device. (c) Electroluminescence spectrum of the OLED device. (d) External quantum efficiency graph of the OLED device.

Emitter	$V_{on}$ (V)	EQE (%)	$\lambda_{EL}$ (nm)	CIE coordinate
<b>4'-MeOPXZOXD</b>	3.9	18.1	484	(0.21, 0.37)
<b>PXZ-OXD</b>	4.5	18.7	496	(0.25, 0.43)
<b>4'-FPXZOXD</b>	4.0	14.6	488	(0.22, 0.39)
<b>4'-CF<sub>3</sub>PXZOXD</b>	4.9	16.1	507	(0.27, 0.48)
<b>4'-CNPXZOXD</b>	5.3	21.3	525	(0.33, 0.52)

**Table 2-4.** Performance of OLED device using 1,3,4-oxadiazole-based TADF emitters.

## 2.4. Conclusions

In summary, series of PXZ-OXD derivatives with various auxiliary functional groups were developed to find role of intramolecular CT characteristics in D-A type TADF emitter. Unlike traditional molecular design strategy, auxiliary functional group moderated excited energy state and emissive rate constants with suppressed spectral shift. From the strategy, 4'-CNPXZOXD containing strong electron-withdrawing nitrile group among newly introduced compounds in this work showed EQE up to 21% in OLED device. By controlling auxiliary functional group's electric characteristics properly, D-A type TADF emitter could be enhanced in its rISC performance without changing its main donor and acceptor pair.

## 2.5. References

1. Tang, C. W.; VanSlyke, S. A., Organic electroluminescent diodes. *Applied Physics Letters* **1987**, *51* (12), 913-915.
2. Baldo, M. A.; O'Brien, D. F.; You, Y.; Shoustikov, A.; Sibley, S.; Thompson, M. E.; Forrest, S. R., Highly efficient phosphorescent emission from organic electroluminescent devices. *Nature* **1998**, *395* (6698), 151-154.
3. Baldo, M. A.; Lamansky, S.; Burrows, P. E.; Thompson, M. E.; Forrest, S. R., Very high-efficiency green organic light-emitting devices based on electrophosphorescence. *Applied Physics Letters* **1999**, *75* (1), 4-6.
4. Bin, J.-K.; Cho, N.-S.; Hong, J.-I., New Host Material for High-Performance Blue Phosphorescent Organic Electroluminescent Devices. *Advanced Materials* **2012**, *24* (21), 2911-2915.
5. Endo, A.; Sato, K.; Yoshimura, K.; Kai, T.; Kawada, A.; Miyazaki, H.; Adachi, C., Efficient up-conversion of triplet excitons into a singlet state and its application for organic light emitting diodes. *Applied Physics Letters* **2011**, *98* (8), 083302.
6. Kaji, H.; Suzuki, H.; Fukushima, T.; Shizu, K.; Suzuki, K.; Kubo, S.; Komino, T.; Oiwa, H.; Suzuki, F.; Wakamiya, A.; Murata, Y.; Adachi, C., Purely organic electroluminescent material realizing 100% conversion from electricity to light. *Nature Communications* **2015**, *6* (1), 8476.
7. Lin, T. A.; Chatterjee, T.; Tsai, W. L.; Lee, W. K.; Wu, M. J.; Jiao, M.; Pan, K. C.; Yi, C. L.; Chung, C. L.; Wong, K. T.; Wu, C. C., Sky-Blue Organic Light Emitting Diode with 37% External Quantum Efficiency Using Thermally Activated Delayed Fluorescence from Spiroacridine-Triazine Hybrid. *Advanced Materials* **2016**, *28* (32), 6976-6983.
8. Pan, K.-C.; Li, S.-W.; Ho, Y.-Y.; Shiu, Y.-J.; Tsai, W.-L.; Jiao, M.; Lee, W.-K.; Wu, C.-

- C.; Chung, C.-L.; Chatterjee, T.; Li, Y.-S.; Wong, K.-T.; Hu, H.-C.; Chen, C.-C.; Lee, M.-T., Efficient and Tunable Thermally Activated Delayed Fluorescence Emitters Having Orientation-Adjustable CN-Substituted Pyridine and Pyrimidine Acceptor Units. *Advanced Functional Materials* **2016**, *26* (42), 7560-7571.
9. Zeng, W.; Zhou, T.; Ning, W.; Zhong, C.; He, J.; Gong, S.; Xie, G.; Yang, C., Realizing 22.5% External Quantum Efficiency for Solution-Processed Thermally Activated Delayed-Fluorescence OLEDs with Red Emission at 622 nm via a Synergistic Strategy of Molecular Engineering and Host Selection. *Advanced Materials* **2019**, *31* (33), 1901404.
  10. Tao, Y.; Yuan, K.; Chen, T.; Xu, P.; Li, H.; Chen, R.; Zheng, C.; Zhang, L.; Huang, W., Thermally Activated Delayed Fluorescence Materials Towards the Breakthrough of Organoelectronics. *Advanced Materials* **2014**, *26* (47), 7931-7958.
  11. Im, Y.; Kim, M.; Cho, Y. J.; Seo, J.-A.; Yook, K. S.; Lee, J. Y., Molecular Design Strategy of Organic Thermally Activated Delayed Fluorescence Emitters. *Chemistry of Materials* **2017**, *29* (5), 1946-1963.
  12. Kitamoto, Y.; Namikawa, T.; Ikemizu, D.; Miyata, Y.; Suzuki, T.; Kita, H.; Sato, T.; Oi, S., Light blue and green thermally activated delayed fluorescence from 10H-phenoxaborin-derivatives and their application to organic light-emitting diodes. *Journal of Materials Chemistry C* **2015**, *3* (35), 9122-9130.
  13. Cao, X.; Zhang, X.; Duan, C.; Xu, H.; Yuan, W.; Tao, Y.; Huang, W., Simple phenyl bridge between cyano and pyridine units to weaken the electron-withdrawing property for blue-shifted emission in efficient blue TADF OLEDs. *Org. Electron.* **2018**, *57*, 247-254.
  14. Ryoo, C. H.; Cho, I.; Han, J.; Yang, J.-h.; Kwon, J. E.; Kim, S.; Jeong, H.; Lee, C.; Park, S. Y., Structure–Property Correlation in Luminescent Indolo[3,2-b]indole (IDID) Derivatives: Unraveling the Mechanism of High Efficiency Thermally Activated Delayed Fluorescence (TADF). *ACS Appl. Mater. Interfaces* **2017**, *9* (47), 41413-41420.

15. Park, I. S.; Min, H.; Yasuda, T., Phenyl-triggered photophysical switching between normal fluorescence and delayed fluorescence in phthalonitrile-based luminophores. *Aggregate* **2021**, 2 (1), 145-150.
16. Lee, J.; Shizu, K.; Tanaka, H.; Nomura, H.; Yasuda, T.; Adachi, C., Oxadiazole- and triazole-based highly-efficient thermally activated delayed fluorescence emitters for organic light-emitting diodes. *Journal of Materials Chemistry C* **2013**, 1 (30), 4599-4604.
17. Lin, M.-S.; Yang, S.-J.; Chang, H.-W.; Huang, Y.-H.; Tsai, Y.-T.; Wu, C.-C.; Chou, S.-H.; Mondal, E.; Wong, K.-T., Incorporation of a CN group into mCP: a new bipolar host material for highly efficient blue and white electrophosphorescent devices. *Journal of Materials Chemistry* **2012**, 22 (31), 16114-16120.
18. Park, I. S.; Lee, S. Y.; Adachi, C.; Yasuda, T., Full-Color Delayed Fluorescence Materials Based on Wedge-Shaped Phthalonitriles and Dicyanopyrazines: Systematic Design, Tunable Photophysical Properties, and OLED Performance. *Advanced Functional Materials* **2016**, 26 (11), 1813-1821.
19. Kobayashi, T.; Niwa, A.; Takaki, K.; Haseyama, S.; Nagase, T.; Goushi, K.; Adachi, C.; Naito, H., Contributions of a Higher Triplet Excited State to the Emission Properties of a Thermally Activated Delayed-Fluorescence Emitter. *Physical Review Applied* **2017**, 7 (3), 034002.
20. Ragni, R.; Punzi, A.; Babudri, F.; Farinola, G. M., Organic and Organometallic Fluorinated Materials for Electronics and Optoelectronics: A Survey on Recent Research. *European Journal of Organic Chemistry* **2018**, 2018 (27-28), 3500-3519.

## **Chapter 3.**

# **1,8-Naphthalimide Acceptor for Efficient Red TADF Emitter**

### **3.1. Research background**

Red-to-Near Infrared (NIR) light-emitting devices have been widely used beyond the traditional display industry, for communication, security, and bioapplication. However, red emitters have lower limit in luminous efficiency than other primary colors of light – blue and green – described in energy gap law<sup>1</sup>. Accordingly, there have been numerous studies<sup>2-5</sup> on highly emissive red-to-NIR emitter from various viewpoints. Phosphors including heavy metal complexes<sup>6</sup> show efficient red-to-NIR emission through proper combination of core metal and ligand, but they also suffer from efficiency roll-off in high-current light emitting devices because of harsh quenching tendency of excited triplet states which are related to emission. In case of conventional fluorophores, only the excited singlet state is involved in luminescence, there is a considerable limitation in terms of internal quantum efficiency (IQE) because fluorophore harvests a quarter of electrically generated excitons as singlet states. As a breakthrough in exciton harvesting, C. Adachi and his colleagues<sup>7</sup> introduced thermally activated delayed fluorescence (TADF) into light-emitting devices. After the first application in organic light

emitting diode (OLED), TADF emitters have been drawn a great attention to realize highly luminescent OLEDs.

In TADF emitter, excited triplet states created from electrical excitation can be converted into excited singlet states via reverse intersystem crossing (rISC), which overcomes the limit of conventional fluorophores in terms of IQE. From this, vigorous studies on overall photophysical process and universal material design strategy related to TADF emitter have been done to raise its performance. The common knowledge to date is that the TADF emitter need to reduce the energy between excited singlet state and triplet state ( $\Delta E_{ST}$ ) which is related to the hurdle of rISC process, and this could be achieved by designing emitter molecule with a twisted linkage of electron donor (D) and acceptor (A). Numerous donors represented by amines and acceptors represented by electron withdrawing groups and heterocyclic compounds have been reported so far. Among various acceptors, pyrazine<sup>8</sup>, heptaazaphenylene<sup>9</sup>, and quinoxaline<sup>10</sup> have strong electron withdrawing ability and are used as the core of efficient red-to-NIR TADF emitters.

Other than these, highly efficient red-to-NIR TADF emitters based on naphthalimide acceptor core have been reported<sup>11,12</sup>, which include the material with electroluminescence (EL) peak at around 600nm and external quantum efficiency (EQE) of 30% in the OLED device without any special treatment after device fabrication. Although the emitters based on naphthalimide have bright enough emission in the device, they are expected to show more potential for deeper red emission. Considering a low excited triplet state level of naphthalimide<sup>13</sup>, deeper red

emission could be satisfied by relaxation of excited state from strong intramolecular charge transfer (CT) of D-A structure including naphthalimide as acceptor moiety.

In this chapter, with reference to the reported material, deeper red emission in naphthalimide core while maintaining outstanding TADF properties was made by (1) making acceptor stronger by applying trifluoromethyl group ( $-\text{CF}_3$ ) as an auxiliary electron withdrawing group (EWG), or (2) using stronger arylamine donor. All TADF emitters, including already-reported PNIDMAC (“6AcBIQ” in the reference<sup>11</sup>), were fully studied in photophysical characteristics and device performances. It was confirmed that the molecular design strategies toward efficient red-to-NIR TADF emitter were valid by observing the EL spectrum peak at 600nm or longer. From the molecules, maximum EQE of 12.7% was acquired from diCF3PNIDMAC and the deepest red emission with emission maximum at 641nm was observed from diCF3PNIPXZ.

## 3.2. Experimental method

### 3.2.1. Materials and synthesis

All target materials were synthesized in a two-step reaction from naphthalic anhydride. Chemicals for synthesis of the target materials were used as purchased from commercial suppliers, without further purification. Thin layer chromatography (TLC) plate (silica gel 60 F254, Merck Co.) and silica gel 60 (particle size 0.063 – 0.200mm, Merck co.) were used to judge the reaction progress and for column chromatographic purification.

Chemical structures of the final target materials were assigned by analyzing nuclear magnetic resonance (NMR) spectra, mass spectra and elemental analysis (EA) data. <sup>1</sup>H-NMR data of the target materials were recorded on Avance-300 (Bruker), and <sup>13</sup>C-NMR data were recorded on Avance-500 (Bruker). Mass spectra of the target materials were obtained with JMS-700 (JEOL) and 6890 series (Agilent). EA of carbon, hydrogen and nitrogen of the target materials was executed with Flash2000 (ThermoFisher Scientific).

#### *Synthesis of 6-bromo-2-phenyl-1H-benzo[de]isoquinoline-1,3(2H)-dione (PNIBr)*

A mixture of 4-bromo-1,8-naphthalic anhydride (5.00 g, 18.05 mmol), aniline (2.47 mL, 27.07 mmol) and acetic acid (100 mL) was refluxed for 24 hours. After the reaction finished, the mixture was cooled down to room temperature and poured

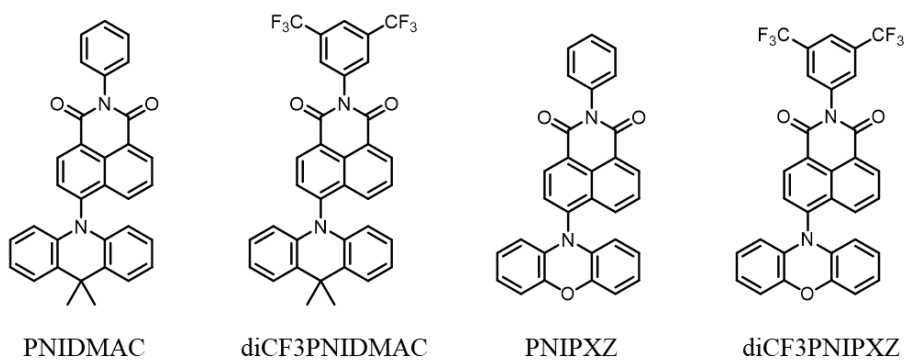


**Figure 3-1.** Chemical structure and synthetic route of the target materials.

into water to precipitate material. Crude precipitate material was filtered and recrystallized from mixed solvent of chloroform and methanol to afford the product as pale yellow solid (2.68 g, yield: 42.2 %). <sup>1</sup>H NMR (300 MHz, DMSO-*d*<sub>6</sub>) δ: 8.61 (t, *J* = 7.5 Hz, 2H), 8.37 (d, *J* = 9.0 Hz, 1H), 8.28 (d, *J* = 9.0 Hz, 1H), 7.56-7.47 (m, 3H), 7.40 (d, *J* = 9.0 Hz, 2H).

*Synthesis of 6-(9,9-dimethylacridin-10(9H)-yl)-2-phenyl-1H-benzo[de]isoquinoline-1,3(2H)-dione (PNIDMAC)*

To a dehydrated round-bottomed flask connected with a reflux condenser, a mixture of PNIBr (1.25 g, 3.55 mmol), 9,10-dihydro-9,9-dimethylacridine (817 mg, 3.90 mmol), bis(tri-*tert*-butylphosphine)palladium(0) (30 mg, 0.06 mmol), sodium *tert*-butoxide (682 mg, 7.10 mmol), and anhydrous toluene (40 mL) was refluxed under inert atmosphere filled with Ar for 24 hours. After the reaction finished, the mixture was cooled down to room temperature and the solvent was removed under reduced pressure, followed by extraction with brine and dichloromethane. The organic layer was dried with MgSO<sub>4</sub> and concentrated under reduced pressure. The residual solid crude material was purified by column chromatography on silica gel using mixture solvent of ethyl acetate / n-hexane (v:v 1:5) and recrystallized from mixed solvent of chloroform and methanol to afford 6-(9,9-dimethylacridin-10(9H)-yl)-2-phenyl-1H-benzo[de] isoquinoline-1,3(2H)-dione (**PNIDMAC**) as orange powder (800 mg, yield: 46.9 %). <sup>1</sup>H NMR (300MHz, CDCl<sub>3</sub>) δ: 8.87 (d, *J* = 7.7 Hz, 1H), 8.69 (d, *J* = 7.3 Hz, 1H), 8.10 (d, *J* = 8.4 Hz, 1H), 7.84 (d, *J* = 7.7 Hz, 1H), 7.68

(dd,  $J_1 = 8.4$  Hz,  $J_2 = 7.3$  Hz, 1H), 7.64-7.48 (m, 5H), 7.37 (d,  $J = 6.9$  Hz, 2H), 6.97 (t,  $J = 7.5$  Hz, 2H), 6.88 (t,  $J = 7.7$  Hz, 2H), 5.99 (d,  $J = 8.1$  Hz, 2H), 1.86 (s, 3H), 1.78 (s, 3H).  $^{13}\text{C}$  NMR (125MHz,  $\text{CDCl}_3$ )  $\delta$ : 164.28, 163.95, 144.74, 140.28, 135.46, 133.18, 132.58, 131.09, 131.03, 130.87, 130.71, 130.16, 129.69, 129.06, 128.82, 128.31, 126.94, 126.22, 124.08, 123.33, 121.52, 114.22, 77.47, 77.22, 76.96, 36.27, 32.98, 32.32. HRMS  $m/z$ : calc.d for  $\text{C}_{33}\text{H}_{24}\text{N}_2\text{O}_2$ , 480.18; found, 480.7970. EA: calc.d for  $\text{C}_{33}\text{H}_{24}\text{N}_2\text{O}_2$ , C 82.48, H 5.03, N 5.83; found, C 82.13, H 4.94, N 5.67.

*Synthesis of 2-(3,5-bis(trifluoromethyl)phenyl)-6-bromo-1H-benzo[de]isoquinoline-1,3(2H)-dione (diCF<sub>3</sub>PNIBr)*

A mixture of 4-bromo-1,8-naphthalic anhydride (5.00 g, 18.05 mmol), 3,5-bis(trifluoromethyl)aniline (4.21 mL, 27.07 mmol), zinc acetate (5.30 g, 28.87 mmol) and quinoline (100 mL) was refluxed for 36 hours. After the reaction finished, the mixture was cooled down to room temperature and extracted with deionized water and dichloromethane. The organic layer was dried with  $\text{MgSO}_4$  and concentrated under reduced pressure. The residual viscous crude material was purified by column chromatography on silica gel using dichloromethane as eluent and recrystallized from mixed solvent of chloroform and methanol to afford the product as white powder (4.32 g, yield: 49.0 %).  $^1\text{H}$  NMR (300 MHz,  $\text{DMSO}-d_6$ )  $\delta$ : 8.65 (dd,  $J_1 = 13.5$  Hz,  $J_2 = 6.0$  Hz, 2H), 8.40 (d,  $J = 9.0$  Hz, 1H), 8.31 (m, 4H), 8.08 (t,  $J = 9.0$  Hz, 1H).

*Synthesis of 2-(3,5-bis(trifluoromethyl)phenyl)-6-(9,9-dimethylacridin-10(9H)-yl)-1H-benzo[de]isoquinoline-1,3(2H)-dione (diCF<sub>3</sub>PNIDMAC)*

To a dehydrated round-bottomed flask connected with a reflux condenser, a mixture of diCF<sub>3</sub>PNIBr (1.70 g, 3.48 mmol), 9,10-dihydro-9,9-dimethylacridine (802 mg, 3.83 mmol), Pd catalyst (50 mg, 0.10 mmol), sodium *tert*-butoxide (670 mg, 6.97 mmol), and anhydrous toluene (50 mL) was refluxed under inert atmosphere filled with Ar for 24 hours. After the reaction finished, the mixture was cooled down to room temperature and the solvent was removed under reduced pressure, followed by extraction with brine and dichloromethane. The organic layer was dried with MgSO<sub>4</sub> and concentrated under reduced pressure. The residual solid crude material was purified by column chromatography on silica gel using mixture solvent of ethyl acetate / n-hexane (v:v 1:5) and recrystallized from mixed solvent of chloroform and methanol to afford 2-(3,5-bis(trifluoromethyl)phenyl)-6-(9,9-dimethylacridin-10(9H)-yl)-1H-benzo[de]isoquinoline-1,3(2H)-dione (diCF<sub>3</sub>PNIDMAC) as orange powder (1.37 g, yield: 63.8 %). <sup>1</sup>H NMR (300MHz, CDCl<sub>3</sub>) δ: 8.90 (d, *J* = 7.7 Hz, 1H), 8.71 (d, *J* = 7.3 Hz, 1H), 8.16 (d, *J* = 8.4 Hz, 1H), 8.03 (s, 1H), 7.88 (d, *J* = 7.7 Hz, 3H), 7.72 (dd, *J*<sub>1</sub> = 8.4 Hz, *J*<sub>2</sub> = 7.3 Hz, 1H), 7.56 (d, *J* = 7.7 Hz, 2H), 6.98 (t, *J* = 7.5 Hz, 2H), 6.88 (t, *J* = 7.7 Hz, 2H), 5.96 (d, *J* = 8.2 Hz, 2H), 1.86 (s, 3H), 1.79 (s, 3H). <sup>13</sup>C NMR (125MHz, CDCl<sub>3</sub>) δ: 163.88, 163.54, 145.53, 140.23, 136.84, 133.67, 133.21, 133.05, 132.94, 132.66, 131.43, 131.30, 130.86, 130.23, 129.97, 128.49, 127.20, 126.98, 126.87, 126.30, 124.20, 123.41, 123.14, 123.12, 122.62, 122.03, 121.67, 114.16, 77.48, 77.22, 76.97, 36.30, 32.96,

32.32. HRMS  $m/z$ : calc.d for  $C_{35}H_{22}F_6N_2O_2$ , 616.16; found, 616.5025. EA: calc.d for  $C_{35}H_{22}F_6N_2O_2$ , C 68.18, H 3.60, N 4.54; found, C 67.92, H 3.61, N 4.42.

### 3.2.2. Quantum chemical calculation

All quantum chemical calculations were carried out using the Gaussian 09 quantum chemical package. Geometry optimization in the ground state was performed using density functional theory (DFT) method with B3LYP functional / 6-31G(d,p) basis set. Energy levels of the ground state and some excited state with singlet or triplet multiplicity were calculated using time-dependent DFT (TD-DFT) method with B3LYP functional / 6-31G(d,p) basis set.

### 3.2.3. Photophysical and electrochemical characterization

Solution samples for cyclic voltammetry (CV) measurement were prepared as concentration of  $5 \times 10^{-3}$  M in methylene chloride, with 0.1 M TBAHFP as the supporting electrolyte. Solution samples for other photophysical characterizations were prepared as concentrations of  $10^{-5}$  M in toluene. Film samples were fabricated on quartz substrate using thermal evaporation under vacuum ( $P < 10^{-4}$  Pa), with co-deposition rate of  $1.0 \text{ \AA s}^{-1}$  in total for the emitter and host material. Quartz substrates were rinsed by sonication with detergent-containing deionized water, acetone, and isopropyl alcohol, in the listed order.

CV was performed on 273A (Princeton Applied Research) using a three-electrode solution container cell. Three electrodes include an Ag wire in 0.01 M

AgNO<sub>3</sub> solution as a reference electrode, a carbon disc as a working electrode, and a Pt wire as a counter electrode. The redox potential of the reference electrode was calibrated using ferrocene/ferrocenium (Fc/Fc<sup>+</sup>) as an internal standard. For steady-state photophysical studies, UV-1650PC (Shimadzu) for UV-Vis absorption spectra, QuantaMaster 40 (Photon Technology International) for room temperature photoluminescence spectra, Cary Eclipse fluorescence spectrophotometer (Varian) for low temperature photoluminescence spectra were used, respectively. In order to remove background data, quartz cuvette filled with toluene, which was the solvent for the solution samples, or blank quartz substrate was used for the steady-state photophysical studies. Time-dependent photoluminescence decay profiles were observed by FluoTime 200 (PicoQuant) and analyzed by time-correlated single photon counting technique.

### 3.2.4. Equations for rate constants

According to the reference,<sup>14</sup> equations below were used to calculate rate constants related to TADF process. Symbols used for terminologies were described as follows:  $\Phi_{\text{PF}}$  and  $\Phi_{\text{DF}}$  (photoluminescence quantum yield (PLQY) derived from prompt and delayed fluorescence),  $k_{\text{PF}}$  and  $k_{\text{DF}}$  (rate constant of prompt and delayed fluorescence),  $k_{\text{r}}^{\text{S}}$  and  $k_{\text{nr}}^{\text{S}}$  (rate constant of radiative and nonradiative decay from excited singlet state, to be specific, S<sub>1</sub>),  $k_{\text{nr}}^{\text{T}}$  (rate constant of nonradiative decay from excited triplet state, to be specific, T<sub>1</sub>),  $\Phi_{\text{ISC}}$  and  $\Phi_{\text{rISC}}$  (ISC and rISC efficiency),  $k_{\text{ISC}}$  and  $k_{\text{rISC}}$  (rate constant of ISC and rISC)

$$k_{\text{PF/DF}} = \frac{1}{\tau_{\text{PF/DF}}}$$

$$k_{\text{ISC}} = \frac{\Phi_{\text{DF}}}{\Phi_{\text{tot}}} * k_{\text{PF}}$$

$$k_{\text{RISC}} = \frac{k_{\text{PF}}}{k_{\text{ISC}}} * \frac{\Phi_{\text{DF}}}{\Phi_{\text{PF}}} * k_{\text{DF}}$$

$$k_{r,S} = \Phi_{\text{PF}} * k_{\text{PF}}$$

$$k_{nr,S} = (1 - \Phi_{\text{PF}} - \Phi_{\text{ISC}}) * k_{\text{PF}}$$

After experimental measurement and analysis of photophysical properties,  $\Phi_{\text{PF}}$ ,  $\Phi_{\text{DF}}$ ,  $\tau_{\text{PF}}$  and  $\tau_{\text{DF}}$  could be directly calculated. Other rate constants and efficiencies for designated photophysical process were calculated by the formula and confirmed whether the values fit the assumption for derivation of the equation.

### 3.2.5. OLED device fabrication and device test

OLED devices were fabricated on indium tin oxide (ITO)-patterned glass substrate using thermal evaporation under vacuum ( $P < 10^{-4}$  Pa). Detailed structure of the device and materials used were described at the discussion section. ITO-patterned glass substrates were rinsed by sonication with detergent-containing deionized water, acetone, and isopropyl alcohol, in the listed order. Sublimation-grade chemicals were used as purchased from commercial sources without further sublimation, unless specifically mentioned. Target materials were used as emitter and sublimed two times before the device fabrication. mCPCN, used for host material, was synthesized according to the previously reported method<sup>15</sup> and sublimed two

times before the device fabrication.

Each layer was deposited continuously following 20 minutes interval in order to prevent from intervening of particle formed during deposition and from increasing substrate temperature. Deposition rate was  $1.0 \text{ \AA s}^{-1}$  for organic layers,  $1.0 \text{ \AA s}^{-1}$  in total for the co-deposited organic layers,  $0.1 \text{ \AA s}^{-1}$  for LiF and  $2.0 \text{ \AA s}^{-1}$  for Al electrode, respectively. Customized aluminum masks for organic and inorganic material were applied during deposition to make the emitting layer of  $2 \text{ mm} \times 2 \text{ mm}$  square shape.

To evaluate performance of the OLED devices, the current–voltage–luminance (I–V–L) data were collected with Keithley 236 source-measure unit (Tektronix), Keithley 2000 multimeter unit (Tektronix) and a calibrated Si photodiode S5227-1010BQ (Hamamatsu). The luminance and the device efficiencies were calculated from the photocurrent measurement data obtained with the Si photodiode. The electroluminescence spectra were obtained by using a spectroradiometer CS-2000 (Konica Minolta).

### **3.3. Results and discussions**

#### **3.3.1. Materials design and synthesis**

Synthesis of target molecules started from commercially available 4-bromonaphthalic anhydride, and completed by two steps of reaction including condensation followed by Buchwald-Hartwig amination. Details of overall synthesis scheme, methods and structure analysis data were described in Supplementary Information. Whole synthetic routes were facile and the products were obtained with moderate yield.

#### **3.3.2. Theoretical calculation**

Before characterization of the target materials, optimized molecular geometry and electronic properties were calculated using Density Functional Theory (DFT) and Time-dependent DFT (TD-DFT). Molecular structure of all target materials in ground state exhibited twisted linkage of D-A, with dihedral angle of nearly 90° between naphthalimide and arylamine donor, which meets general design strategy of TADF molecule. Distribution of frontier molecular orbitals (FMOs) of target materials also showed that they were expected to exhibit TADF characteristics, where the highest occupied molecular orbitals (HOMOs) were localized at D and the lowest unoccupied molecular orbitals (LUMOs) were localized at A (naphthalimide), which could lead to reduced  $\Delta E_{ST}$  of molecules low enough to overcome by thermal excitation. Particularly, LUMO localized at naphthalimide didn't extended to

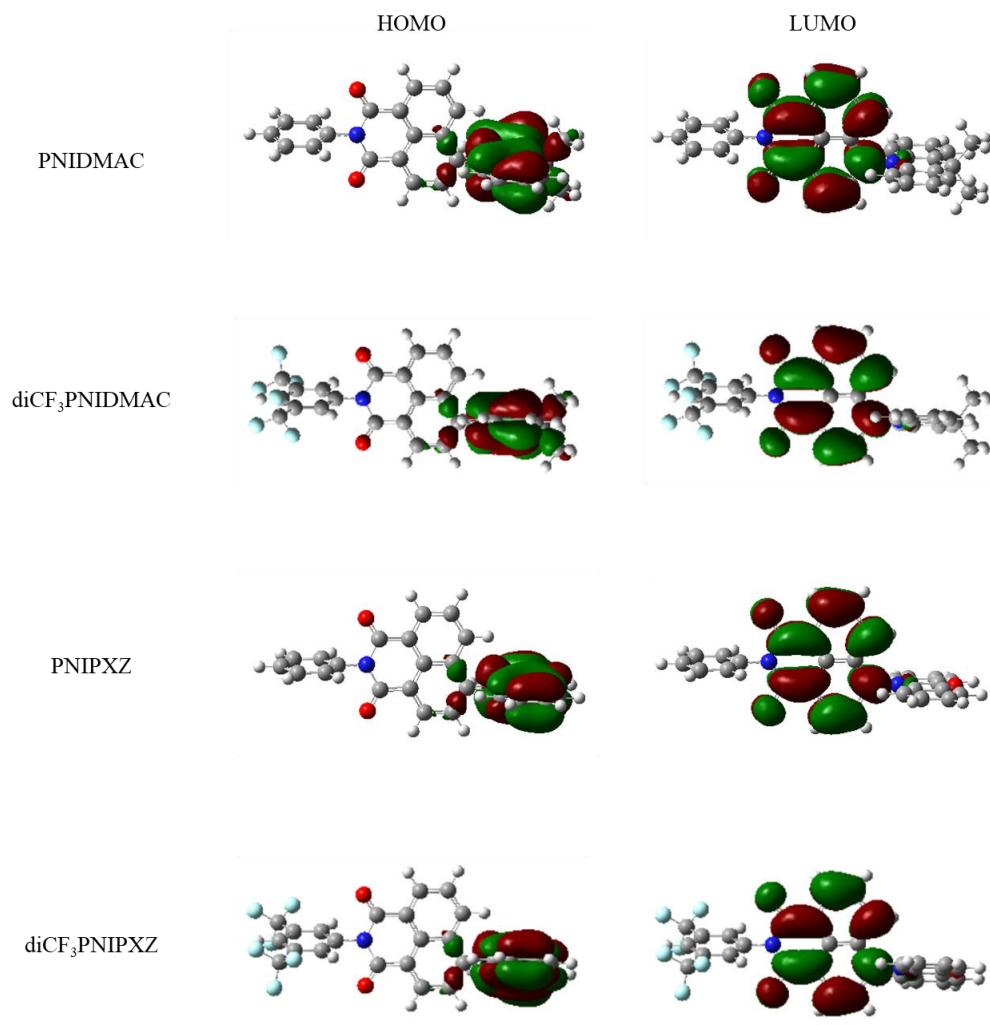


**Figure 3-2.** Optimized structure and distribution of HOMOs and LUMOs of the target materials from DFT calculation.

Emitter	HOMO	LUMO	S <sub>1</sub>	T <sub>1</sub>	ΔE <sub>ST</sub>
PNIDMAC	-5.18eV	-2.56eV	1.983eV	1.975eV	8meV
diCF3PNIDMA C	-5.31eV	-2.84eV	1.840eV	1.832eV	8meV
PNIPXZ	-4.95eV	-2.63eV	1.706eV	1.694eV	12meV
diCF3PNIPXZ	-5.09eV	-2.91eV	1.567eV	1.554eV	13meV

**Table 3-1.** Selective parameters of 1,8-naphthalimide-based TADF emitters from DFT calculation.

auxiliary group and phenyl ring attached to *N*- site of the imide, so that the auxiliary group would carry out delicate influence on the molecule. From the energy level calculation of FMOs, lowest excited singlet state energy ( $S_1$ ), and lowest excited triplet state energy ( $T_1$ ) of target materials, HOMO level depended on donor moiety and LUMO level depended on auxiliary functional group, which made less effect than HOMO level deviation. In terms of excited state energy, calculated  $\Delta E_{ST}$  and excited state values were as low as 10 meV and 2 eV in all target materials, respectively, which implies that they would be red-to-NIR TADF emitter.

### 3.3.3. Photophysical properties

From the calculation results, overall physical properties of the target materials were evaluated. First, FMO level were experimentally calculated from electrochemical and absorption measurement. HOMO level of the target materials, directly acquired from oxidation region of cyclicvoltammetry, varied up to 0.3 eV depending on the donor moiety, not on the introduction of auxiliary EWG. On the other hand, LUMO level, calculated from optical bandgap obtained from the onset wavelength of UV-Vis absorption spectra and HOMO level, was controlled with a consistent tendency by donor moiety and introduction of auxiliary EWG, but the difference was less than 0.1 eV. This result corresponded with the calculation result, which indicated little change of LUMO distribution and energy level with or without auxiliary EWG. From the result, it was confirmed that the proper modification of TADF emitter can be selected to adjust the photophysical properties to a desired level.

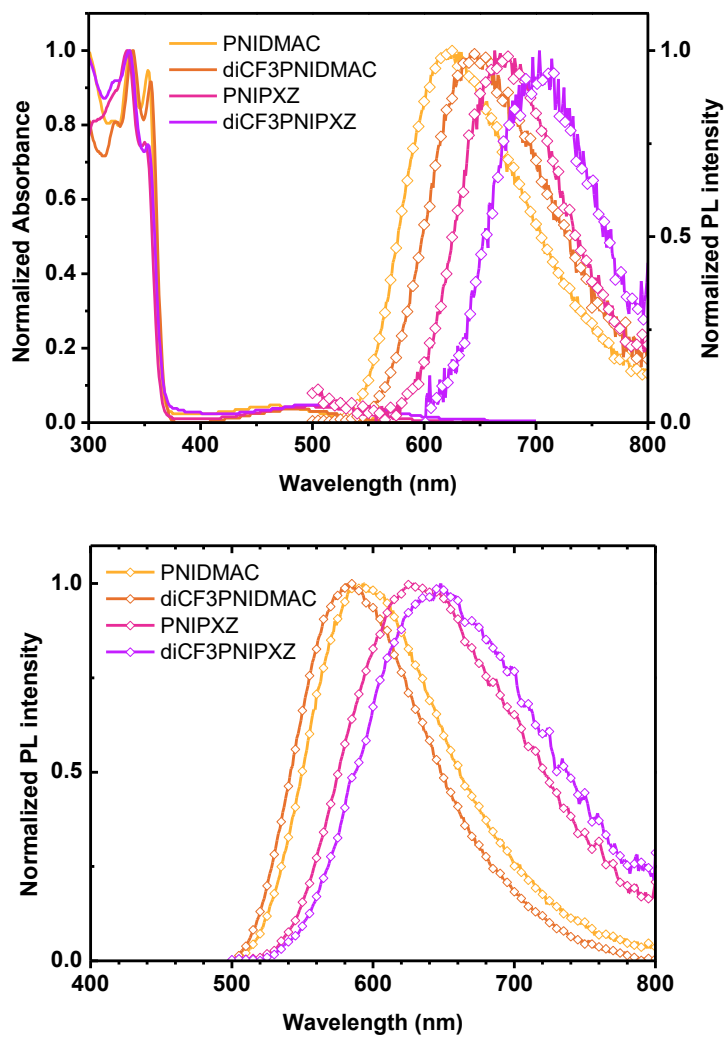


**Figure 3-3.** (upper) Absorption and emission spectra of target materials in toluene solution. (below) Emission spectra of target materials doped in mCPCN film.

Next, to ensure that the target materials exhibit proper photophysical characteristics of red emitter, UV-Vis absorption and Photoluminescence (PL) spectra were obtained in toluene solution and doped film with mCPCN as host. All the target materials showed strong and sharp absorption peaks near 335 and 350 nm, and a weak and broad structureless absorption peak around 500 nm in toluene solution. In emission spectra, all the target materials exhibited emission peak around 600 nm both in solution and doped film state. Moreover, this structureless emission range could be managed by intramolecular CT strength of the material, which indicates that the emission came from excited state with intramolecular CT character. PL quantum yield (PLQY) of the target materials was also acquired, which featured harsh decrease in PNIPXZ series which exhibited red-shifted emission range compared to PNIDMAC series, because of energy-gap law. In addition, fluorescence and phosphorescence of the target materials at 77K were measured to calculate  $S_1$  and  $T_1$  level from the onset wavelength of the spectra, respectively. From the spectra,  $\Delta E_{ST}$  of the target materials was calculated with the value less than 0.1eV, which means that rISC could occur effectively. Moreover, fluorescence and phosphorescence of the target materials in 77K exhibited structureless spectra based on intramolecular CT state rather than locally excited (LE) state of D or A, which indicates that the excited states of the target materials were sufficiently stable to function as a red emission.

Finally, to guarantee that the target materials have TADF characteristics, transient PL decay measurement at various temperature was carried out. Since the

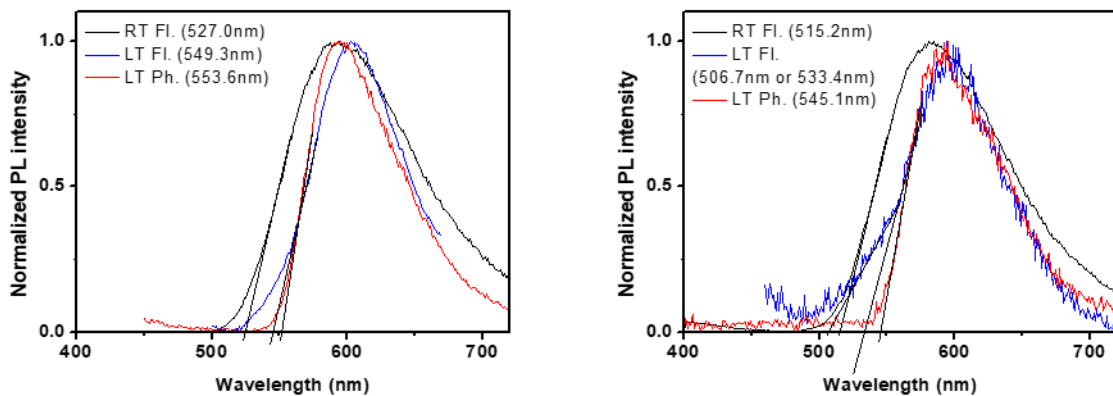


**Figure 3-4.** Low temperature PL spectra of the target materials doped in mCPCN film. (left) PNIDMAC (right) diCF<sub>3</sub>PNIDMAC.

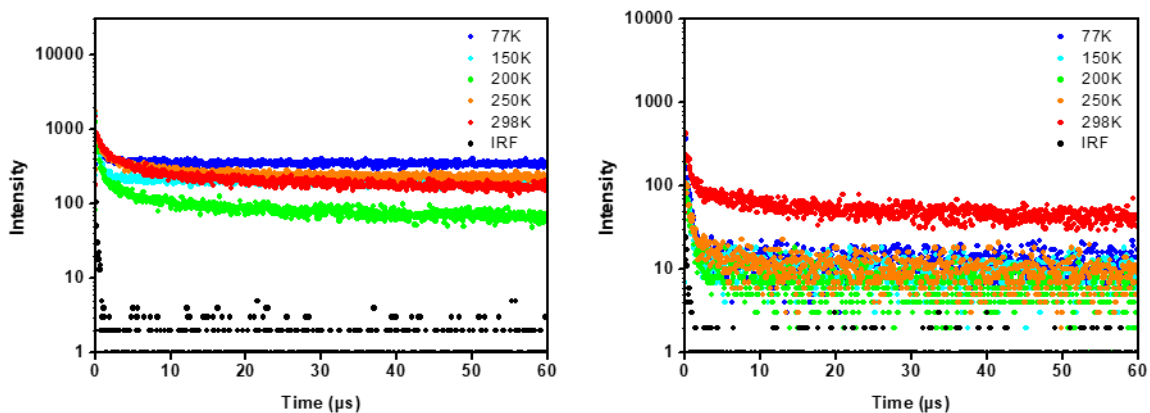


**Figure 3-5.** Time-resolved radiative decay profile of target materials doped in mCPCN film in various temperatures. (left) PNIDMAC (right) diCF<sub>3</sub>PNIDMAC.

PL decay profile of the doped film samples lasted for  $10^1 \mu\text{s}$  order, which is way longer time range than one in the conventional fluorescence, it was expected that all target materials could exhibit delayed fluorescence. Indeed, there was a PL decay component with lifetime from  $10^0 \mu\text{s}$  (PNIPXZ series) to  $10^1 \mu\text{s}$  (PNIDMAC series) order from the fitted data of PL decay profile, which meets the criteria of delayed fluorescence. Also, this delayed fluorescence didn't appear at low temperature, and the delayed fluorescence occurred faster and more active as the temperature rises. (Fig. S5 and Table S2) It could be concluded that TADF was observed in all the target materials since the results from the transient PL decay supported that rISC process was thermally activated.

#### 3.3.4. Rate constant study

From lifetime data of transient PL decay graph combined with the measured fluorescence performances, rate constant study was carried out following the formula in reference. Rate constants and quantum efficiencies of selected photophysical transitions are listed at Table S3. Contrary to the expectation that reduced  $\Delta E_{\text{ST}}$  in electron-withdrawing-group-attached compounds enhances TADF performance so that the portion of delayed fluorescence toward PLQY ( $f_{\text{DF}}$ ) increase, calculated  $f_{\text{DF}}$  also reduced as  $\Delta E_{\text{ST}}$  reduced. This could be elucidated from high rate constant of radiative decay in  $S_1$  state ( $k_{\text{rad},S}$ ), guiding photoexcited singlet exciton directly to prompt fluorescence rather than quantum-mechanically prohibited ISC in spite of small energy difference. However, at the same time, tendency of rate constant of

Material	Solution (10 <sup>-5</sup> M in toluene)		Doped film (1.5wt.% in mCPCN)		S <sub>1</sub> /T <sub>1</sub> /ΔE <sub>S-T</sub> (eV)	HOMO (eV)	LUMO (eV)	τ <sub>PF</sub> (ns)	τ <sub>DF</sub> (μs)
	λ <sub>abs</sub> (nm)	λ <sub>PL</sub> (nm)	λ <sub>PL</sub> (nm)	Φ <sub>PL</sub> (%)					
PNIDMAC	337,353,466	623	593	44.3	2.257/2.240/0.017	-5.39	-3.18	14.2	11.0
diCF <sub>3</sub> PNIDMAC	339,355,485	643	581	47.3	2.325/2.275/0.050	-5.43	-3.20	17.1	11.5
PNIPXZ	334,498	663	628	13.6	N/A	-5.13	-3.14	26.8	0.79
diCF <sub>3</sub> PNIPXZ	336,353,508	703	648	9.48	N/A	-5.15	-3.18	N/A	N/A

**Table 3-2.** Photophysical parameters of 1,8-naphthalimide-based TADF emitters from experiments.

rISC ( $k_{\text{rISC}}$ ) matched with tendency of  $\Delta E_{\text{ST}}$ ,  $k_{\text{rISC}}$  scoring high as  $4.12 \times 10^5 \text{ s}^{-1}$  in 4'-CNPXZOXD while low as  $2.37 \times 10^5 \text{ s}^{-1}$  in 4'-FPXZOXD. From the result, small  $\Delta E_{\text{ST}}$  value played an important role toward photophysical properties in two ways – increasing  $k_{\text{rad,S}}$  and  $k_{\text{rISC}}$ , which predicted that 4'-CNPXZOXD become a high-performance TADF emitter for OLED among the target compounds.

### 3.3.5. OLED device performance

To evaluate electric device performance of the target materials, OLED devices were fabricated as a stacked layers of ITO / HAT-CN (5 nm) / TAPC (30 nm) / mCP (10 nm) / 1.5wt.% emitter : mCPCN (20 nm) / TmPyPB (10 nm) / 3TPYMB (50 nm) / LiF (0.7 nm) / Al (100 nm). (ITO: indium tin oxide, served as an anode, HAT-CN: 1,4,5,8,9,11-hexaazatriphenylenehexacarbonitrile, served as a hole-injecting material, TAPC: 4,4'-cyclohexylidenebis[*N,N'*-bis(4-methylphenyl)benzenamine], served as a hole transporting material, mCP: 1,3-bis(9*H*-carbazol-9-yl)benzene, served as an exciton blocking material, mCPCN: 9-(3-(9*H*-carbazol-9-yl)phenyl)-9*H*-carbazole-3-carbonitrile, served as a host, TmPyPB: 1,3,5-tri(*m*-pyridin-3-ylphenyl)benzene, served as an exciton blocking material, 3TPYMB: tri[3-(3-pyridyl)mesityl]borane, served as an electron transporting material, LiF as an electron injecting material, Al as a cathode) All newly introduced target materials except the referential PNIDMAC had EL spectrum peak red-shifted than 600 nm, so that the suggested molecular design strategy was valid toward an efficient red-to-NIR TADF emitter. Besides, in the case of *N*- site substitution method of

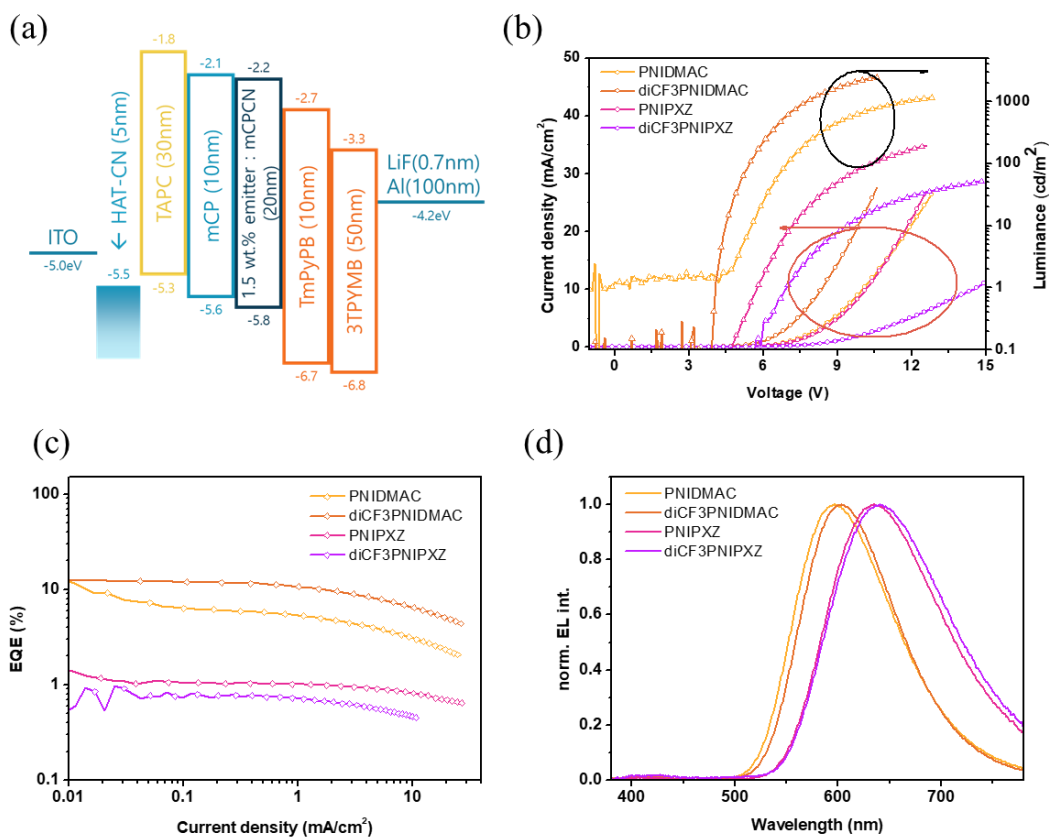


**Figure 3-6.** (a) Structure of OLED device. (b) J-V-L curve of the OLED device. (c) Electroluminescence spectrum of the OLED device. (d) External quantum efficiency graph of the OLED device.

naphthalimide, introducing EWG as an auxiliary group made finely tuned photophysical characteristics in the device without making much difference in formation of FMO. From this, OLED device with diCF3PNIDMAC as emitter recorded maximum EQE of 12.7% and its International Commission on Illumination (Commission internationale de l'éclairage, CIE) coordinate was (0.56,0.43), which showed deeper red emission than (0.54,0.44) in PNIDMAC-based device. Two emitters using phenoxazine as D (PNIPXZ and diCF3PNIPXZ) showed much lower maximum EQE about 1% in the device because of harshly suppressed PLQY, but their CIE coordinate (0.60,0.40) in the device implied that further optimization in the device structure and emitter would lead the emitters toward promising efficient red-to-NIR emitter.

Emitter	PNIDMAC	diCF3PNIDM AC	PNIPXZ	diCF3PNIPX Z
V <sub>on</sub> (V)	4.9	4.2	4.9	5.6
EQE (%)	11.5	12.7	1.39	0.973
EL peak (nm)	597	603	634	641
CIE	(0.54,0.44)	(0.56,0.43)	(0.61,0.38)	(0.59,0.37)

**Table 3-3.** Performance of OLED device using 1,8-naphthalimide-based TADF emitters.

### 3.4. Conclusions

In summary, new red-to-NIR TADF emitters were developed by both major and fine tuning strategy of photophysical characteristics. By comprehensive photophysical study, newly introduced materials had red-shifted emission, so they were able to raise the possibility of naphthalimide toward efficient red-to-NIR TADF emitter maintaining its superior emission property. The degree of tuning in photophysical properties of the emitter depended on the degree to which the tuning site contributes to the FMOs. Among the target materials, diCF<sub>3</sub>PNIDMAC exhibited EQE in the OLED device more than 12%. By adopting described material design strategy, understanding the contribution of possible substitution site of molecule to FMOs would help the TADF emitter to be tuned with controlled direction and amount in its photophysical properties.

### 3.5. References

1. M. Bixon, J. Jortner, J. Cortes, H. Heitele, M. E. Michel-Beyerle, *J. Phys. Chem.* **1994**, *98*, 7289-7299.
2. C.-T. Chen, *Chem. Mater.* **2004**, *16*, 4389-4400.
3. J. H. Kim, J. H. Yun, J. Y. Lee, *Adv. Opt. Mater.* **2018**, *6*, 1800255.
4. J. Chang, S. Zhang, N. Wang, Y. Sun, Y. Wei, R. Li, C. Yi, J. Wang, W. Huang, *J. Phys. Chem. Lett.* **2018**, *9*, 881-886.
5. B. S. Mashford, M. Stevenson, Z. Popovic, C. Hamilton, Z. Zhou, C. Breen, J. Steckel, V. Bulovic, M. Bawendi, S. Coe-Sullivan, P. T. Kazlas, *Nature Photonics* **2013**, *7*, 407-412.
6. B. Jiang, X. Ning, S. Gong, N. Jiang, C. Zhong, Z.-H. Lu, C. Yang, *J. Mater. Chem. C* **2017**, *5*, 10220-10224.
7. A. Endo, K. Sato, K. Yoshimura, T. Kai, A. Kawada, H. Miyazaki, C. Adachi, *Appl. Phys. Lett.* **2011**, *98*, 083302.
8. I. S. Park, S. Y. Lee, C. Adachi, T. Yasuda, *Adv. Funct. Mater.* **2016**, *26*, 1813-1821.
9. J. Li, T. Nakagawa, J. MacDonald, Q. Zhang, H. Nomura, H. Miyazaki, C. Adachi, *Adv. Mater.* **2013**, *25*, 3319-3323.
10. R. Furue, K. Matsuo, Y. Ashikari, H. Ooka, N. Amanokura, T. Yasuda, *Adv. Opt. Mater.* **2018**, *6*, 1701147.
11. J. H. Yun, J. Y. Lee, *Dyes and Pigments* **2017**, *144*, 212-217.
12. W. Zeng, H. Y. Lai, W. K. Lee, M. Jiao, Y. J. Shiu, C. Zhong, S. Gong, T. Zhou, G. Xie, M. Sarma, K. T. Wong, C. C. Wu, C. Yang, *Adv. Mater.* **2018**, *30*, 1704961.

13. X. Chen, C. Xu, T. Wang, C. Zhou, J. Du, Z. Wang, H. Xu, T. Xie, G. Bi, J. Jiang, X. Zhang, J. N. Demas, C. O. Trindle, Y. Luo, G. Zhang, *Angew. Chem. Int. Ed.* **2016**, *55*, 9872-9876.
14. Y. Tao, K. Yuan, T. Chen, P. Xu, H. Li, R. Chen, C. Zheng, L. Zhang, W. Huang, *Advanced Materials* **2014**, *26*, 7931-7958.
15. M.-S. Lin, S.-J. Yang, H.-W. Chang, Y.-H. Huang, Y.-T. Tsai, C.-C. Wu, S.-H. Chou, E. Mondal, K.-T. Wong, *Journal of Materials Chemistry* **2012**, *22*, 16114-16120.

## **Chapter 4.**

# **Chalcogen-introduced Multiresonance TADF Emitter for Narrow and Pure Blue Emission**

### **4.1. Research background**

Since thermally activated delayed fluorescence (TADF) was suggested, a great deal of donor-acceptor type TADF emitters and their application in OLED to enhance EQE more than 30%. However, intramolecular CT state, which is the essence of radiation from TADF emitter, has a critical disadvantage in its wide range of energy distribution, and features wide emission spectrum with full width at half maximum (FWHM) up to 100 nm and ambiguous color purity. This phenomenon is derived from activated molecular vibronic states that mainly comes from covalent single bond between donor and acceptor. To solve the problem in TADF, T. Hatakeyama introduced multiresonance (MR) model, with suppressed molecular motion by emitting covalent single bond and molecular orbitals split into atomic scale.<sup>1</sup> In the newly structured material, heteroatoms with different electronegativity affected phenyl rings right next to the heteroatom to separate localization of HOMO and LUMO. In addition, FWHM of emission got narrow by 20 nm, which is much smaller than in conventional D-A type TADF emitters,

because of suppressed molecular motion. From this discovery, efficient and pure colored emission using multiresonance model.<sup>2-5</sup>

However, process regarded to rISC in MR type TADF is not fully studied. MR type TADF materials have larger  $\Delta E_{ST}$  of about 0.2 eV than D-A type TADF emitters, which cannot be explained by simple spin flipping method. MR type TADF emitters still have delayed fluorescence with lifetime of microsecond scale or faster and exhibit light harvesting from excited triplet states clearly.

In this chapter, MR type TADF emitters with chalcogen<sup>6-12</sup> and boron atom as heteroatom for multiresonance are proposed. Within the series of target materials, role of excited triplet state beyond its low lying energy in rISC process could be described, with enhanced rISC process in its rate or fraction. From DOBNA-type emitter which is already reported, sulfur substitution into oxygen of the molecule and tetraphenylsilyl group attachment to the multiresonant core was executed to take quick rISC through heavy atom effect. Photophysical study revealed that SBS-Si, newly synthesized material in the chapter features pure blue emission with vigorous TADF characteristics.

## 4.2. Experimental method

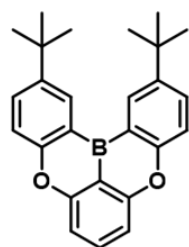
### 4.2.1. Materials and synthesis

Chemicals for synthesis of the target materials were used as purchased from commercial suppliers, without further purification. (4-(triphenylsilyl)phenyl)boronic acid was prepared as reported in the references. Thin layer chromatography (TLC) plate (silica gel 60 F254, Merck Co.) and silica gel 60 (particle size 0.063 – 0.200mm, Merck co.) were used to judge the reaction progress and for column chromatographic purification.

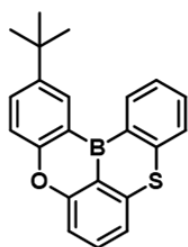
Chemical structures of the final target materials were assigned by analyzing nuclear magnetic resonance (NMR) spectra, mass spectra and elemental analysis (EA) data. <sup>1</sup>H-NMR data of the target materials were recorded on Avance-300 (Bruker), and <sup>13</sup>C-NMR data were recorded on Avance-500 (Bruker).

#### *Synthesis of 4,4'-((2-bromo-1,3-phenylene)bis(oxy))bis(tert-butylbenzene)*

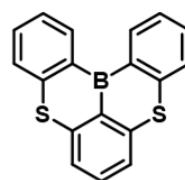
To a dehydrated round-bottomed flask connected with a reflux condenser, a mixture of 2-bromo-1,3-difluorobenzene (3.0 mL, 26.05 mmol), 4-*tert*-butylphenol (8.17 g, 54.41 mmol), potassium carbonate (12.9 g, 93.34 mmol) and anhydrous *N*-methyl-2-pyrrolidone (20 mL) was refluxed under inert atmosphere filled with Ar for 3 days. After the reaction finished, the mixture was cooled down to room temperature, poured into brine and extracted with dichloromethane. After the dichloromethane layer isolated from the mixture, dichloromethane solution was



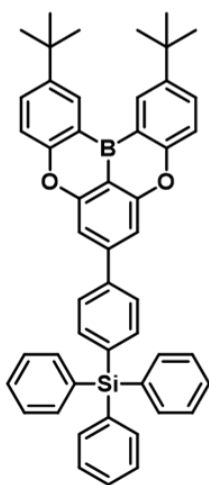
OBO core



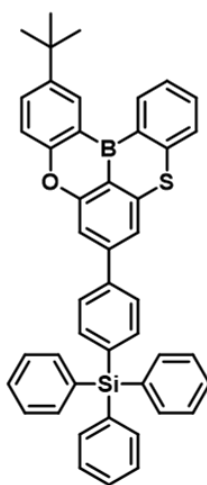
OBS core



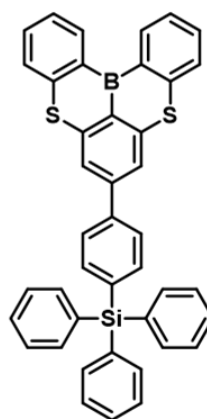
SBS core



OBO-Si



OBS-Si



SBS-Si

**Figure 4-1.** Chemical structure of the target materials.

extracted with brine 2 times more to remove residual *N*-methyl-2-pyrrolidone. The organic layer was dried with MgSO<sub>4</sub> and concentrated under reduced pressure. The residual thick oil was purified by column chromatography on silica gel using *n*-hexane to afford 4,4'-((2-bromo-1,3-phenylene)bis(oxy))bis(*tert*-butylbenzene) as white powder (6.02 g, yield: 51.3 %). <sup>1</sup>H NMR (300 MHz, CDCl<sub>3</sub>) δ: 7.37 (d, *J* = 8.5 Hz, 4H), 7.12 (t, *J* = 8.5 Hz, 1H), 6.96 (d, *J* = 10.0 Hz, 4H), 6.66 (d, *J* = 10.0 Hz, 2H), 1.32 (s, 18H).

*Synthesis of 2,12-di-tert-butyl-5,9-dioxo-13b-boranaphtho[3,2,1-de]anthracene (OBO core)*

To a dehydrated round-bottomed flask, 4,4'-((2-bromo-1,3-phenylene)bis(oxy))bis(*tert*-butylbenzene) (1.00 g, 2.21 mmol) was dissolved in *tert*-butylbenzene (10 mL) under atmosphere filled with Ar. The mixture was cooled down to -40 °C using cooling bath with acetonitrile and dry ice. *n*-butyllithium (2.5 M solution in hexane, 1.06 mL, 2.65 mmol) was slowly added to the mixture at -40 °C and stirred for 2 hours. After the lithiation finished, judging by TLC, boron tribromide (0.52 mL, 5.51 mmol) was slowly added to the mixture at -40 °C. Temperature of the mixture was slowly warm up to 60 °C and stirred 1 hour, followed by cooling down to 0 °C using cooling bath with ice water. Then, *N,N*-diisopropylethylamine (1.92 mL, 11.03 mmol) was added to the mixture and stirred for 30 minutes. The mixture was finally heated to 120 °C and stirred for 18 hours. After the reaction finished, the mixture was cooled down to room temperature and

quenched with 2 mL of water. The mixture was poured into dichloromethane and extracted with brine 3 times. The organic layer was dried with  $\text{MgSO}_4$  and concentrated under reduced pressure. The residual thick oil was purified by column chromatography on silica gel using dichloromethane / n-hexane (v:v 1:6) and washed with methanol to afford 2,12-di-*tert*-butyl-5,9-dioxa-13b-boranaphtho[3,2,1-*de*]anthracene (**OBO core**) as white powder (195 mg, yield: 23.1 %).  $^1\text{H}$  NMR (300 MHz,  $\text{CDCl}_3$ )  $\delta$ : 8.76 (d,  $J = 5.0$  Hz, 2H), 7.77 (m, 3H), 7.50 (d,  $J = 5.0$  Hz, 2H), 7.21-7.19 (d,  $J = 10.0$  Hz, 2H), 1.49 (s, 18H).  $^{13}\text{C}$  NMR (125 MHz,  $\text{CDCl}_3$ )  $\delta$ : 158.85, 157.75, 145.11, 134.53, 131.67, 130.44, 121.93, 118.19, 108.42, 34.76, 31.77.

*Synthesis of 4,4'-((2,5-dibromo-1,3-phenylene)bis(oxy))bis(tert-butylbenzene)*

Detailed synthetic method of 4,4'-((2-bromo-1,3-phenylene)bis(oxy))bis(*tert*-butylbenzene) was same to the synthetic method of 4,4'-((2-bromo-1,3-phenylene)bis(oxy))bis(*tert*-butylbenzene), as previously stated. With reacting chemicals including 2,5-dibromo-1,3-difluorobenzene (5.00 g, 3.68 mmol), 4-*tert*-butylphenol (1.16 g, 7.72 mmol), potassium carbonate (1.83 g, 13.24 mmol) and anhydrous *N*-methyl-2-pyrrolidone (20 mL), reaction was carried out for 3 days. Crude reaction mixture was purified to afford 4,4'-((2-bromo-1,3-phenylene)bis(oxy))bis(*tert*-butylbenzene) as white powder (6.34 g, yield: 64.8 %).  $^1\text{H}$  NMR (300 MHz,  $\text{CDCl}_3$ )  $\delta$ : 7.40 (d,  $J = 8.7$  Hz, 4H), 6.98 (d,  $J = 9.0$  Hz, 4H), 6.73 (s, 2H), 1.34 (s, 18H).

*Synthesis of 7-bromo-2,12-di-tert-butyl-5,9-dioxo-13b-boranaphtho[3,2,1-de]anthracene (OBO-Br)*

Detailed synthetic method of 4,4'-((2-bromo-1,3-phenylene)bis(oxy))bis(*tert*-butylbenzene) (**OBO-Br**) was same to the synthetic method of 2,12-di-*tert*-butyl-5,9-dioxo-13b-boranaphtho[3,2,1-*de*]anthracene (**OBO core**), as previously stated. With reacting chemicals including 4,4'-((2-bromo-1,3-phenylene)bis(oxy))bis(*tert*-butylbenzene) (2.00g, 3.76 mmol), *tert*-butylbenzene (20 mL), *n*-butyllithium (2.5 M solution in hexane, 1.80mL, 4.51 mmol), boron tribromide (0.9 mL, 9.50 mmol) and *N,N*-diisopropylethylamine (3.27 mL, 18.79 mmol), reaction was carried out for 18 hours after addition of *N,N*-diisopropylethylamine. Crude reaction mixture was purified to afford 7-bromo-2,12-di-*tert*-butyl-5,9-dioxo-13b-boranaphtho[3,2,1-*de*]anthracene (**OBO-Br**) as white powder (280 mg, yield: 16.2 %). <sup>1</sup>H NMR (300 MHz, CDCl<sub>3</sub>) δ: 8.74 (d, *J* = 2.4 Hz, 2H), 7.79 (dd, *J*<sub>1</sub> = 8.9 Hz, *J*<sub>2</sub> = 2.6 Hz, 2H), 7.49 (d, *J* = 9.0 Hz, 2H), 7.40-.37 (m, 2H), 1.48 (s, 18H).

*Synthesis of 4-(2,12-di-tert-butyl-5,9-dioxo-13b-boranaphtho[3,2,1-de]anthracen-7-yl)phenyl)triphenylsilane (OBO-Si)*

A mixture of 7-bromo-2,12-di-*tert*-butyl-5,9-dioxo-13b-boranaphtho[3,2,1-*de*]anthracene (**OBO-Br**) (200 mg, 0.43 mmol), (4-(triphenylsilyl)phenyl)boronic acid (181 mg, 0.48 mmol), tetrakis(triphenylphosphine)palladium(0) (25 mg, 0.02 mmol), K<sub>2</sub>CO<sub>3</sub> (2 M aqueous solution, 1.5 mL, 3.00 mmol) and toluene (5 mL) was stirred at 70 °C for 3 days under nitrogen atmosphere. After the reaction finished, the

mixture was cooled down to room temperature and extracted with brine and ethyl acetate. The organic layer was dried with MgSO<sub>4</sub> and concentrated under reduced pressure. The residual solid crude material was purified by column chromatography on silica gel using mixture solvent of dichloromethane / n-hexane (v:v 1:3) and washed with methanol to afford 4-(2,12-di-*tert*-butyl-5,9-dioxa-13b-boranaphtho [3,2,1-*de*]anthracen-7-yl)phenyl)triphenylsilane (**OBO-Si**) as white powder (112 mg, yield: 36.1 %) <sup>1</sup>H NMR (300 MHz, CDCl<sub>3</sub>) δ: 8.76 (d, *J* = 2.5 Hz, 2H), 7.79-7.77 (m, 4H), 7.71 (d, *J* = 8.5 Hz, 2H), 7.64-7.62 (m, 6H), 7.51 (d, *J* = 8.5 Hz, 2H), 7.48-7.41 (m, 5H), 7.40 (m, 6H), 1.49 (s, 18H). <sup>13</sup>C NMR (125 MHz, CDCl<sub>3</sub>) δ: 159.03, 158.09, 147.52, 145.22, 141.77, 137.21, 136.65, 134.60, 134.27, 131.66, 130.45, 129.92, 128.17, 127.20, 122.01, 118.19, 114.21, 107.25, 34.76, 31.77.

#### *Synthesis of 2-bromo-1-(4-(*tert*-butyl)phenoxy)-3-fluorobenzene*

Detailed synthetic method of 2-bromo-1-(4-(*tert*-butyl)phenoxy)-3-fluorobenzene was same to the synthetic method of 4,4'-((2-bromo-1,3-phenylene)bis(oxy))bis(*tert*-butylbenzene), as previously stated. With reacting chemicals including 2-bromo-1,3-difluorobenzene (3.0 mL, 26.05 mmol), 4-*tert*-butylphenol (3.89 g, 25.91 mmol), potassium carbonate (6.44 g, 46.63 mmol) and anhydrous *N*-methyl-2-pyrrolidone (10 mL), reaction was carried out for 3 days. Crude reaction mixture was purified to afford 2-bromo-1-(4-(*tert*-butyl)phenoxy)-3-fluorobenzene as thick transparent oil (4.11 g, yield: 49.1 %). <sup>1</sup>H NMR (300 MHz, CDCl<sub>3</sub>) δ: 7.37 (d, *J* = 9.0 Hz, 2H), 7.18 (q, *J* = 7.7 Hz, 1H), 6.94 (d, *J* = 9.0 Hz, 2H),

6.88 (t,  $J = 8.2$  Hz, 1H), 6.68 (d,  $J = 8.7$  Hz, 1H), 1.32 (s, 9H).

*Synthesis of (2-bromo-3-(4-(tert-butyl)phenoxy)phenyl)(phenyl)sulfane*

Detailed synthetic method of (2-bromo-3-(4-(tert-butyl)phenoxy)phenyl)(phenyl)sulfane was same to the synthetic method of 4,4'-((2-bromo-1,3-phenylene)bis(oxy))bis(tert-butylbenzene), as previously stated. With reacting chemicals including 2-bromo-1-(4-(tert-butyl)phenoxy)-3-fluorobenzene (1.00 g, 3.09 mmol), sodium thiophenolate (450 mg, 3.40 mmol) and anhydrous *N*-methyl-2-pyrrolidone (8 mL), reaction was carried out for 18 hours. Crude reaction mixture was purified to afford (2-bromo-3-(4-(tert-butyl)phenoxy)phenyl)(phenyl)sulfane as white powder (752 mg, yield: 58.8 %).  $^1\text{H}$  NMR (300 MHz,  $\text{CDCl}_3$ )  $\delta$ : 7.57-7.50 (m, 2H), 7.47-7.39 (m, 3H), 7.35 (d,  $J = 8.4$  Hz, 2H), 7.03 (t,  $J = 8.1$  Hz, 1H), 6.93 (d,  $J = 9.0$  Hz, 2H), 6.70 (dd,  $J_1 = 8.1$  Hz,  $J_2 = 1.5$  Hz, 2H), 6.56 (dd,  $J_1 = 6.3$  Hz,  $J_2 = 3.0$  Hz, 2H), 1.32 (s, 9H).

*Synthesis of 2-(tert-butyl)-5-oxa-9-thia-13b-boranaphtho[3,2,1-de]anthracene (OBS core)*

Detailed synthetic method of 2-(tert-butyl)-5-oxa-9-thia-13b-boranaphtho[3,2,1-de]anthracene (**OBS core**) was same to the synthetic method of 2,12-di-tert-butyl-5,9-dioxa-13b-boranaphtho[3,2,1-de]anthracene (**OBO core**), as previously stated. With reacting chemicals including (2-bromo-3-(4-(tert-butyl)phenoxy)phenyl)(phenyl)sulfane (752 mg, 1.82 mmol), tert-butylbenzene (8 mL), *n*-

butyllithium (2.5 M solution in hexane, 0.87 mL, 2.18 mmol), boron tribromide (0.43 mL, 4.55 mmol) and *N,N*-diisopropylethylamine (1.58 mL, 9.10 mmol), reaction was carried out for 18 hours after addition of *N,N*-diisopropylethylamine. Crude reaction mixture was purified to afford 2-(*tert*-butyl)-5-oxa-9-thia-13b-boranaphtho [3,2,1-*de*]anthracene (**OBS core**) as yellow powder (63.2 mg, yield: 10.2 %). <sup>1</sup>H NMR (300 MHz, CDCl<sub>3</sub>) δ: 8.70 (d, *J* = 8.1 Hz, 1H), 8.56 (d, *J* = 2.4 Hz, 1H), 7.78 (dd, *J*<sub>1</sub> = 8.7 Hz, *J*<sub>2</sub> = 2.7 Hz, 1H), 7.72 (d, *J* = 8.1 Hz, 1H), 7.66 (t, *J* = 7.9 Hz, 1H), 7.59 (td, *J*<sub>1</sub> = 7.7 Hz, *J*<sub>2</sub> = 1.5 Hz, 1H), 7.54-7.42 (m, 3H), 7.33 (d, *J* = 8.1 Hz, 1H), 1.48 (s, 18H). <sup>13</sup>C NMR (125 MHz, CDCl<sub>3</sub>) δ: 159.23, 158.46, 145.34, 144.26, 141.89, 137.50, 132.79, 131.47, 131.12, 126.30, 125.27, 117.82, 117.76, 112.39, 31.83.

*Synthesis of 2,5-dibromo-1-(4-(tert-butyl)phenoxy)-3-fluorobenzene*

Detailed synthetic method of 2,5-dibromo-1-(4-(*tert*-butyl)phenoxy)-3-fluorobenzene was same to the synthetic method of 4,4'-((2-bromo-1,3-phenylene)bis(oxy))bis(*tert*-butylbenzene), as previously stated. With reacting chemicals including 2,5-dibromo-1,3-difluorobenzene (1.00 g, 3.68 mmol), 4-*tert*-butylphenol (553 mg, 3.68 mmol), potassium carbonate (915 mg, 6.62 mmol) and anhydrous *N*-methyl-2-pyrrolidone (10 mL), reaction was carried out for 3 days. Crude reaction mixture was purified to afford 2,5-dibromo-1-(4-(*tert*-butyl)phenoxy)-3-fluorobenzene as white solid (1.04 g, yield: 70.4 %). <sup>1</sup>H NMR (300 MHz, CD<sub>2</sub>Cl<sub>2</sub>) δ: 7.41 (d, *J* = 8.7 Hz, 2H), 7.06 (dd, *J*<sub>1</sub> = 7.8 Hz, *J*<sub>2</sub> = 2.1 Hz, 1H), 6.94 (d, *J* = 8.7 Hz, 2H), 6.77 (t, *J* = 1.9 Hz, 1H), 1.32 (s, 9H).

*Synthesis of (2,5-dibromo-3-(4-(tert-butyl)phenoxy)phenyl)(phenyl)sulfane*

Detailed synthetic method of (2,5-dibromo-3-(4-(tert-butyl)phenoxy)phenyl)(phenyl)sulfane was same to the synthetic method of 4,4'-((2-bromo-1,3-phenylene)bis(oxy))bis(tert-butylbenzene), as previously stated. With reacting chemicals including 2,5-dibromo-1-(4-(tert-butyl)phenoxy)-3-fluorobenzene (1.00 g, 2.49 mmol), sodium thiophenolate (362 mg, 2.74 mmol) and anhydrous *N*-methyl-2-pyrrolidone (8 mL), reaction was carried out for 18 hours. Crude reaction mixture was purified to afford (2,5-dibromo-3-(4-(tert-butyl)phenoxy)phenyl)(phenyl)sulfane as white powder (895 mg, yield: 73.1 %). <sup>1</sup>H NMR (300 MHz, CDCl<sub>3</sub>) δ: 7.60-7.52 (m, 2H), 7.46 (t, *J* = 3.3 Hz, 3H), 7.38 (d, *J* = 8.7 Hz, 2H), 6.94 (d, *J* = 9.0 Hz, 2H), 6.76 (d, *J* = 2.4 Hz, 1H), 6.55 (d, *J* = 2.1 Hz, 1H), 1.33 (s, 9H).

*Synthesis of 7-bromo-2-(tert-butyl)-5-oxa-9-thia-13b-boranaphtho[3,2,1-de]anthracene (OBS-Br)*

Detailed synthetic method of 7-bromo-2-(tert-butyl)-5-oxa-9-thia-13b-boranaphtho[3,2,1-de]anthracene (**OBS-Br**) was same to the synthetic method of 2,12-di-tert-butyl-5,9-dioxa-13b-boranaphtho[3,2,1-de]anthracene (**OBO core**), as previously stated. With reacting chemicals including (2,5-dibromo-3-(4-(tert-butyl)phenoxy)phenyl)(phenyl)sulfane (895 mg, 1.82 mmol), *tert*-butylbenzene (10 mL), *n*-butyllithium (2.5 M solution in hexane, 0.87 mL, 2.18 mmol), boron tribromide (0.43 mL, 4.55 mmol) and *N,N*-diisopropylethylamine (1.58 mL, 9.09

mmol), reaction was carried out for 18 hours after addition of *N,N*-diisopropylethylamine. Crude reaction mixture was purified to afford 7-bromo-2-(*tert*-butyl)-5-oxa-9-thia-13b-boranaphtho[3,2,1-*de*]anthracene (**OBS-Br**) as yellow powder (199 mg, yield: 25.9%). <sup>1</sup>H NMR (300 MHz, CDCl<sub>3</sub>) δ: 8.70 (d, *J* = 7.8 Hz, 1H), 8.55 (d, *J* = 2.4 Hz, 1H), 7.79 (dd, *J*<sub>1</sub> = 8.9 Hz, *J*<sub>2</sub> = 2.6 Hz, 1H), 7.71 (d, *J* = 8.1 Hz, 1H), 7.65-7.56 (m, 2H), 7.55-7.45 (m, 3H), 1.46 (s, 9H).

*Synthesis of (4-(2-(tert-butyl)-5-oxa-9-thia-13b-boranaphtho[3,2,1-de]anthracen-7-yl)phenyl)triphenylsilane (OBS-Si)*

Detailed synthetic method of (4-(2-(*tert*-butyl)-5-oxa-9-thia-13b-boranaphtho[3,2,1-*de*]anthracen-7-yl)phenyl)triphenylsilane (**OBS-Si**) was same to the synthetic method of 4-(2,12-di-*tert*-butyl-5,9-dioxa-13b-boranaphtho [3,2,1-*de*]anthracen-7-yl)phenyl)triphenylsilane (**OBO-Si**), as previously stated. With reacting chemicals including 7-bromo-2-(*tert*-butyl)-5-oxa-9-thia-13b-boranaphtho[3,2,1-*de*]anthracene (**OBS-Br**) (92.5 mg, 0.22 mmol), (4-(triphenylsilyl)phenyl)boronic acid (167 mg, 0.44 mmol), tetrakis(triphenylphosphine)palladium(0) (12.7 mg, 0.01 mmol), K<sub>2</sub>CO<sub>3</sub> (2 M aqueous solution, 1 mL, 2.00 mmol) and toluene (3 mL), reaction was carried out for 3 days. Crude reaction mixture was purified to afford (4-(2-(*tert*-butyl)-5-oxa-9-thia-13b-boranaphtho[3,2,1-*de*]anthracen-7-yl)phenyl)triphenylsilane (**OBS-Si**) as yellow powder (55 mg, yield: 37.0 %). <sup>1</sup>H NMR (300 MHz, CDCl<sub>3</sub>) δ: 8.73 (d, *J* = 7.8 Hz, 1H), 8.58 (d, *J* = 2.4 Hz, 1H), 7.81-7.68 (m, 6H), 7.62 (dd, *J*<sub>1</sub> = 7.8 Hz, *J*<sub>2</sub> = 1.5 Hz, 6H), 7.59-7.48 (m, 4H), 7.48-7.34 (m, 10H),

1.47 (s, 9H).  $^{13}\text{C}$  NMR (125 MHz,  $\text{CDCl}_3$ )  $\delta$ : 159.61, 158.64, 145.58, 145.43, 144.32, 142.55, 141.17, 137.46, 137.25, 137.10, 136.63, 134.78, 134.21, 131.46, 131.13, 131.10, 129.93, 129.85, 129.79, 128.18, 128.12, 128.07, 127.14, 126.76, 126.34, 125.35, 117.78, 116.55, 110.99, 34.83, 31.84.

*Synthesis of (2-bromo-1,3-phenylene)bis(phenylsulfane)*

Detailed synthetic method of (2-bromo-1,3-phenylene)bis(phenylsulfane) was same to the synthetic method of 4,4'-((2-bromo-1,3-phenylene) bis(oxy))bis(*tert*-butylbenzene), as previously stated. With reacting chemicals including 2-bromo-1,3-difluorobenzene (3.0 mL, 26.05 mmol), sodium thiophenolate (7.53 g, 57.00 mmol) and anhydrous *N*-methyl-2-pyrrolidone (20 mL), reaction was carried out for 24 hours. Crude reaction mixture was purified to afford (2-bromo-1,3-phenylene) bis(phenylsulfane) as white powder (5.23 g, yield: 53.8 %).  $^1\text{H}$  NMR (300 MHz,  $\text{CDCl}_3$ )  $\delta$ : 7.53-7.50 (m, 2H), 7.49 (d,  $J$  = 2.1 Hz, 2H), 7.43-7.40 (m, 3H), 7.39 (d,  $J$  = 2.1 Hz, 3H), 6.93 (t,  $J$  = 7.8 Hz, 1H), 6.60 (d,  $J$  = 7.8 Hz, 2H).

*Synthesis of 5,9-dithia-13b-boranaphtho[3,2,1-*de*]anthracene (SBS core)*

Detailed synthetic method of 5,9-dithia-13b-boranaphtho[3,2,1-*de*]anthracene (SBS core) was same to the synthetic method of 2,12-di-*tert*-butyl-5,9-dioxa-13b-boranaphtho[3,2,1-*de*]anthracene (OBO core), as previously stated. With reacting chemicals including (2-bromo-1,3-phenylene) bis(phenylsulfane) (1.00 g, 2.68 mmol), *tert*-butylbenzene (10 mL), *n*-butyllithium (2.5 M solution in hexane, 1.3 mL,

3.25 mmol), boron tribromide (0.63 mL, 6.70 mmol) and *N,N*-diisopropylethylamine (2.33 mL, 13.39 mmol), reaction was carried out for 18 hours after addition of *N,N*-diisopropylethylamine. Crude reaction mixture was purified to afford 5,9-dithia-13b-boranaphtho[3,2,1-*de*]anthracene (**SBS core**) as yellow powder (156 mg, yield: 19.3 %). <sup>1</sup>H NMR (300 MHz, CDCl<sub>3</sub>) δ: 8.31 (d, *J* = 7.5 Hz, 2H), 7.73 (d, *J* = 7.8 Hz, 2H), 7.61 (t, *J* = 1.8 Hz, 1H), 7.60-7.54 (m, 3H), 7.51 (dd, *J*<sub>1</sub> = 8.7 Hz, *J*<sub>2</sub> = 6.6 Hz, 1H), 7.44 (t, *J* = 7.4 Hz, 2H). <sup>13</sup>C NMR (125 MHz, CDCl<sub>3</sub>) δ: 143.62, 143.53, 138.78, 131.03, 130.23, 125.70, 125.20, 121.50.

*Synthesis of (2,5-dibromo-1,3-phenylene)bis(phenylsulfane)*

Detailed synthetic method of (2,5-dibromo-1,3-phenylene)bis(phenylsulfane) was same to the synthetic method of 4,4'-((2-bromo-1,3-phenylene)bis(oxy))bis(*tert*-butylbenzene), as previously stated. With reacting chemicals including 2,5-dibromo-1,3-difluorobenzene (1.00 g, 3.68 mmol), sodium thiophenolate (1.07 g, 8.09 mmol) and anhydrous *N*-methyl-2-pyrrolidone (5 mL), reaction was carried out for 24 hours. Crude reaction mixture was purified to afford (2,5-dibromo-1,3-phenylene)bis(phenylsulfane) as white powder (741 mg, yield: 44.6 %). <sup>1</sup>H NMR (300 MHz, CDCl<sub>3</sub>) δ: 7.55-7.48 (m, 4H), 7.45 (t, *J* = 3.3 Hz, 6H), 6.59 (s, 2H).

*Synthesis of 7-bromo-5,9-dithia-13b-boranaphtho[3,2,1-*de*]anthracene (SBS-Br)*

Detailed synthetic method of 7-bromo-5,9-dithia-13b-boranaphtho[3,2,1-

*de*]anthracene (**SBS-Br**) was same to the synthetic method of 2,12-di-*tert*-butyl-5,9-dioxa-13b-boranaphtho[3,2,1-*de*]anthracene (**OBO core**), as previously stated. With reacting chemicals including (2,5-dibromo-1,3-phenylene)bis(phenylsulfane) (741 mg, 1.64 mmol), *tert*-butylbenzene (5 mL), *n*-butyllithium (2.5 M solution in hexane, 0.79 mL, 1.97 mmol), boron tribromide (0.39 mL, 4.10 mmol) and *N,N*-diisopropylethylamine (1.43 mL, 8.19 mmol), reaction was carried out for 18 hours after addition of *N,N*-diisopropylethylamine. Crude reaction mixture was purified to afford 7-bromo-5,9-dithia-13b-boranaphtho[3,2,1-*de*]anthracene (**SBS-Br**) as yellow powder (132 mg, yield: 22.4 %). <sup>1</sup>H NMR (300 MHz, CD<sub>2</sub>Cl<sub>2</sub>) δ: 8.30 (d, *J* = 7.5 Hz, 2H), 7.76-7.69 (m, 4H), 7.60 (td, *J*<sub>1</sub> = 7.5 Hz, *J*<sub>2</sub> = 1.5 Hz, 2H), 7.46 (td, *J*<sub>1</sub> = 7.5 Hz, *J*<sub>2</sub> = 1.0 Hz, 2H).

*Synthesis of (4-(5,9-dithia-13b-boranaphtho[3,2,1-*de*]anthracen-7-yl)phenyl)triphenylsilane (**SBS-Si**)*

Detailed synthetic method of (4-(5,9-dithia-13b-boranaphtho[3,2,1-*de*]anthracen-7-yl)phenyl)triphenylsilane (**SBS-Si**) was same to the synthetic method of 4-(2,12-di-*tert*-butyl-5,9-dioxa-13b-boranaphtho[3,2,1-*de*]anthracen-7-yl)phenyl)triphenylsilane (**OBO-Si**), as previously stated. With reacting chemicals including 7-bromo-5,9-dithia-13b-boranaphtho[3,2,1-*de*]anthracene (**SBS-Br**) (100 mg, 0.26 mmol), (4-(triphenylsilyl)phenyl)boronic acid (100 mg, 0.26 mmol), tetrakis(triphenylphosphine)palladium(0) (15.2 mg, 0.01 mmol), K<sub>2</sub>CO<sub>3</sub> (2 M aqueous solution, 1 mL, 2.00 mmol) and toluene (3 mL), reaction was carried out for 3 days.

Crude reaction mixture was purified to afford (4-(5,9-dithia-13b-boranaphtho[3,2,1-*de*]anthracen-7-yl)phenyl)triphenylsilane (**SBS-Si**) as yellow powder (38.3 mg, yield: 22.9 %).  $^1\text{H}$  NMR (300 MHz,  $\text{CDCl}_3$ )  $\delta$ : 8.34 (d,  $J = 6.6$  Hz, 2H), 7.83 (s, 1H), 7.77-7.69 (m, 4H), 7.65-7.53 (m, 10H), 7.50-7.34 (m, 12H).  $^{13}\text{C}$  NMR (125 MHz,  $\text{CDCl}_3$ )  $\delta$ : 207.20, 142.09, 138.74, 137.28, 137.10, 136.59, 134.35, 134.05, 133.52, 133.38, 133.05, 131.05, 130.97, 130.70, 129.95, 129.89, 128.18, 127.11, 126.87, 126.83, 126.76, 125.74, 125.28, 121.42, 120.14, 31.15.

### 3.2.2. Quantum chemical calculation

All quantum chemical calculations were carried out using the Gaussian 09 quantum chemical package. Geometry optimization in the ground state was performed using density functional theory (DFT) method with B3LYP functional / 6-31G(d,p) basis set. Energy levels of the ground state and some excited state with singlet or triplet multiplicity were calculated using time-dependent DFT (TD-DFT) method with B3LYP functional / 6-31G(d,p) basis set.

### 3.2.3. Photophysical and electrochemical characterization

Solution samples for cyclic voltammetry (CV) measurement were prepared as concentration of  $2 \times 10^{-3}$  M in methylene chloride, with 0.1 M TBAHFP as the supporting electrolyte. Solution samples for other photophysical characterizations were prepared as concentrations of  $10^{-5}$  M in toluene. Film samples were fabricated on quartz substrate with spin coating method, using 2 wt.% of emitter material and

98 wt.% of host material. Concentration of the solution for spin coating was 0.25 g mL<sup>-1</sup> in total. Quartz substrates were rinsed by sonication with detergent-containing deionized water, acetone, and isopropyl alcohol, in the listed order.

CV was performed on 273A (Princeton Applied Research) using a three-electrode solution container cell. Three electrodes include an Ag wire in 0.01 M AgNO<sub>3</sub> solution as a reference electrode, a carbon disc as a working electrode, and a Pt wire as a counter electrode. The redox potential of the reference electrode was calibrated using ferrocene/ferrocenium (Fc/Fc<sup>+</sup>) as an internal standard. For steady-state photophysical studies, UV-1650PC (Shimadzu) for UV-Vis absorption spectra, QuantaMaster 40 (Photon Technology International) for room temperature photoluminescence spectra, FP-6500 spectrofluorometer (Jasco) for low temperature photoluminescence spectra were used, respectively. In order to remove background data, quartz cuvette filled with toluene, which was the solvent for the solution samples, or quartz substrate was used for the steady-state photophysical studies. Time-dependent photoluminescence decay profiles were observed by FluoTime 200 (PicoQuant) and analyzed by time-correlated single photon counting technique.

## 4.3. Results and discussions

### 4.3.1. Molecular design and characterization

To inspect the effect of heavy atom effect toward MR TADF, two kinds of heavy atom including sulfur (S) and silicon (Si) were substituted for oxygen (O) or introduced to the existing MR TADF core part, respectively. From the referential compound OBO core, which was previously reported, two oxygen atoms were sequentially substituted into S atom to derive OBS core and SBS core. Sulfur atom is in the same chalcogen chemical family as oxygen, which would not dramatically change the overall chemical structure or characteristics of the molecule, but is heavier than oxygen so that the atom could induce heavy atom effect and increase spin-orbit coupling enough. Tetraphenylsilyl group (Ph<sub>4</sub>Si) was additionally introduced to the *para* site of phenyl ring directly and simultaneously connected to chalcogens and boron to derive OBO-Si, OBS-Si and SBS-Si. Therefore, six target materials were designed for this chapter.

Synthesis of the target materials included nucleophilic aromatic substitution of aryl fluoride as C-O / C-S coupling, ring closing including boron atom, and Suzuki coupling of aryl bromide and (4-(triphenylsilyl)phenyl)boronic acid. Reactions were executed with generous yield, except for ring closing step, which was challenged by unexpected deactivation of lithiated intermediate and poor reactivity between intermediate and *N,N*-diisopropylethylamine. Detailed synthetic procedure was described in the experimental method (**Section 4.2**). Chemical structure of newly

synthesized compounds were assigned with NMR spectra. Especially for the ring closing step, there was special signal peak with chemical shift up to 9 ppm in  $^1\text{H}$  NMR spectra. The peak was originated from the hydrogen nearest to boron atom of the ring-closed MR TADF compound, which was scarcely found in normal aromatic organic compounds.

#### **4.3.2. Theoretical calculation**

Optimized molecular geometry and electronic properties were calculated using DFT calculation., while tendency and essence of excited states were estimated through TD-DFT calculation. Molecular structure of multiresonant core part of all target materials in the ground state was nearly planar, including the phenyl ring connected to both of the chalcogen atoms and boron concurrently (“main plane”) and the phenyl ring connected to only one of two chalcogen atoms and boron (“side plane”). To be specific, sulfur atom in the molecule increased steric hindrance because of enlarged atom radius than oxygen atom, which led the distortion of two side planes. Dihedral angle between two side planes was  $9.6^\circ$  in OBO core and got wider up to  $28.8^\circ$  in OBS core and  $42.5^\circ$  in SBS core. On the other hand, introduction of tetraphenylsilyl group did not changed the atomic configuration of MR core part, reducing the dihedral angle no more than  $2^\circ$  compared to the MR core material without tetraphenylsilyl group. On behalf of trivial effect on the MR core, tetraphenylsilyl group itself had specific geometry, with one coplanar phenyl ring directly connected to the MR core and almost vertically lying phenyl rings alongside

Si atom.

HOMOs and LUMOs of target materials were also examined from DFT calculation. Distribution of the HOMO was focused on carbon atoms at *meta* position based on carbon atom bonded to boron atom, while the LUMO was localized to carbon atoms at *ortho* and *para* position and boron atom, giving that HOMO and LUMO were spatially separated as design strategy of multiresonance. Energy level of HOMO was calculated between -5.4 eV and -5.5 eV through all target materials, regardless of sulfur substitution and introduction of tetraphenylsilyl group. However, LUMO energy become deeper when oxygen atom changed to sulfur atom or tetraphenylsilyl group attached, from -1.59 eV in OBO core to -1.91 eV in SBS core and -1.97 eV in SBS-Si, which means bandgap energy between HOMO and LUMO got reduced throughout the chemical change. This result stems from contribution of sulfur substitution and tetraphenylsilyl group toward molecular orbitals, which did not change the fundamental structure of HOMO and LUMO of the target material, but affected LUMO a little by extend the conjugation length.

From the energetic point of view, excited singlet and triplet states were investigated to determine whether the target materials could have TADF properties. All target materials exhibited  $S_1$  level 0.45 eV to 0.5 eV higher than  $T_1$  level, which was immoderate for conventional TADF emitter but general for MR type TADF emitter. Instead of low-lying  $T_1$ ,  $T_2$  was energetically near to  $S_1$  state with difference less than 0.1 eV in most materials, which could take the key role in rISC process. In accordance with bandgap energy, energy level of the same excited states was

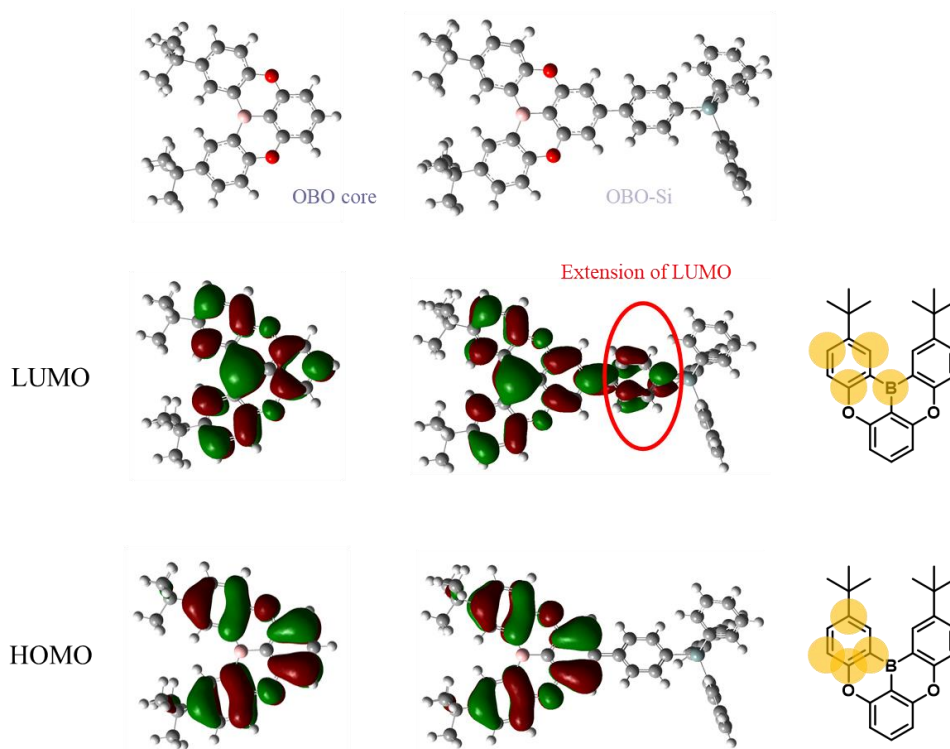


**Figure 4-2.** Optimized structure and distribution of HOMOs and LUMOs of OBO core and OBO-Si from DFT calculation.

Material	HOMO (eV)	LUMO (eV)	$S_1$ (eV)	$T_1$ (eV)	$\Delta E_{S1-T1}$ (eV)	$T_2$ (eV)	$\Delta E_{S1-T2}$ (eV)	Dihedral angle (deg.)
OBO core	-5.49	-1.59	3.3710	2.8492	0.5218	3.3113	0.0597	9.6
OBS core	-5.42	-1.74	3.1609	2.6529	0.5080	3.2349	-0.0740	28.8
SBS core	-5.45	-1.91	3.0054	2.5461	0.4593	3.0169	-0.0115	42.5
OBO-Si	-5.50	-1.70	3.2991	2.7822	0.5169	3.1109	0.1882	7.6
OBS-Si	-5.45	-1.84	3.1023	2.6107	0.4916	3.0323	0.0700	28.4
SBS-Si	-5.44	-1.97	2.9540	2.5001	0.4539	2.9141	0.0399	42.2

**Table 4-1.** Selective parameters of MR type TADF emitters from DFT calculation.

decreased as the sulfur replaced oxygen or tetraphenylsilyl group attached, but with different amount of change for each excited states. Deviation of excited triplet levels were milder than the  $S_1$  level, giving reduced  $\Delta E_{ST}$  of target material from 0.52 eV in OBO core to 0.46 eV in SBS core and 0.45 eV in SBS-Si. (SOCME result should be attached, if I want to)

#### **4.3.3. Photophysical properties**

From the calculation results, overall physical properties of the target materials were evaluated. UV-Vis absorption and PL emission spectra were firstly obtained to check whether the target materials work well as fluorescent emitter. All target materials exhibited narrow absorption and emission band in toluene solution, which is characteristics of MR type TADF emitter with small chance of vibration mode of chemical bond. Therefore, reduced Stokes shift about 20 nm were found in most of samples compared to conventional D-A type TADF emitters, which value is expanded up to 100 nm or more. Wavelength range of absorption and emission was blue-shifted as sulfur atom altered oxygen atom, which is already known properties from previous reports. First equivalent of atomic substitution in OBS core and OBS-Si induced bathochromic shift of about 30 nm in absorption and 40 nm in emission from OBO core and OBO-Si, but the bathochromic shift effect was reduced down to about 20 nm in absorption and emission for the second equivalent atomic substitution in SBS core and SBS-Si. Meanwhile, tetraphenylsilyl group did not affected wavelength range of the target material, with 6 to 8 nm bathochromic shift in

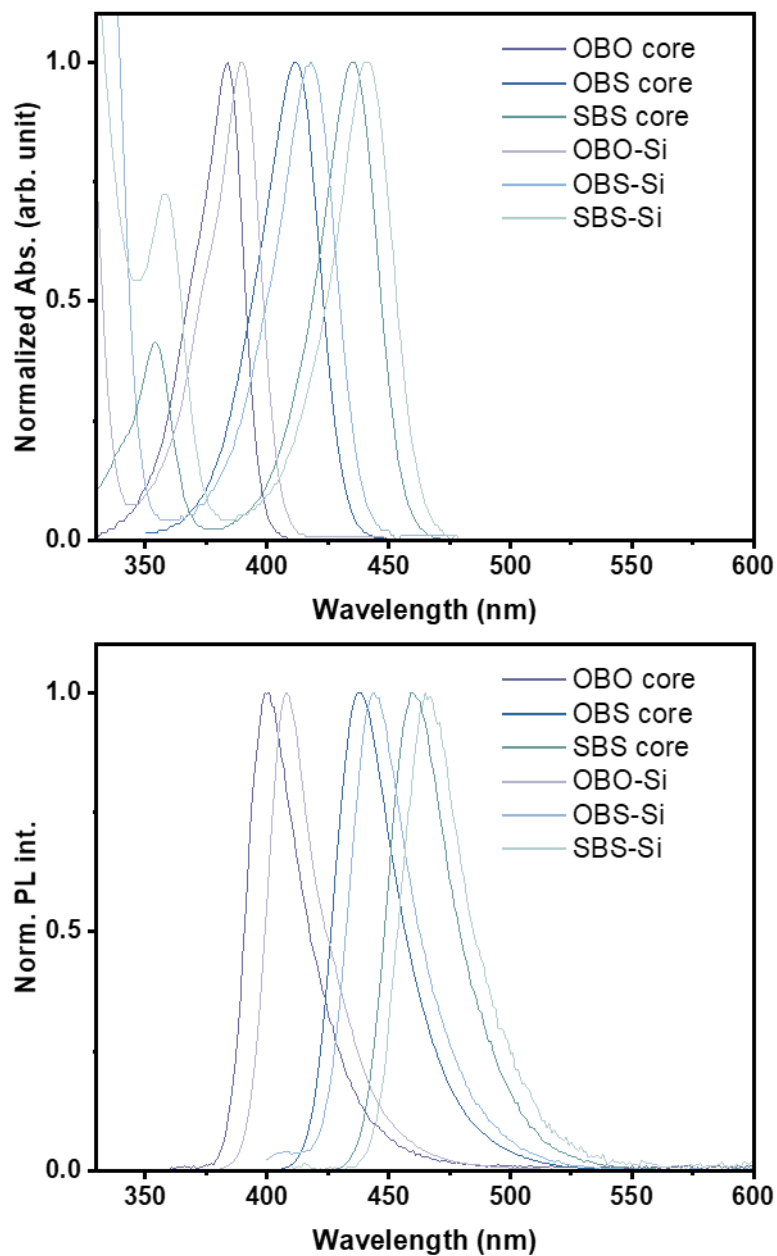


**Figure 4-3.** (upper) Absorption and (lower) emission spectra of target materials in toluene solution.

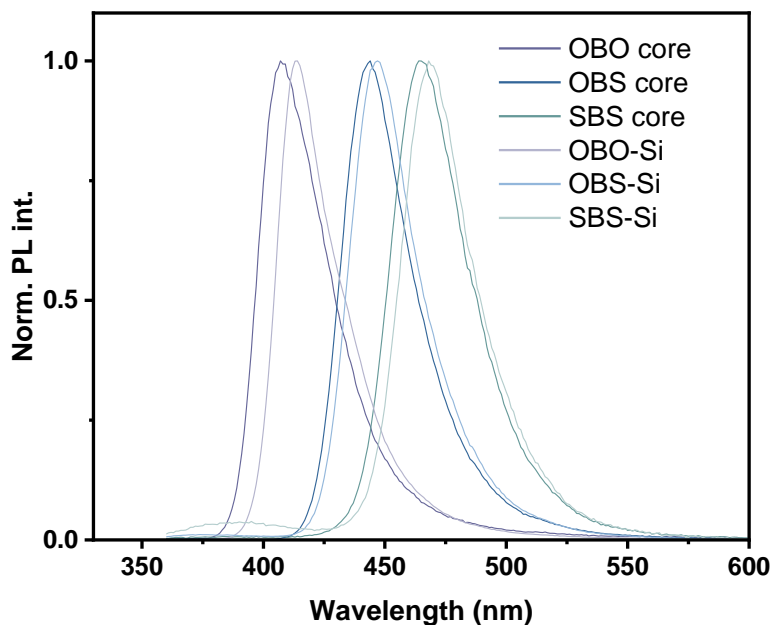


**Figure 4-4.** Emission spectra of target materials doped in DPEPO film.

Material	Solution ( $10^{-5}$ M in toluene)			Doped film (2wt.% in DPEPO)			$S_1/T_1/\Delta E_{S,T}$ (eV)	HOMO (eV)	$E_{g,opt}$ (eV)	LUMO (eV)	$\tau_{PF}$ (ns)	$\tau_{DF}$ ( $\mu$ s)
	$\lambda_{abs}$ (nm)	$\lambda_{PL}$ (nm)	FWHM (nm)	$\lambda_{PL}$ (nm)	FWHM (nm)	$\Phi_{PL}$ (%)						
OBO core	384	400	27	407	33	55.1	3.246/2.997/0.249	-0.00	3.120	-0.00	13.6	0.353
OBS core	412	438	31	444	34	39.0	3.045/2.804/0.241		2.874		47.9	0.380,56.1
SBS core	354,435	460	31	464	38	29.8	2.886/2.637/0.249		2.721		-	0.426,53.5
OBO-Si	390	408	25	414	30	55.1	3.206/2.951/0.255		3.056		13.7	0.298
OBS-Si	418	444	30	447	33	33.0	3.012/2.759/0.254		2.828		43.2	66.2
SBS-Si	358,441	466	31	468	35	23.9	2.804/2.606/0.198		2.685		-	0.445,62.2

**Table 4-2.** Photophysical parameters of 1,3,4-oxadiazole-based TADF emitters from experiments.

absorption and emission when attached to the multiresonant core.

It was noteworthy that SBS core and SBS-Si had blue emission with emission maximum at 460 nm and 466 nm, which overcame the inadequacy of UV-emitting OBO core as emitters for visible light display device. Moreover, additional absorption band at higher energy level was found in materials containing sulfur, and the relative absorption of the higher energy level was intensified as tetraphenylsilyl group introduced. From the result of absorption spectra, one could estimate that higher energy state of  $S_n$  and  $T_n$  probably take part in intersystem crossing by spin-orbit coupling from sulfur and silicon atom, which would make target materials utilizing TADF rigorously. PL emission of film samples with DPEPO as host materials were also evaluated. Wavelength range of emission did not displaced much in film samples from the data of solution samples. Common in solution and film samples, narrower emission was exhibited when tetraphenylsilyl group introduced, with reduced FWHM value from 38 nm in SBS core in DPEPO film to 35 nm in SBS-Si in same condition. From this, it could be supposed that tetraphenylsilyl group bears vibrational perturbation to molecular transformation of multiresonant core, while not affecting much to the emission wavelength as seen in the theoretical calculation section.

Fluorescence and phosphorescence spectra in 77K were measured to calculate  $S_1$  and  $T_1$  levels. From onset wavelength of non-delayed and delayed measurement of photoluminescence spectra, energy level of  $S_1$  state was calculated between 3.25 eV and 2.80 eV, and  $T_1$  state between 3.00 eV and 2.61 eV. Energy level of the excited

states decreased up to 0.2 eV as sulfur gradually substituted an oxygen, but tetraphenylsilyl group changed excited energy levels subtly. Therefore,  $\Delta E_{ST}$  was recorded as about 0.25 eV, and maintained its value within most of the target materials. To be surprise, there was specific form of graph of fluorescence in low temperature for target materials containing sulfur atom. Their low temperature fluorescence data showed not only emission from  $S_1$  state but also emission from  $T_1$  state, which means phosphorescence could occur within extremely short data acquisition time and thus the emitters could utilize ultrafast rISC process.

Delayed fluorescence was directly observed via transient PL decay profile. Contrary to the expectation, there was no delayed fluorescence observed in OBO core and OBO-Si. Even supposed that the lifetime of delayed fluorescence was way longer than the observation time range, proportion of the delayed fluorescence was such a trivial amount that could be neglected. However, rest of target materials showed delayed fluorescence, with lifetime of  $10^2$  ns or  $10^1$   $\mu$ s order. From the result, it could be found that two molecular design strategies executed enhance of delayed fluorescence in different way. Substitution by sulfur atom reduced lifetime of  $10^1$   $\mu$ s-ordered delayed fluorescence, while tetraphenylsilyl group increased proportion of delayed fluorescence without reducing lifetime.

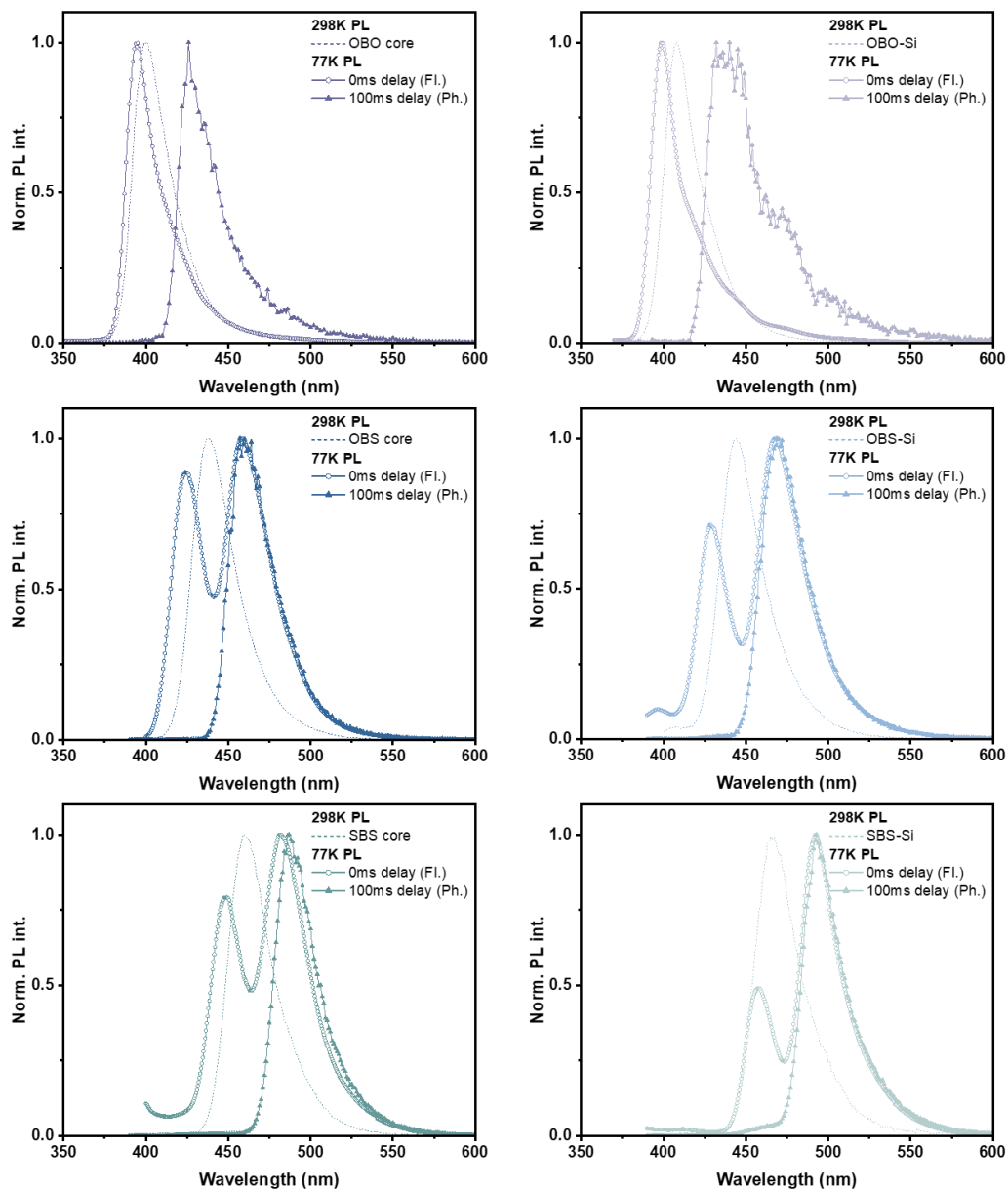


**Figure 4-5.** Low temperature PL spectra of the target materials in toluene solution.

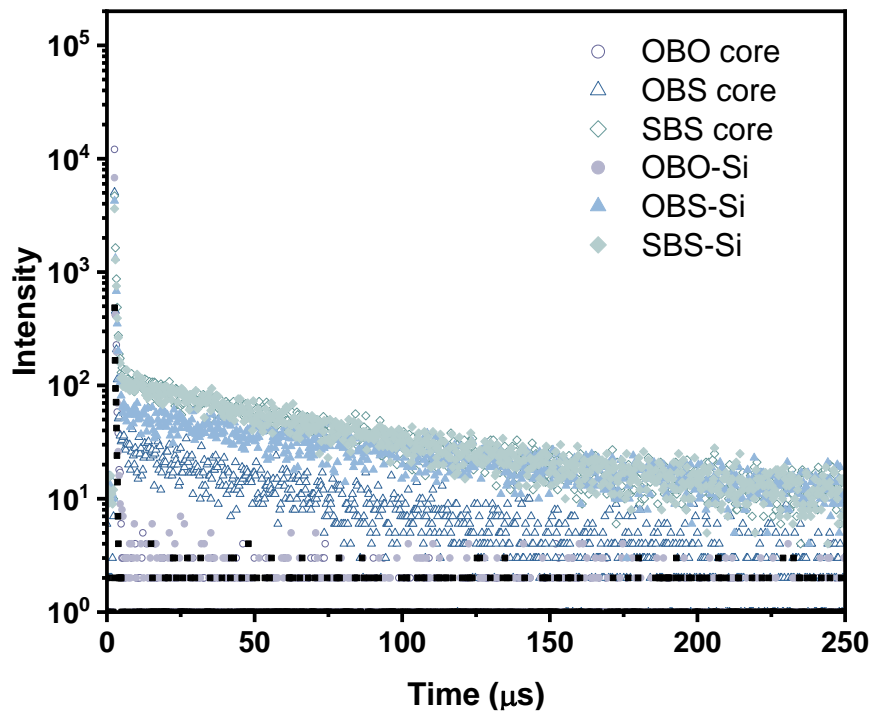


**Figure 4-6.** Time-resolved radiative decay profile of target materials doped in DPEPO film.

## 4.4. Conclusions

In summary, series of multiresonant TADF materials with two chalcogen atom of oxygen and sulfur and tetraphenylsilyl group were developed to evaluate rISC characteristics and its enhancement by spin-orbit coupling. Different from conventional D-A type TADF emitters described in previous chapters, MR type TADF materials showed narrow emission spectra which is advantageous to emitters to qualify pure color emitter. Moreover, from two molecular design strategies suggested, enhanced rISC characteristics were verified in direct and indirect way from photophysical measurements. Among the target materials, SBS-Si performed as pure blue TADF emitter with 468 nm of emission maximum wavelength, 35 nm of FWHM, fast and intensified delayed fluorescence.

## 4.5. References

1. Hatakeyama, T.; Shiren, K.; Nakajima, K.; Nomura, S.; Nakatsuka, S.; Kinoshita, K.; Ni, J.; Ono, Y.; Ikuta, T. Ultrapure Blue Thermally Activated Delayed Fluorescence Molecules: Efficient HOMO–LUMO Separation by the Multiple Resonance Effect. *Advanced Materials* **2016**, *28* (14), 2777-2781.
2. Ikeda, N.; Oda, S.; Matsumoto, R.; Yoshioka, M.; Fukushima, D.; Yoshiura, K.; Yasuda, N.; Hatakeyama, T. Solution-Processable Pure Green Thermally Activated Delayed Fluorescence Emitter Based on the Multiple Resonance Effect. *Advanced Materials* **2020**, *32* (40), 2004072.
3. Tanaka, H.; Oda, S.; Ricci, G.; Gotoh, H.; Tabata, K.; Kawasumi, R.; Beljonne, D.; Olivier, Y.; Hatakeyama, T. Hypsochromic Shift of Multiple-Resonance-Induced Thermally Activated Delayed Fluorescence by Oxygen Atom Incorporation. *Angewandte Chemie International Edition* **2021**, *60* (33), 17910-17914.
4. Kondo, Y.; Yoshiura, K.; Kitera, S.; Nishi, H.; Oda, S.; Gotoh, H.; Sasada, Y.; Yanai, M.; Hatakeyama, T. Narrowband deep-blue organic light-emitting diode featuring an organoboron-based emitter. *Nature Photonics* **2019**, *13* (10), 678-682.
5. Zou, Y.; Hu, J.; Yu, M.; Miao, J.; Xie, Z.; Qiu, Y.; Cao, X.; Yang, C. High-Performance Narrowband Pure-Red OLEDs with External Quantum Efficiencies up to 36.1% and Ultralow Efficiency Roll-Off. *Advanced Materials* **2022**, *34* (29), 2201442.
6. Nagata, M.; Min, H.; Watanabe, E.; Fukumoto, H.; Mizuhata, Y.; Tokitoh, N.; Agou, T.; Yasuda, T. Fused-Nonacyclic Multi-Resonance Delayed Fluorescence Emitter Based on Ladder-Thiaborin Exhibiting Narrowband Sky-Blue Emission with Accelerated Reverse Intersystem Crossing. *Angewandte Chemie International Edition* **2021**, *60* (37), 20280-20285.
7. Gao, H.; Shen, S.; Qin, Y.; Liu, G.; Gao, T.; Dong, X.; Pang, Z.; Xie, X.; Wang, P.; Wang, Y. Ultrapure Blue Thermally Activated Delayed Fluorescence (TADF) Emitters Based on

- Rigid Sulfur/Oxygen-Bridged Triarylboron Acceptor: MR TADF and D–A TADF. *The Journal of Physical Chemistry Letters* **2022**, *13* (32), 7561-7567.
8. Hu, Y. X.; Miao, J.; Hua, T.; Huang, Z.; Qi, Y.; Zou, Y.; Qiu, Y.; Xia, H.; Liu, H.; Cao, X.; et al. Efficient selenium-integrated TADF OLEDs with reduced roll-off. *Nature Photonics* **2022**, *16* (11), 803-810.
  9. Li, Q.; Wu, Y.; Yang, Q.; Wang, S.; Shao, S.; Wang, L. Selenium-Doped Polycyclic Aromatic Hydrocarbon Multiresonance Emitters with Fast Reverse Intersystem Crossing for Narrowband Blue Emission. *ACS Appl. Mater. Interfaces* **2022**, *14* (44), 49995-50003.
  10. Park, I. S.; Min, H.; Yasuda, T. Ultrafast Triplet–Singlet Exciton Interconversion in Narrowband Blue Organoboron Emitters Doped with Heavy Chalcogens. *Angewandte Chemie International Edition* **2022**, *61* (31), e202205684.
  11. Park, I. S.; Yang, M.; Shibata, H.; Amanokura, N.; Yasuda, T. Achieving Ultimate Narrowband and Ultrapure Blue Organic Light-Emitting Diodes Based on Polycyclo-Heteraborin Multi-Resonance Delayed-Fluorescence Emitters. *Advanced Materials* **2022**, *34* (9), 2107951.
  12. Wang, Y.; Zhang, K.; Chen, F.; Wang, X.; Yang, Q.; Wang, S.; Shao, S.; Wang, L. Boron-, Sulfur- and Nitrogen-Doped Tridecacyclic Aromatic Emitters with Multiple Resonance Effect for Narrowband Red Emission. *Chinese Journal of Chemistry* **2022**, *40* (22), 2671-2677.

## 국문 초록 (Abstract in Korean)

발광체는 유기 발광 다이오드와 관련된 주제들 중 가장 활발하게 논의되고 있을 정도로 유기 발광 다이오드에서 가장 중요한 역할을 수행한다. 기존의 형광체와 인광체의 시대를 지나, 열활성지연형광의 특성을 보이는 발광체들은 서로 다른 다중도를 갖는 들뜬 상태에서부터 빛을 발생시켜야 하는 발광체의 한계점을 극복했다는 점에서 주목을 받고 있다. 열활성지연형광을 효율적으로 활용하기 위해서는, 발광체 물질의 들뜬 삼중항 상태가 들뜬 단일항 상태와 작은 에너지 차이를 가지도록 세심하게 설계되어야 한다. 본 학위 논문에서는 들뜬 삼중항 상태가 광물리학적 관점에서 열활성지연형광에 중요하게 기여하는 바를 세 종류의 물질군을 통해 다루고자 한다.

제2장에서는 이미 우수한 열활성지연형광 발광체로 알려진 PXZ-OXD에 서로 다른 전자밀기 혹은 전자끌기 효과를 가지는 작용기를 도입하였다. 전반적인 연구를 통해 기존의 광물리학적 모델로는 충분히 설명되지 않는 분자내 전하 이동 및 국소적 들뜸에 기인한 서로 다른 들뜬 상태들 사이의 독특한 경향성을 관측하였다. 목표 물질이 분자내 전하 이동에 기인한 들뜬 단일항 상태와 들뜬 삼중항 상태 사이의 에너지 차이가 줄어듦에 따라 빠른 역계간교차를 일으키는 현상을 국소적 들뜸 상태의 도움을 필요로 하지 않는 2-레벨 모델을 통해 설명하였다. 이러한 결과를 바탕으로 청록색에서 녹색 영역의 발광을 가지는 유기 발광 다이오드를 제작할 수 있었다.

제3장에서는 적색 열활성지연형광 발광체의 전자받개로 나프탈이미드를 활용하였으며, 두 가지 분자 설계 전략을 통해 적색 열활성지연형광 발광체의 밝기와 색 특성을 향상시키고자 하였다. 전자주개-전자받개 형태의 열활성지연형광 발광체의 전자주개 부분을 변경시켰을 때에는 발광 스펙트럼의 측면에서는 확실한 장파장 영역으로의 이동을 보였으나, 장파장 영역의 발광체가 꺾게 되는 에너지 간격 법칙에 의해 발광성이 현저하게 줄어들었다. 그 대신에 전자끌기 효과를 가지는 작용기의 도입은 발광 영역에는 미미한 영향을 가져다 주었지만 역계간교차를 활성화시켜 유기 발광 다이오드 소자의 외부 양자 효율을 증가시키는 결과를 낳았다.

제4장에서는 기존의 전자주개-전자받개 형태의 열활성지연형광 발광체와 비교했을 때 세부적인 특징이 다른 광물리화학적 메커니즘을 갖는 다중공명 형태의 열활성지연형광 발광체가 제시되었다. 황과 규소에 기인한 무거운 원자 효과가 열활성지연형광 발광체에 있어 중요한 특징인 역계간교차를 향상시켰다.

**주요어:** 유기 발광 다이오드, 열활성지연형광, 들뜬 삼중항 상태, 고속 역계간교차, 옥사다이하졸, 나프탈이미드, 다중공명

**학번:** 2016-20824

## List of publications

1. Hyeong-Ju Kim<sup>†</sup>, In-Sun Jung<sup>†</sup>, **Seyoung Jung**<sup>†</sup>, Dongmin Kim, Daiki Minami, Sunjung Byun, Taejin Choi, Jisoo Shin, Sungyoung Yun, Chul-Joon Heo, Kyung-Bae Park, Soo Young Park, Seon-Jeong Lim\*, Hyo Sug Lee and Byoungki Choi, "Harnessing Intramolecular Chalcogen–Chalcogen Bonding in Merocyanines for Utilization in High-Efficiency Photon-to-Current Conversion Optoelectronics", ACS Appl. Mater. Interfaces, 14, 4360–4370, (2022)
2. Illia Serdiuk\*<sup>†</sup>, **Seyoung Jung**<sup>†</sup>, Michał Mońka, Chi Hyun Ryoo and Soo Young Park\*, "Contradictory Role of Locally-Excited Triplet States in Blue Thermally Activated Delayed Fluorescence of s-Triazine-Based Emitters", J. Phys. Chem. C, *accepted*
3. Jin Hong Kim<sup>†</sup>, Min-Woo Choi<sup>†</sup>, Su-Yeon Kim, **Seyoung Jung**, Yeong Suk Choi, and Soo Young Park\*, "Novel Organic Semiconductors Based on 1,5-Naphthyridine-2,6-dione Unit for Blue-selective Organic Phototransistor", Adv. Optical Mater., 8, 2000695, (2020)
4. Sangyoon Oh, Sang Kyu Park, Byung Hak Jhun, Juan Roldao, Jin Hong Kim, Min-Woo Choi, Chi Hyun Ryoo, **Seyoung Jung**, Nicola Demitri, Roland Fischer, Illia Serdiuk, Roland Resel\*, Johannes Gierschner\* and Soo Young Park\*, "Unraveling the Origin of High Efficiency Photoluminescence in Mixed-Stack Isostructural Crystals of Organic Charge-Transfer Complex: Fine-Tuning of Isometric Donor-Acceptor Pairs", J. Phys. Chem. C, 124, 20377–20387, (2020)

5. Chi Hyun Ryoo, Jongseok Han, Jung-hoon Yang, Kwangmo Yang, Ilhun Cho, **Seyoung Jung**, Sehun Kim, Hyein Jeong, Changhee Lee, Ji Eon Kwon, Illia E. Serdiuk\* and Soo Young Park\*, "Systematic Substituent Control in Blue Thermally Activated Delayed Fluorescence (TADF) Emitters: Unraveling the Role of Direct Intersystem Crossing between the Same Charge-Transfer States", Adv. Optical Mater., 2201622 (2022)

(† mark for equal contribution as the first author)

## **List of Presentations**

1. **Seyoung Jung**, Somasundaram Sivaraman, Chi Hyun Ryoo, Ji Eon Kwon, Sanghyuk Park and Soo Yung Park\*, "Fine Tuning of Photophysical Properties of Oxadiazole-based Thermally Activated Delayed Fluorescence (TADF) Materials", PSK fall 2017, Jeju, Korea
2. **Seyoung Jung**, Chi Hyun Ryoo, Ji Eon Kwon and Soo Young Park\*, "Tuning of Thermally Activated Delayed Fluorescence (TADF) Emitter Based on Naphthalimide toward Efficient and Deep Red Organic Light-emitting Diode (OLED)", MRS fall 2019, Boston, USA

## List of Patents

1. 김세훈, 박수영, 유치현, 조일훈, 양정훈, 정세영, 정혜인, “다환 화합물 및 이를 포함한 유기 발광 소자”, 대한민국제20180097807호.
2. 최용석, 박수영, 윤성영, 김형주, 정세영, 민동주, 권지언, “n-형 반도체 및 이를 포함하는 유기 광전 소자, 이미지 센서 및 전자 장치”, 대한민국제20210055399호.
3. 최용석, 박수영, 윤성영, 김형주, 최민우, 김수연, 김진홍, 정세영, “청색 흡수용 필름, 광전 소자 및 이를 포함하는 이미지 센서와 전자 장치”, 대한민국제20220096214호.